
Application of the chiral SMS potential to selected electromagnetic processes in two- and three-nucleon systems

Vitalii Urbanevych

Ph.D. thesis written under the supervision of dr. hab Roman Skibiński
at the Jagiellonian University, Faculty of Physics, Astronomy
and Applied Computer Science, Kraków,
Monday 19th February, 2024



CONTENTS

1	Introduction	1
2	Formalism and numerical methods	9
2.1	2N bound state	9
2.2	2N scattering state	13
2.3	3N bound state	15
2.4	3N scattering state	16
2.5	Nd scattering state	17
2.6	Nuclear electromagnetic current	18
2.7	Pion absorption	20
2.8	Theoretical uncertainties	23
3	Results	27
3.1	Deuteron photodisintegration	27
3.1.1	Cross section	27
3.1.2	Polarization observables	34
3.2	Helium-3 photodisintegration	55
3.2.1	Three-body breakup	55
3.2.2	Two-body breakup	63
3.3	Triton 3N photodisintegration	64
3.4	Pion absorption from the lowest atomic orbital	69
3.4.1	Pion absorption in ^2H	69
3.4.2	Pion absorption in ^3He	69
3.4.3	Pion absorption in ^3H	82
4	Summary	88
	Bibliography	91

Abstract

This Ph.D. thesis presents a comprehensive investigation into the application of the chiral potential to understand two types of processes with two- and three-nucleons. The primary focus is on the application of the state-of-the-art semilocal momentum-space regularized potential (SMS) potential to photodisintegration processes of ${}^2\text{H}$, ${}^3\text{H}$, and ${}^3\text{He}$, as well as to pion absorption by the same nuclei. The SMS potential is taken up to the fifth order of chiral expansion, $\text{N}^4\text{LO}+$, and augmented by the consistently regularized three-nucleon force at N^2LO .

The study employs the momentum space formalism, solving the standard Lippmann-Schwinger equation to obtain the t -operator and the corresponding two-nucleon scattering state. For three-nucleon processes, the Faddeev equations are utilized to include both initial and final state interactions, allowing a thorough examination of observables such as total cross sections, capture rates, differential cross sections, and polarization observables.

The main goal is to assess the quality and convergence of predictions based on the chiral SMS potential, particularly in comparison to the semi-phenomenological AV18 potential. The research explores the convergence of predictions with respect to the chiral order, revealing that predictions based on the SMS interaction are generally well-converged, indicating satisfactory model performance. Additionally, in this work I study the dependence of predictions on the intrinsic cut-off parameter Λ , providing valuable insights into the sensitivity of results to this parameter.

Furthermore, the study investigates the role of various dynamical components, including final state interactions and two-nucleon current contributions. The analysis highlights the significance of these components in influencing predicted values, emphasizing the importance of a fully consistent model incorporating 2N forces, 3N forces, and one-, two-, and three-body currents.

In conclusion, this work contributes to our understanding of electromagnetic and strong processes in nuclear physics, demonstrating the high quality and convergence of the chiral SMS potential. For all studied processes I point out especially interesting observables and kinematical configurations, in which the role of individual components of the Hamiltonian is highlighted.

This work is organized as follows. Chapter 1 provides an introduction to the theoretical framework and the motivation for the study. Chapter 2 presents the formalism and methodology used in the study. Chapter 3 presents the results of numerical calculations for corresponding processes, and Chapter 4 provides a summary and conclusions.

CHAPTER 1

INTRODUCTION

Why we study few nucleon systems

The study of light nuclei and their reactions has been serving as an easy way to investigate particles in nuclei and the forces between them for decades. A convenient way to proceed may be to study the interaction of a nucleus with other nuclei, particles, or electroweak probes such as electrons, photons, muons, pions, neutrinos, and hyperons. In most cases, the study of elastic or inelastic scattering is possible. This can be done either theoretically or by performing relevant experiments to test if the theory works. It should be taken into account that nuclear interactions may be caused by different fundamental forces, including strong, weak, or electromagnetic interactions. This depends on the type of particle being scattered and the target of the reaction and requires different theoretical approaches. Of course gravitational force is also in the game but due to its weakness it is usually omitted in the nuclear physics.

In the past many experimental efforts have been undertaken and experimentalists have been interested in electromagnetic reactions involving light nuclei for decades. There are experimental data from the second half of 20th century (e.g. [2–5]) which are still useful for comparing theoretical predictions with experimental measurements. There are several facilities providing sources of gamma rays (both low- and high-energy) and other particles that have been operating for decades and still enable experiments to be conducted. Let us mention here such facilities as TUNL with HI γ S [6, 7] or MAMI [8].

To accurately describe nuclear reactions, two important components of the Hamiltonian must be considered. They are nuclear interactions and nuclear currents. First of all, various nuclear forces may act on the particles.

The strong nuclear force acts inside the nuclei and, among others, binds neutrons and protons together. The description of strong interactions is extremely difficult as it deals not only with the nucleons themselves but also with their constituents: quarks and gluons. Quantum chromodynamics (QCD) is a modern theory describing strong interactions, but, at the moment, it is not applicable at low energies (e.a. at $Q^2 \lesssim 1\text{GeV}^2$). In such a situation, various approaches are emerging. The most advanced is the chiral effective theory and lattice calculation [9–11]. In this work we will use the results of the first approach and the corresponding model is described in Sec. 2.

A study of three- (and more) nucleon systems showed that the strong two-nucleon (2N) force is not efficient in describing $N > 2$ systems, thus a three-nucleon (3N) force

(3NF) was introduced. The first applications of such a force showed that it brings a sizable contribution to observables and cannot be ignored [12]. The contribution of the 3NF can be examined e.g. by comparing binding energies of light nuclei calculated with and without this part of the Hamiltonian concerning experimental values.

For example, the binding energy¹ for ${}^3\text{H}$ calculated with the Argonne V18 (AV18) 2N potential without 3NF amounts to $E_b({}^3\text{H}) = -7.628 \text{ MeV}$ [13]. There are different models that might add a 3NF contribution to AV18 (or other potentials). Using the Tucson-Melbourne (TM) model [14] results in $E_b({}^3\text{H}) = -8.478 \text{ MeV}$, and the Urbana IX [15] 3NF provides us with $E_b({}^3\text{H}) = -8.484 \text{ MeV}$. Looking at the experimental value $E_b({}^3\text{H}) = -8.482 \text{ MeV}$, it is clear that the 3NF contribution makes the prediction much closer to the measurement. Nevertheless, the parameters of the UrbanaIX 3NF were fitted to the experimental value for ${}^3\text{H}$, so there is no surprise in good agreement.

However one can also check the binding energy for other nuclei, which were not used for the fitting. The 2N force (2NF) binding energy for ${}^3\text{He}$ (calculated with AV18) is $E_b({}^3\text{He}) = -6.917 \text{ MeV}$. The TM contribution makes it $E_b({}^3\text{He}) = -7.706 \text{ MeV}$, the Urbana IX gives $E_b({}^3\text{He}) = -7.739 \text{ MeV}$, while the experimental value is $E_b({}^3\text{He}) = -7.718 \text{ MeV}$. One can see the importance of 3NF contribution also for the α -particle's (${}^4\text{He}$) binding energy: the AV18 alone gives $E_b({}^4\text{He}) = -24.25 \text{ MeV}$, while the AV18 + TM leads to -28.84 MeV , the AV18 + Urbana IX delivers $E_b({}^4\text{He}) = -28.50 \text{ MeV}$, and the experimental value is -28.30 MeV [13].

Whereas the first applications included only early simplified "realistic" 3N potential, the latter investigations, based on more advanced models, fully confirmed this statement [16,17]. Within new models, the four-nucleon (4N) interaction was constructed to improve the description of ${}^4\text{He}$ [18]. A broader discussion of nuclear forces used in this thesis is given below.

The electromagnetic force appears between charged particles like protons, electrons, or pions. That force acts also between charged particles and photons, so in photon- and electron- scatterings on the nuclei it is a necessary component of a description. However, electromagnetic interaction between nuclei manifests only at very low energies or for specific kinematic configurations with two protons having approximately equal momenta. Thus it rather is skipped in the lowest-order analysis.

The main contribution of electromagnetic interaction to disintegration processes in hand is due to the current operator describing photon-nucleon vertex and second-order processes. The structure of the electromagnetic current has been investigated in many works by numerous groups [19] but it was H. Arenhövel who performed a study of nuclear electromagnetic current in the few-nucleon sector. His long-term research, reviewed in [20] demonstrated various theoretical models applied to the deuteron photodisintegration. He analyzed among others a nonrelativistic potential model, a relativistic impulse approximation, and a relativistic meson-exchange model. These models were used to calculate the differential cross section and various polarization observables, which describe the probability of the process occurring at different scattering angles, photon energies, spin directions, etc.

The calculated cross sections were then compared to experimental data, and it was found that the relativistic meson-exchange model provided the best agreement with the data at photon's energies up to $E_\gamma \approx 100 \text{ MeV}$. At higher energies agreement is observed but is getting worse. This model includes the exchange of virtual mesons between the interacting particles, which accounts for the strong and electromagnetic forces between

¹More precisely it is a ground state energy, but I follow commonly used mental shortcut.

them.

Overall, Arenhövel demonstrated the importance of including both strong interaction and electromagnetic current operator in a description of the deuteron photodisintegration process, and highlighted the need for accurate theoretical models to interpret experimental data.

The weak force is of great importance in the study of nuclear processes. One of the main roles of the weak force is to mediate negative beta decay, which is a process in which a neutron in a nucleus is converted into a proton, emitting an electron and an antineutrino. This process plays a crucial role in the formation of elements in the universe, as it allows for the conversion of neutron-rich isotopes into more stable, proton-rich isotopes. Additionally, the weak force plays a role in neutrino interactions with matter, which are of great interest in both astrophysics and particle physics. In nuclear physics, weak interactions can also play a role in the decay of unstable nuclei, the production of neutrinos in nuclear reactions, and the scattering of neutrinos off nuclei. The study of weak interactions is therefore an essential component of the overall understanding of nuclear physics and the behavior of matter on the subatomic scale. However, in the thesis, I stick with electromagnetic processes.

Models of strong interaction used in the thesis

In order to model the nuclear potential, physicists often use phenomenological or semi-phenomenological approaches. It allows them to combine theoretical knowledge about the studied processes and experimental findings.

Among many of such models, the AV18 [17] force is one of the most advanced and therefore is used in the current thesis. To construct the nucleon-nucleon (NN) force, authors combine long-range one-pion-exchange part with short-range phenomenological one and supplement them with electromagnetic corrections. Free parameters were fitted to the Nijmegen partial-wave analysis of pp and np data [21]. Authors showed, that the AV18 potential delivers good description of nucleon-nucleon scattering data ($\chi^2/data = 1.08$ for around 4000 pp and np scattering data points) as well as deuteron properties (estimated binding energy is 2.2247(35) MeV vs experimental 2.224 575(9) MeV [22]).

Weinberg's idea of using chiral symmetry to describe nuclear interactions at low energies was first introduced in his papers published in 1990 and 1991 [23,24]. In these papers, Weinberg argued that the low-energy dynamics of nucleons could be described using a chiral Lagrangian, which is the most general Lagrangian consistent with chiral symmetry and its spontaneous breaking. This Lagrangian is expressed in terms of nucleon and pion fields, which are the degrees of freedom that become relevant at low energies.

The chiral Lagrangian is the starting point for the development of the Chiral Effective Field Theory (χ EFT), which has become one of the most advanced approaches to low-energy nuclear physics [25]. The use of the χ EFT allows (at least in theory) for the calculation of nuclear properties and reactions in a model-independent way. It is also possible to quantify the uncertainties associated with the calculation. One of the key features of the χ EFT is that it allows for the construction of a nuclear potential, which can then be used in relevant formalisms, e.g. to solve the Schrödinger equation and to obtain bound and scattering state properties. The accuracy of the potential can be systematically improved by including higher-order terms in the chiral expansion, which leads to a better description of experimental data.

In the χ EFT there are two natural scales: so-called soft scale $Q \sim M_\pi$ - the mass of

pion and the hard scale - $\Lambda_\chi \sim 0.7 \text{ GeV}$ - the chiral symmetry breaking scale. The ratio between these two scales Q/Λ_χ is being used as an expansion parameter in χEFT with power ν : $(Q/\Lambda_\chi)^\nu$.²

The possibility of deriving nuclear potential is an important feature of χEFT . The potential, as occurs in Lagrangian, is a perturbation expression of the same parameter Q/Λ_χ . Considering so-called irreducible diagrams (which cannot be split by cutting nucleon lines), Weinberg [23, 24] came to the expression for the powers ν_W of such diagrams

$$\nu_W = 4 - A - 2C + 2L + \sum_i \Delta_i, \quad (1.1)$$

where i specifies a vertex number and

$$\Delta_i \equiv d_i + \frac{n_i}{2} - 2. \quad (1.2)$$

In Eq. (1.1) C is a number of pieces which are connected, L - the number of loops in the graph and A is the amount of nucleons in the diagram. In Eq. (1.2) n_i is a number of nucleon field operators and d_i - the number of insertions (or derivatives) of M_π .

Further analysis of Eq. (1.1) revealed some problems which occur for particular values of parameters in the equation, namely negative values of ν_W are possible while the order has to take integer values from 0 to infinity. To deal with that, Eq. (1.1) was slightly modified by adding $3A - 6$ to it [11, 27]:

$$\nu = \nu_W + 3A - 6 = -2 + 2A - 2C + 2L + \sum_i \Delta_i. \quad (1.3)$$

That convention above is widely used and we will also stick to it as well.

In χEFT the first order, "leading order" ($\nu = 0$) is followed by the next-to-leading order ($\nu = 2$)³, the next-to-next-to-leading order ($\nu = 3$) and so on. At each chiral order, new interaction diagrams complete the potential. There are only two diagrams at leading order (LO): one is a contact term and the other one is a one-pion exchange, see Fig. 1.1. Both diagrams reflect only 2NF. The same is for diagrams at next-to-leading order (NLO), where more contact terms occur together with two-pion exchange topologies. Each subsequent order includes more and more sophisticated diagrams describing nucleon interaction via multiple pion exchanges and various contact vertexes. 3NF appears for the first time at next-to-next-to-leading order (N^2LO) while 4NF contributions start from next-to-next-to-next-to-leading order (N^3LO). This scheme establishes for the first time a systematic way to include all the contributions to a strong nuclear force starting from the simplest diagrams at LO and gradually adding more and more terms. It is also beneficial in the way that one can obtain results using chiral potential at different orders and track which one gives a large or small contribution to the final prediction. At the moment, next-to-next-to-next-to-next-to-leading order (N^4LO) is the highest order at which 2N interaction has been completely derived. Nevertheless leading F-wave contact interactions from N^5LO have been combined with N^4LO force leading to the N^4LO^+ potential, which is currently regarded as the best available potential on the market. The progression of the chiral orders is reflected in a χ^2/data . Leading order results in $\chi^2/\text{data} = 73$ (with

²Note that exact values of some parameters are still under discussion [26]. We follow here approach proposed by E. Epelbaum and collaborators, see e.g. [1]

³The contributions to the potential at order $\nu = 1$ completely vanish due to parity and time-reversal invariance, so the next-to-leading order stands for the second order ($\nu = 2$) of expansion.

neutron-proton data with $E_{lab} = 0 - 100\text{MeV}$). Each subsequent order has better and better results: NLO gives $\chi^2/data = 2.2$, $N^2\text{LO}$ - $\chi^2/data = 1.2$ and the highest, $N^4\text{LO}^+$, leads to $\chi^2/data = 1.08$ [1]. Similar progress is observed for a wider energy range, e.g for $E_{lab} = 0 - 300\text{MeV}$ $\chi^2/data$ is 75, 14, 4.1, 2.01, 1.16 and 1.06 at LO, NLO, $N^2\text{LO}$, $N^3\text{LO}$, $N^4\text{LO}$ and $N^4\text{LO}^+$, respectively. The proton-proton data description has a similar trend, so $\chi^2/data$ is 1380, 91, 41, 3.43, 1.67, 1.00 for the same energy bin and chiral orders. At $N^4\text{LO}^+$ $\chi^2/data$ for proton-proton data stands a similar value (close to 1) as for neutron-proton. However for the proton-proton force, the convergence comes a bit later, and the leading order has a way worse description than for the neutron-proton potential. In my work, I will use chiral potentials from LO up to $N^4\text{LO}^+$.

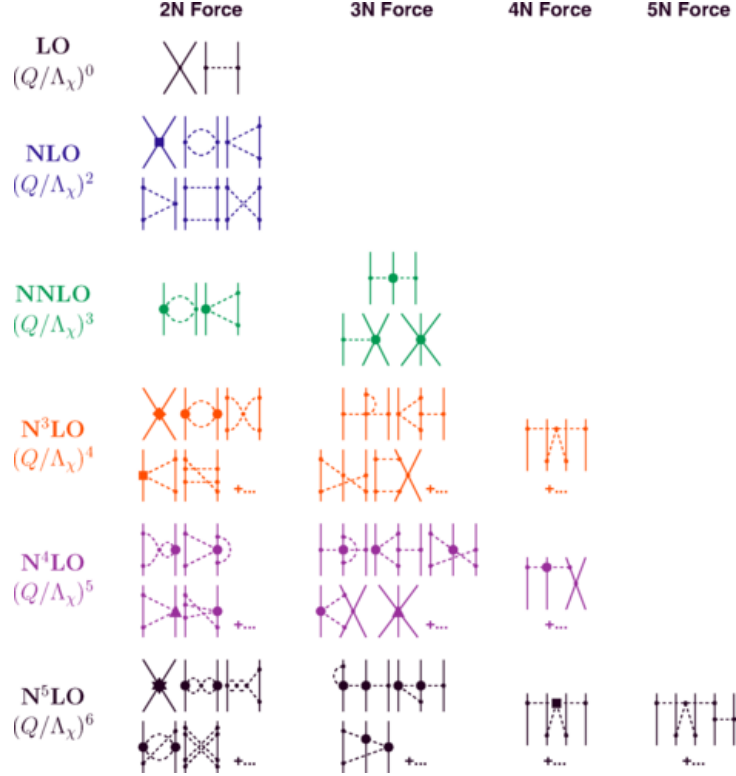


Figure 1.1: *Make own diagrams, e.g. with JaxoDraw or PyFeyn [28]*

The Argonne V18 potential [17], mentioned earlier, has 40 adjustable parameters, while χEFT NN potential at $N^4\text{LO}$ [11] has only 27 low-energy constants (LECs) fitted to 2N data. The reduction of the number of free parameters of the χEFT -based potentials has not only a theoretical but also a practical advantage in the studies of nuclear systems.

The general scheme outlined above was developed mainly by the Bochum-Bonn and Moscow-Idaho groups. Both groups have similar approaches and were independently and almost simultaneously developing their models. In 1998 Epelbaum and collaborators from the Bochum-Bonn group presented a first version of their NN chiral potential [29,30]. Developing more and more sophisticated versions with higher chiral orders, authors presented in 2001 [31] $N^2\text{LO}$ model which included 3NF contributions and in 2005 [32] $N^3\text{LO}$ NN potential. They were further developing their chiral model, taking into account more Feynmann diagrams coming to a higher chiral orders. At some moment Bochum-Bonn group faced a problem of potential regularisation [33,34]. Solving it was a necessary step but authors were struggling with finding an appropriate regularization method to handle

the divergences that arise in the χ EFT calculations. Different techniques were applied such as the cutoff regularization and the regulator function methods. An important step was done when authors started using a semi-local regularisation in the coordinate space. The corresponding potential is called the SCS potential (semi-local regularisation in the coordinate space) [35]. Later similar regularisation, but done in momentum space was introduced, resulting in the most advanced chiral potential [1]: the SMS. It is developed up to $N^4\text{LO}^+$ at the moment.

On the other side of the planet, in Idaho, R. Machleidt and his group from Moscow(Idaho) were also developing a chiral interaction. Their results from 2003 [36], following with later investigations [37, 38] and recently in [28] introduced very similar model to the one from the Bochum-Bonn group with minor technical differences.

There are a number of other attempts to construct the nuclear potential from the χ EFT. M.Piarulli et al [39, 40] contributed to quite a similar approach, based on the same chiral potentials but including explicitly Δ -isobar intermediate states up to the third chiral order and taking into account sophisticated electromagnetic corrections.

Other groups try to improve already derived forces. Let us mention here works by A. Ekström and collaborators [41, 42] who, by using advanced fitting methods combined with statistical analysis proposed so-called optimised interaction V_{opt} which was proved to provide a good description of nuclei properties and nuclear matter without using 3NF.

Another approach is the pionless effective field theory, which integrates pions out and focuses on the various types of contact interactions between nucleons [43]. Obtained potential has a very simple form, but cannot be applied to higher energies since pions start playing an important role there.

Yet another promising approach is the Lattice Effective Field Theory (LEFT), which is based on the Lattice QCD simulations of the strong interaction. U.-G. Meißner and collaborators have developed a chiral effective theory for nuclear forces based on the methods of lattice QCD calculations [44]. This approach has the advantage of being able to predict the nuclear force directly from the first principles, without the need for phenomenological input. However, currently, it is limited to small systems and low energies due to the computational resources required for calculations. Up to now, the relatively simple two-nucleon scattering problem and few-nucleon bound state have been solved within the LEFT and more complex systems are still under attack. For more details please refer to [44].

Technically, the chiral potential may be derived both in coordinate and momentum spaces. Nevertheless, in both cases, it requires regularisation which improves potential behavior at small distances or at high momenta, which allows to avoid infinities. The SMS potential is being regularized semilocally. It means that local or nonlocal regularisations are being applied for different parts of the potential. In [32, 36] the non-local regulation scheme was applied to both short- and long-range parts of the potential while in the next model [28, 35] it affected only a short-range part. This regularisation is applied directly to the potential matrix elements in the coordinate space:

$$V_{\pi}(\vec{r}) \rightarrow V_{\pi,R}(\vec{r}) = V_{\pi}(\vec{r}) \left(1 - \exp(-r^2/R^2)\right), \quad (1.4)$$

or in the momentum space

$$V_{\pi}(\vec{p}', \vec{p}) \rightarrow V_{\Lambda}(\vec{p}', \vec{p}) = V_{\pi}(\vec{p}', \vec{p}) \exp \left[-(p'/\Lambda)^{2n} - (p/\Lambda)^{2n} \right], \quad (1.5)$$

where the cutoff R was chosen in the range of $R = 0.8, \dots, 1.2$ fm, $\Lambda = \frac{2}{R}$ and n being

adjusted with respect to the considered chiral order. For specific case of the SMS force $\Lambda = 400 - 550 \text{ MeV}$ and $n = 3$.

The other way of regularisation, the local one, is applied to the propagator operator, already during the derivation of potential. Namely, the Gaussian form factor $F(\vec{l}^2)$ is being used to reduce pions with higher momenta:

$$\int_{-\infty}^{\infty} \frac{\rho(\mu^2)}{\vec{l}^2 + \mu^2} d\mu^2 \rightarrow \frac{F(\vec{l}^2)}{\vec{l}^2 + \mu^2} \quad (1.6)$$

with

$$F(\vec{l}^2) = e^{-\frac{\vec{l}^2 + M_\pi^2}{\Lambda^2}}, \quad (1.7)$$

M_π is an effective pion mass, Λ - a cutoff parameter and l is a four-momentum of the exchanged pion. The form factor (1.7), being used together with Feynman propagator, ensures that the long-range part of the forces has no singularities.

The cut-off parameter Λ is not fixed and usually calculations are being performed for its different values. The comparison of such results may reveal stronger or weaker dependence on Λ and in a perfect case, which is expected at $\nu \gg 1$, one will come up with such a potential, where the cut will not affect results at all. One of the aims of my thesis is to test how a big cut-off dependency of predictions is observed for the best currently available forces (SCS and SMS). To illustrate a cutoff dependency of the potential, in Fig. 1.2 I show values of the matrix elements for $2N \langle p|V|p' \rangle$ potential ${}^3S_1 - {}^3D_1$ as a function of the momentum $|\vec{p}|$ with fixed value $|\vec{p}'| = 1.798 \text{ fm}^{-1}$. Please note, that the relatively strong dependency of specific matrix elements on the potential is not always leading to a strong dependency of observables, as observables comprise contributions from many matrix elements.

Let me add, that another regularisation function used by R. Machleidt and collaborators with non-local regulator only [28, 36]. That is the main reason for the observed differences between predictions based on Epelbaum's and Machleidt's models.

Currents

The electromagnetic current operator for a few-nucleon system has both one- and many-body contributions, which can be denoted as $j_\mu^1, j_\mu^2, j_\mu^3$, etc, respectively (where $\mu = 0..3$ denotes a four-vector components). The leading one-body contribution, j_μ^1 , represents the photon's interaction with a single nucleon. The many-body contributions are known as meson exchange currents (MEC) and arise from the meson-exchange picture of the nucleon-nucleon (NN) interaction. In that picture, the photon can couple also to mesons exchanged between two nucleons, leading to two-body contributions to the nuclear current. The necessity of introducing the MEC arises from the continuity equation. The momentum and isospin-dependent terms in the potential require the introduction of two-body MEC. Similarly, the inclusion of the three-body force into the Hamiltonian requires the existence of three-body contributions to the nuclear current. However, the effects of the three-body MEC are likely negligible in the low-energy region. Therefore, in the thesis, I will consider one- and two-body currents, only. The continuity equation, connecting the interaction and the current clearly shows that those two quantities should be derived consistently from the same underlying theory of nuclear phenomena. I work with the SMS chiral interaction and for that force the complete consistent MEC has not



Figure 1.2: Matrix elements $\langle p|V|p' \rangle$ of the SMS potential in coupled partial waves ${}^3S_1 - {}^3D_1$ as a function on the momentum p with fixed value of the momentum $p' = 1.798 \text{ fm}^{-1}$. Potential element $V_{ll'}$ is taken between two states with angular momenta l and l' where $l = 0$ stands for 3S_1 state and $l = 2$ for 3D_1 .

been derived yet. Consistency includes here also the same regularization as used for the interaction. While the derivation of such currents is ongoing [?], at the moment only SNC is well established. Thus to mimic the effects of the MEC, I apply the Siegert theorem [45, 46]. In general, this theorem allows the substitution of explicit MEC terms by the time component of the nuclear current (the charge density). It is less sensitive to MEC contributions (compared to spatial components of j_μ) and thus in its case, the SNC approximation is sufficient. I use here the formulation of the Siegert theorem given in [46].

A more detailed discussion of electromagnetic currents used here is given in the Section 2.6.

CHAPTER 2

FORMALISM AND NUMERICAL METHODS

Even though the deuteron problem was solved a long time ago, I will describe it briefly to introduce the notation and formalism. With that, for more complex 3N cases only a slight extension will be needed.

To calculate any observable for the deuteron photodisintegration, one has to find a nuclear matrix elements:

$$N^\mu = \langle \Psi_{final} | J^\mu | \Psi_{initial} \rangle, \quad (2.1)$$

with the two-nucleon wave function of the initial state $\Psi_{initial} = \Psi_{deuteron}$; the two-nucleon wave function of the final scattering state Ψ_{final} and a four-vector current operator J^μ which acts between initial and final two-nucleon states. In case of ${}^3\text{He}$ or ${}^3\text{H}$ photodisintegration analogous nuclear matrix element $\langle \Psi_{final} | J^\mu | \Psi_{initial} \rangle$ has to be found, but now $|\Psi_{initial}\rangle$ is either ${}^3\text{He}$ or ${}^3\text{H}$ bound state and $\langle \Psi_{final}|$ describes a 3N scattering state with all three nucleons unbound after reaction or Nd scattering state with the pair nucleon-deuteron in the final state. In the following, I describe how to get these quantities.

2.1 2N bound state

Let's find a deuteron bound state wave function $|\phi_d\rangle$. The time-independent Schrödinger equation for two particles is expressed as:

$$(H_0 + V) |\phi_d\rangle = E_d |\phi_d\rangle, \quad (2.2)$$

with a kinetic energy H_0 and potential V . The kinetic energy H_0 can be represented in terms of relative and total momenta of the particles:

$$H_0 = \frac{\vec{p}_1^2}{2m_1} + \frac{\vec{p}_2^2}{2m_2} = \frac{\vec{p}^2}{2\mu} + \frac{\vec{P}^2}{2M}, \quad (2.3)$$

where the relative and total momenta are defined as follows:

$$\vec{p} = \frac{(m_1 \vec{p}_1 - m_2 \vec{p}_2)}{m_1 + m_2}, \quad (2.4)$$

$$\vec{\mathcal{P}} = \vec{p}_1 + \vec{p}_2, \quad (2.5)$$

where $M = m_1 + m_2$ is a total mass, $\mu = \frac{m_1 m_2}{M}$ is a reduced mass of two nucleons and \vec{p}_i is the momentum of i-th particle.

Potential V is assumed to depend on the relative degrees of freedom only, so Eq. (2.2) may be decomposed into two separate equations:

$$\frac{\vec{p}^2}{2\mu} \langle \vec{p} | \Psi_{int} \rangle + \langle \vec{p} | V | \Psi_{int} \rangle = (E_d - E) \langle \vec{p} | \Psi_{int} \rangle \quad (2.6)$$

$$\frac{\vec{\mathcal{P}}^2}{2M} \langle \vec{\mathcal{P}} | \Psi \rangle = E \langle \vec{\mathcal{P}} | \Psi \rangle, \quad (2.7)$$

with $\langle \vec{p}, \vec{\mathcal{P}} | H_0 | \phi_d \rangle = \frac{\vec{p}^2}{2\mu} \langle \vec{p} | \Psi_{int} \rangle + \frac{\vec{\mathcal{P}}^2}{2M} \langle \vec{\mathcal{P}} | \Psi \rangle$. So Ψ is a component of the total wave function, which reflects a deuteron as a single object with momentum $\vec{\mathcal{P}}$ while Ψ_{int} is an internal wave function describing the interaction between nucleons. Basis state $|\vec{p}\rangle$ obeys a completeness equation:

$$\int d^3 \vec{p} |\vec{p}\rangle \langle \vec{p}| = 1. \quad (2.8)$$

Eq. (2.6) is basically the Schrödinger equation for a single particle with mass μ in potential V and Eq. (2.7) can be regarded as a Schrödinger equation for particle with mass M in a free motion. Assuming that deuteron is at rest ($E = 0$) we can stick to the Eq.(2.6) only. Using completeness relation (2.8) we get:

$$\frac{\vec{p}^2}{2\mu} \langle \vec{p} | \Psi_{int} \rangle + \int d\vec{p}' \langle \vec{p} | V | \vec{p}' \rangle \langle \vec{p}' | \Psi_{int} \rangle = E_d \langle \vec{p} | \Psi_{int} \rangle \quad (2.9)$$

Working in 3-dimensional space (i.e. directly with \vec{p} vectors) is difficult, especially numerically, so I follow a standard path and introduce the partial-wave decomposed representation (PWD) of the momentum state, adding spin and isospin degrees of freedom in the following form:

$$|p\alpha\rangle \equiv |p(ls)jm_j\rangle |tm_t\rangle, \quad (2.10)$$

where quantum numbers l, s, j, t are orbital angular momentum, total spin, total angular momentum and total isospin respectively. m_j and m_t are total angular momentum and isospin projections, respectively.

States $|p(ls)jm_j\rangle$ can be further decomposed to the more basic states than it is in (2.10), separating spin part as

$$|p(ls)jm_j\rangle = \sum_{m_l} c(ls j; m_l, m_j - m_l, m_j) |plm_l\rangle |s m_j - m_l\rangle. \quad (2.11)$$

Spin(isospin) states can be further represented via single-nucleon spin(isospin) states:

$$|sm_s\rangle = \sum_{m_1} c\left(\frac{1}{2}\frac{1}{2}s; m_1, m_s - m_1, m_s\right) \left|\frac{1}{2}m_1\right\rangle \left|\frac{1}{2}m_s - m_1\right\rangle, \quad (2.12)$$

$$|tm_t\rangle = \sum_{\nu_1} c\left(\frac{1}{2}\frac{1}{2}t; \nu_1, m_t - \nu_1, m_t\right) \left|\frac{1}{2}\nu_1\right\rangle \left|\frac{1}{2}m_t - \nu_1\right\rangle. \quad (2.13)$$

In Eqs.(2.11) -(2.13), $c(\dots)$ are Clebsh-Gordon coefficients. Nucleons are spin $\frac{1}{2}$ particles, and we also treat proton and neutron as the same particle in different isospin states, using convention in which isospin $\nu_1 = \frac{1}{2}$ stands for proton and $\nu_1 = -\frac{1}{2}$ is for neutron.

The states $|plm_l\rangle$ from Eq.(2.11) are orthogonal

$$\langle p'l'm'_l | plm_l\rangle = \frac{\delta(p-p')}{p^2} \delta_{ll'} \delta_{m_l m'_l} \quad (2.14)$$

and satisfy the completeness relation:

$$\sum_{l=0}^{\infty} \sum_{m_l=-l}^l \int dp p^2 |plm_l\rangle \langle plm_l| = \mathbb{1} \quad (2.15)$$

Projection of $\langle \vec{p}'|$ states to $|plm_l\rangle$ leads to

$$\langle \vec{p}' | plm_l\rangle = \frac{\delta(|\vec{p}'| - p)}{p^2} Y_{lm_l}(\hat{p}'), \quad (2.16)$$

where $Y_{lm_l}(\hat{p}')$ is a spherical harmonic and 'hat' denotes a unit vector \hat{X} in direction of \vec{X} . Thus for the momentum vector:

$$\vec{p} \equiv |\vec{p}|\hat{p} \equiv p\hat{p}. \quad (2.17)$$

Nucleons are fermions so exchanging them leads to antisymmetry of the wave function. In PWD it results in additional requirements on allowed quantum numbers which is:

$$(-1)^{l+s+t} = -1. \quad (2.18)$$

In general, nuclear NN force conserves spin, parity, and charge so

$$\langle p'\alpha' | V | p\alpha \rangle = \delta_{jj'} \delta_{mm'} \delta_{tt'} \delta_{m_t m'_t} \delta_{ss'} V_{ll'}^{sjtm_t}(p', p) \quad (2.19)$$

which introduces restrictions for particular sets of quantum numbers α and α' . Strong interaction allows for change of the orbital angular momenta $l = j \pm 1$, $l' = j' \pm 1$. The channels, in which $l \neq l'$ is allowed, are called coupled channels and for the deuteron bound state one can find only one such PWD state combination: two coupled channels which are commonly denoted as 3S_1 and 3D_1 (the naming stands for ${}^{2s+1}l_j$). They correspond to $l = 0$ and $l = 2$ respectively (with $s = j = 1$ and $t = m_t = 0$). I will denote wave functions for these channels as $\phi_l(p)$ with $l = 0, 2$, such that:

$$\phi_l(p) = \langle p(ls)jm_d | \langle tm_t | \Psi_{int} \rangle = \langle p(l1)1m_d | \langle 00 | \Psi_{int} \rangle; l = 0, 2. \quad (2.20)$$

In that new basis Eq.(2.9) takes a form of two coupled equations:

$$\frac{\vec{p}^2}{2\mu}\phi_l(p) + \sum_{l'=0,2} \int dp' p'^2 \langle p(l1)1m_d | \langle 00|V|00 \rangle | p'(l'1)1m_d \rangle \phi_{l'}(p') = E_d \phi_l(p), \quad (2.21)$$

for $l = 0, 2$. In case one does not have a matrix elements for the potential $\langle plm_l | V | p'l'm_l' \rangle$ in analytical form, but only numerical values for some grid of points are given, there is still one complication in the Eq.(2.21) - integration, which has to be discretized. In order to get rid of the integral I use a Gaussian quadrature method of numerical integration [47]. It allows me to replace an integral by the weighted sum: $\int_a^b f(x)dx = \sum_{i=1}^N \omega_i f(x_i)$. In current work I used $N = 72$ points in the interval from 0 to 50 fm^{-1} . Using this method, Eq.(2.21) becomes

$$\frac{p_i^2}{2\mu}\phi_l(p_i) + \sum_{l'=0,2} \sum_{j=0}^N \omega_j p_j^2 \langle p_i(l1)1m_d | \langle 00|V|00 \rangle | p_j(l'1)1m_d \rangle \phi_{l'}(p_j) = E_d \phi_l(p_i). \quad (2.22)$$

In practical computations, the same grid points p_i are used for p and p' in order to optimize computational time. I solve this equation as an eigenvalue problem $M\Psi = E_d\Psi$ and in that way find simultaneously wave function values in a grid of p points and the binding energy E_d . For example, the binding energy E_d calculated with the SMS potential at different chiral orders is presented in Fig. 2.1.

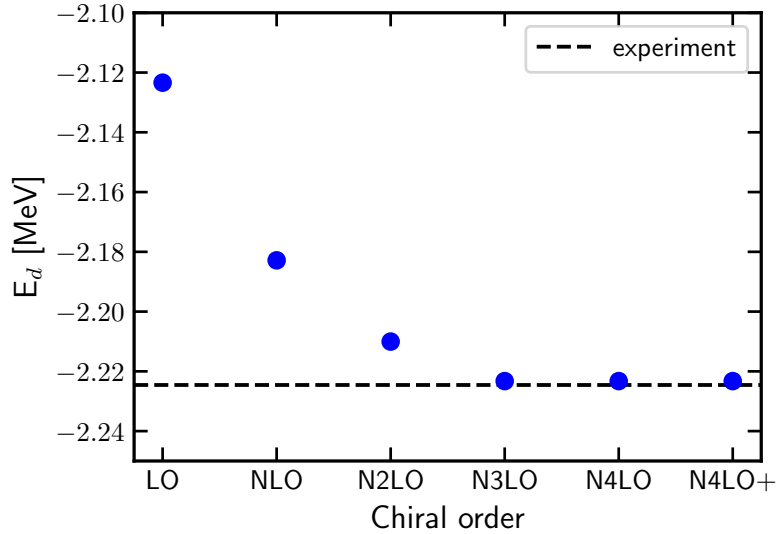


Figure 2.1: Deuteron binding energy calculated using the chiral SMS potential at different chiral orders as a mean value over all cutoffs. Experimental data is taken from [22].

An example of such wave functions is demonstrated in Fig. 2.2. The left panel demonstrates a wave function for $l = 0$ - 3S_1 while the right one - for $l = 2$ - 3D_1 . Both plots consist of the curves for different cutoff values and using the chiral SMS potential at $N^4\text{LO}^+$. The small deviation between lines shows that cutoff dependence is rather weak at this stage but further discrepancies connected to the value of Λ may appear in other components of nuclear matrix elements.

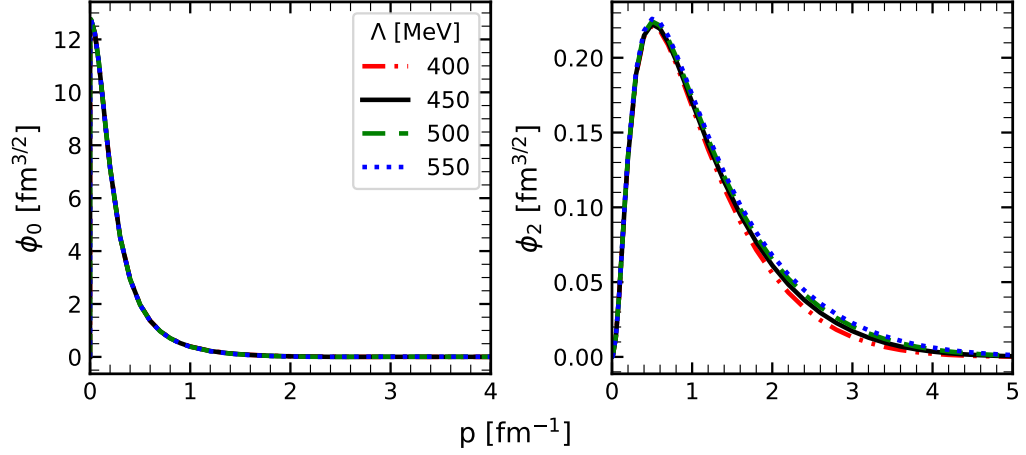


Figure 2.2: The deuteron wave function ϕ_l for $l=0$ (3S_1 partial wave)(left) and $l=2$ (3D_1) (right). Each curve shows results obtained with different values of the cutoff parameter Λ . The chiral SMS potential at $N^4\text{LO}^+$ was used.

2.2 2N scattering state

I work in the time-independent formulation of the scattering process. In such a case the Hamiltonian is:

$$H = H_0 + V, \quad (2.23)$$

where again H_0 is a kinetic energy operator, $H_0 = \frac{\vec{p}^2}{2m}$, and V is a nucleon-nucleon interaction. For a free particle motion, V will be absent and we will denote a corresponding energy eigenstate as a free particle state $|\vec{p}\rangle$. The scattering state $|\psi\rangle$ fulfills similar Schrödinger equation as $|\vec{p}\rangle$, with the same energy eigenvalue, but with the presence of the potential:

$$\begin{cases} H_0 |\vec{p}\rangle &= E |\vec{p}\rangle, \\ (H_0 + V) |\psi\rangle &= E |\psi\rangle. \end{cases} \quad (2.24)$$

We are interested in a solution for Eq. (2.24), so that $|\psi\rangle \rightarrow |\vec{p}\rangle$ as $V \rightarrow 0$ and both $|\psi\rangle$ and $|\vec{p}\rangle$ have the same energy eigenvalues E . As we have scattering process, the energy spectra for both operators H_0 and $H_0 + V$ are continuous.

From Eq. (2.24) it follows that

$$|\psi\rangle = \frac{1}{E - H_0} V |\psi\rangle + |\vec{p}\rangle, \quad (2.25)$$

which guarantees that application of the operator $(E - H_0)$ to the Eq. (2.25) results in the second equation from the set (2.24).

In order to deal with a singular operator $\frac{1}{E - H_0}$ in Eq. (2.25), the well-known technique is used to make such an operator complex by adding a small imaginary number to the denominator so Eq. (2.25) becomes

$$|\psi\rangle = G_0(E \pm i\epsilon)V |\psi\rangle + |\vec{p}\rangle, \quad (2.26)$$

where G_0 is a free propagator:

$$G_0(z) = \frac{1}{z - H_0}. \quad (2.27)$$

Solution with $G_0(E - i\epsilon)$ corresponds to the incoming spherical wave, while $G_0(E + i\epsilon)$ - to the outgoing one. Since we are interested in the final scattering state, only the (+) sign survives.

Eq. (2.26) is known as the Lippmann-Schwinger equation (LSE). Defining the transition operator t :

$$t |\vec{p}\rangle = V |\psi\rangle \quad (2.28)$$

we can rewrite it as

$$|\psi\rangle = (1 + G_0(E + i\epsilon)t) |\vec{p}\rangle. \quad (2.29)$$

With substitution of Eq. (2.26) into Eq. (2.28) we find an explicit form of the t operator:

$$\begin{aligned} t |\vec{p}\rangle &= V G_0(E + i\epsilon) V |\psi\rangle + V |\vec{p}\rangle = \\ &= V G_0(E + i\epsilon) t |\vec{p}\rangle + V |\vec{p}\rangle \end{aligned} \quad (2.30)$$

Getting rid off the initial state $|\vec{p}\rangle$ in the Eq. (2.30) we can get the LSE for the transition operator in the iterative operator form:

$$\begin{aligned} t &= V + V G_0 t = \\ &= V + V G_0 V + V G_0 V G_0 V + \dots, \end{aligned} \quad (2.31)$$

which constitutes an infinite series of subsequent NN interactions and free propagators of nucleons.

In the partial-wave representation, the LSE Eq. (2.30) expresses as:

$$\begin{aligned} \langle p'(l's')j'm_{j'} | \langle t'm_{t'} | t(E) | t m_t \rangle | p(ls)j m_j \rangle &= \langle p'(l's')j'm_{j'} | \langle t'm_{t'} | V | t m_t \rangle | p(ls)j m_j \rangle + \\ &+ \sum_{\alpha''} \int_0^\infty dp'' p''^2 \langle p'(l's')j'm_{j'} | \langle t'm_{t'} | V | t''m_{t''} \rangle | p''(l''s'')j''m_{j''} \rangle \\ &\times \frac{1}{E + i\epsilon - p''^2/m} \langle p''(l''s'')j''m_{j''} | \langle t''m_{t''} | t(E) | t m_t \rangle | p(ls)j m_j \rangle, \end{aligned} \quad (2.32)$$

which after using symmetries of potential matrix elements (2.19) reduces to

$$\begin{aligned} \langle p'(l's')jt | t(E) | p(ls)jt \rangle &= \langle p'(l's')jt | V | p(ls)jt \rangle + \\ &+ \sum_{l''} \int_0^\infty dp'' p''^2 \langle p'(l's')jt | V | p''(l''s)jt \rangle \\ &\times \frac{1}{E + i\epsilon - p''^2/m} \langle p''(l''s)jt | t(E) | p(ls)jt \rangle. \end{aligned} \quad (2.33)$$

I solve Eq. (2.33) numerically, which again requires discretisation and therefore leads to a set of linear equations. Finally, using Eq. (2.29) and denoting the momentum state

of two nucleons with spin projections m_d and m_n as $\langle \phi_{m_d m_n} |$, we can write Eq. (2.1) as

$$N^\mu = \langle \phi_{m_d m_n} | (1 + G_0(E + i\epsilon)t) J^\mu | \Psi_{deuteron} \rangle \quad (2.34)$$

2.3 3N bound state

The 3N bound state is described by the Schrödinger equation for 3N system, with Hamiltonian comprising two- and three- nucleon interaction. The bound state total wave function $|\Psi\rangle$ obeys the following equation:

$$|\Psi\rangle = G_0(E + i\epsilon) \sum_{j=1}^3 (V_j + V_4^j) |\Psi\rangle, \quad (2.35)$$

where G_0 is a 3N free propagator as in Eq. (2.27), V_j - is a two-body potential acting between nucleons k and l (j, k and l - numerate nucleons, $j, k, l \in 1, 2, 3$ and $j \neq k \neq l$), V_4^j is a component of three-body potential $V_4 = \sum_{j=1}^3 V_4^j$ symmetrical under exchange of nucleons k and l , and E - is a 3N binding energy.

Eq. (2.35) can be split into three independent equations for so-called Faddeev components $|\psi_j\rangle$

$$|\Psi\rangle = \sum_{j=1}^3 |\psi_j\rangle, \quad (2.36)$$

which fulfills separately

$$|\psi_j\rangle = G_0(E + i\epsilon)(V_j + V_4^j) |\Psi\rangle. \quad (2.37)$$

Next, I introduce a permutation operator P , which is a combination of operators P_{jk} :

$$P = P_{12}P_{23} + P_{13}P_{32}. \quad (2.38)$$

The operator P_{jk} acting on the state interchange the momenta and quantum numbers of the nucleons j and k .

Using definitions (2.38) and (2.36), one can rewrite Eq. (2.37) as:

$$|\psi_j\rangle = G_0(E + i\epsilon)t_j P |\psi_j\rangle + (1 + G_0(E + i\epsilon)t_j)G_0(E + i\epsilon)V_4^j(1 + P) |\psi_j\rangle, \quad (2.39)$$

where t_j is a two-body t-operator which obeys Eq. (2.30) for corresponding two-body potential V_j . I solve Eq. (2.39) numerically to find $|\psi_j\rangle$ and the binding energy E . To do that, I perform PWD again.

The partial wave representation of the Eq. (2.39) is obtained using following 3N states:

$$|p, q, \alpha_{J, M_J}\rangle = \left| p, q, (ls)j, (\lambda, \frac{1}{2})I(jI)JM; (t\frac{1}{2})TM_T \right\rangle_1, \quad (2.40)$$

where index 1 states the choice of the Jacobi momenta, such that p is a relative momentum of the nucleons 2 and 3. Values l, s , and j are quantum numbers in the two-body subsystem consisting of nucleons 2 and 3. λ is the orbital angular momentum with respect to the c.m. of the particles 2 and 3, of the first particle which spin is $\frac{1}{2}$ and I is its total

angular momentum. J and M_J are the total angular momentum of the 3N system and its projection on the z-axis respectively. t is a total isospin of the 2-3 subsystem whereas T and M_T are the total isospin of the 3N system and its projection on the z-axis, respectively. The Jacobi momenta \vec{p} and \vec{q} for three particles with individual momenta $\vec{k}_i, i = 1, 2, 3$ are defined as [48]:

$$\begin{aligned}\vec{p}_i &= \frac{1}{2}(\vec{k}_j - \vec{k}_k), \\ \vec{q}_i &= \frac{1}{3}(2\vec{k}_i - \vec{k}_j - \vec{k}_k), \quad \{i, j, k\} = \{1, 2, 3\}, \{2, 3, 1\}, \{3, 1, 2\}.\end{aligned}\quad (2.41)$$

2.4 3N scattering state

Let us introduce an asymptotic state $|\Phi_j^{3N}\rangle$ describing a free motion of three nucleons j, k, l with particles k and l having relative momentum \vec{p} and particle j moving with momentum \vec{q} with respect to the center of mass $(k - l)$ subsystem:

$$|\Phi_j^{3N}\rangle \equiv \frac{1}{\sqrt{2}}(1 - P_{kl}) |\vec{p}(kl)\vec{q}(j)\rangle. \quad (2.42)$$

The Jacobi momenta \vec{p} and \vec{q} build the total energy of three nucleons in the 3N-c.m. system:

$$E_{3N} = \frac{|\vec{p}|^2}{m} + \frac{3|\vec{q}|^2}{4m}. \quad (2.43)$$

Using a free propagator $G(E_{3N} - i\epsilon)$ we can come up with the total 3N scattering state

$$|\Psi^{(-)}\rangle^{3N} = \frac{1}{\sqrt{3}} \sum_j |\Psi_j^{(-)}\rangle^{3N}, \quad (2.44)$$

where auxiliary scattering states $|\Psi_j^{(-)}\rangle^{3N}$ are defined as [48]

$$|\Psi_j^{(-)}\rangle^{3N} \equiv \lim_{\epsilon \rightarrow 0} i\epsilon G(E_{3N} - i\epsilon) |\Phi_j^{3N}\rangle. \quad (2.45)$$

The state $|\Psi_j^{(-)}\rangle^{3N}$ together with the state $|\Phi_j^{3N}\rangle$ fulfills an equation [48]

$$|\Psi_j^{(-)}\rangle^{3N} = |\Phi_j^{3N}\rangle + G_0 (V_1 + V_2 + V_3 + V_4) |\Psi_j^{(-)}\rangle^{3N}. \quad (2.46)$$

Defining the antisymmetrised Faddeev components, and using index "i" instead of "j"

$$|F_i^0\rangle \equiv G_0 (V_i + V_4^i) (1 + P) |\Psi_i^{(-)}\rangle^{3N} \quad (2.47)$$

we obtain a 3N scattering wave function as:

$$\begin{aligned}
 |\Psi^{(-)}\rangle^{3N} &= \frac{1}{\sqrt{3}} \left(\sum_{i=1}^3 |\Phi_i^{3N}\rangle + G_0 (V_1 + V_2 + V_3 + V_4) \sum_{i=1}^3 |\Psi_i^{(-)}\rangle^{3N} \right) \\
 &= \frac{1}{\sqrt{3}} \left(\sum_{i=1}^3 |\Phi_i^{3N}\rangle + \sum_{i=1}^3 |F_i^0\rangle \right) = \frac{1}{\sqrt{3}} (1 + P) (|\Phi_1^{3N}\rangle + |F_1^0\rangle).
 \end{aligned} \tag{2.48}$$

In this case the nuclear matrix element $N_\mu^{3N} = \langle \Psi^- | j^\mu | \psi_i \rangle$ (with $|\psi_i\rangle$ being the Faddeev component of the 3N bound state (2.36)) is [49–51]:

$$\begin{aligned}
 N_\mu^{3N} &= \frac{1}{\sqrt{3}} \langle \Phi_1^{3N} | (1 + P) j_\mu | \Psi_i \rangle + \frac{1}{\sqrt{3}} \langle \Phi_1^{3N} | t_1^+ G_0^+ (1 + P) j_\mu | \Psi_i \rangle \\
 &\quad + \frac{1}{\sqrt{3}} \langle \Phi_1^{3N} | t_1^+ G_0^+ P | U_\mu \rangle + \frac{1}{\sqrt{3}} \langle \Phi_1^{3N} | P | U_\mu \rangle,
 \end{aligned} \tag{2.49}$$

where U_μ fulfills the following equation:

$$\begin{aligned}
 |U_\mu\rangle &= \left[t_1^+ G_0^+ + \frac{1}{2} (1 + P) V_4^{(1)} G_0^+ (1 + t_1^+ G_0^+) \right] (1 + P) j_\mu | \Psi_i \rangle \\
 &\quad + \left[t_1^+ G_0^+ P + \frac{1}{2} (1 + P) V_4^{(1)} G_0^+ (1 + t_1^+ G_0^+) P \right] |U_\mu\rangle.
 \end{aligned} \tag{2.50}$$

Eq. (2.50) is being solved numerically in PWD scheme. The numerical techniques applied are the same as those presented in [49] for N-d elastic scattering.

2.5 Nd scattering state

Analogously to the bound and 3N scattering states, one can express a nucleon-deuteron scattering state using a permutation operator Eq. (2.38).

$$|\Psi^{(-)}\rangle^{Nd} = \frac{1}{\sqrt{3}} \sum_j |\Psi_j^{(-)}\rangle^{Nd} \tag{2.51}$$

Further a scattering state $|\Psi_j^{(-)}\rangle^{Nd}$ can be expressed in terms of asymptotic state $|\Phi_j^{Nd}\rangle$, in which particles k and l form a deuteron and the third particle (nucleon j) propagates freely with a relative momentum \vec{q}_0 with respect to the deuteron:

$$|\Psi_j^{(-)}\rangle^{Nd} \equiv \lim_{\epsilon \rightarrow 0} i\epsilon G(E_{Nd} - i\epsilon) |\Phi_j^{Nd}\rangle \tag{2.52}$$

$$|\Phi_j^{Nd}\rangle \equiv |\Phi_{d(k,l)}\rangle |\vec{q}_0\rangle, \tag{2.53}$$

where $|\Phi_{d(k,l)}\rangle$ is a deuteron wave function and $|\vec{q}_0\rangle$ - a free particle state and $G(t)$ is a free propagator of N-d pair. E_{Nd} is the total energy of the N-d system:

$$E_{Nd} = E_d + \frac{3|\vec{q}_0|^2}{4m}, \tag{2.54}$$

where E_d is the deuteron binding energy and m denotes the nucleon mass.

$|\Psi^{(-)}\rangle^{Nd}$ can be expressed by the Faddeev components

$$|\Psi^{(-)}\rangle^{Nd} = \frac{1}{\sqrt{3}}(1 + P)|F_1\rangle, \quad (2.55)$$

where

$$|F_1\rangle = |\phi_1^{Nd}\rangle G_0(V_1 + V_2 + V_3 + V_4) \sum_{j=1}^3 |\Psi_j^{(-)}\rangle^{Nd}. \quad (2.56)$$

The nuclear matrix element $N_\mu^{Nd} = {}^{Nd} \langle \Psi^- | j_\mu | \Psi_i \rangle$ (with Ψ_i - bound state) is now [49, 50]:

$$N_\mu^{Nd} = \frac{1}{\sqrt{3}} \langle \Phi_1^{Nd} | (1 + P) j_\mu | \Psi_i \rangle + \frac{1}{\sqrt{3}} \langle \Phi_1^{Nd} | P | U_\mu \rangle \quad (2.57)$$

with U_μ being a solution of Eq. (2.50). Fact that solving once Eq. (2.50) opens opportunity to compute both N_μ^{Nd} and N_μ^{3N} is a great advantage of the presented formulas.

2.6 Nuclear electromagnetic current

The electromagnetic current operator for 2N (3N) system is constructed from the one- and many-body currents:

$$j_\mu = j_\mu^1 + j_\mu^2 + j_\mu^3. \quad (2.58)$$

Here j_μ^n is a contribution from the interaction between a photon and n nucleons (obviously j_μ^3 is present in 3N system only). Each j_μ^n describes the interaction of photon with all relevant permutations of n nucleons, i.e. j_μ^1 is a sum of photon interactions with each of nucleons in the system separately.

In the case of the photodisintegration process, I will use only a single nucleon current (1NC), so I stick to its definition here. In the Hamiltonian framework, the nucleons are constrained to lie on the mass shell. The general current expression for a single nucleon at the spacetime point zero, denoted as $j_\mu^1(0)$, is computed between the initial nucleon momentum $p \equiv (p_0 = \sqrt{M_N^2 + \vec{p}^2}, \vec{p})$ and the final momentum $p' \equiv (p'_0 = \sqrt{M_N^2 + \vec{p}'^2}, \vec{p}')$ with the latter one constrained by the four-momentum transfer Q from photon to nucleon. This computation yields the following matrix elements:

$$\begin{aligned} \langle \vec{p}' | j_\mu^1(0) | \vec{p} \rangle &= \bar{u}(\vec{p}' s') (\gamma^\mu F_1 + i\sigma^{\mu\nu} (p' - p)_\nu F_2) u(\vec{p} s) \\ &= \bar{u}(\vec{p}' s') (G_M \gamma^\mu - F_2 (p' + p)^\mu) u(\vec{p} s). \end{aligned} \quad (2.59)$$

In the above equation, the symbols $u(\vec{p} s)$ represent Dirac spinors for particle having momentum \vec{p} and spin s , F_1 and F_2 are the Dirac and Pauli form factors of the nucleon, respectively, and $G_M \equiv F_1 + 2M_N F_2$ denotes the magnetic form factor of the nucleon. The proton charge e is extracted from the matrix element. Further γ^μ are Dirac matrices and $\sigma^{\mu\nu} = \frac{i}{2} [\gamma^\mu, \gamma^\nu]$. In this thesis, only the nonrelativistic limit of Eq. (2.59) is considered, which leads to well-known expressions for the operators for the single nucleon current [54]:

$$\langle \vec{p}' | j_0^1 | \vec{p} \rangle = (G_E^p \Pi^p + G_E^n \Pi^n), \quad (2.60)$$

$$\langle \vec{p}' | \vec{j}^1 | \vec{p} \rangle = \frac{\vec{p} + \vec{p}'}{2M_N} (G_E^p \Pi^p + G_E^n \Pi^n) + \frac{i}{2M_N} (G_M^p \Pi^p + G_M^n \Pi^n) \vec{\sigma} \times (\vec{p}' - \vec{p}). \quad (2.61)$$

The electric form factor denoted as G_E is defined as $G_E \equiv F_1 + \frac{(p'-p)^2}{2M_N} F_2$ and represents the neutron (n) and proton (p) form factors. Both electric and magnetic form factors, $G_E(Q^2)$ and $G_M(Q^2)$, are normalized as:

$$\begin{aligned} G_E^n(0) &= 0 \\ G_E^p(0) &= 1 \\ G_M^n(0) &= -1.913 \\ G_M^p(0) &= 2.793 \end{aligned} \quad (2.62)$$

The above values correspond to nucleons with point-like characteristics. While all the form factors depend on the squared four-momentum transfer $(p' - p)^2$, in the nonrelativistic regime, it is common to use as arguments of G_E and G_M the squared three-momentum transfer $-(\vec{p}' - \vec{p})^2$ or even set it to zero for interactions involving real photons. Numerous authors have investigated the properties of electromagnetic nucleon form factors through theoretical and experimental approaches, as discussed in [52, 53] but at low energies discussed here, all models lead to practically the same values of the form factors. Π^p (Π^n) in Eq. (2.61) is a proton (neutron) isospin projection operator.

The two-nucleon current contribution is in that work taken into account via Siegert approach [45, 46, 54]. To do that we break down the single nucleon current matrix elements into multipole components and represent some of the electric multipoles using the Coulomb multipoles, which arise from the single nucleon charge density operator [54]. This is acceptable because, in low-energy regime, contributions from many nucleons to the nuclear charge density are typically small. We then obtain the rest of the electric multipoles and all of the magnetic multipoles exclusively from the single nucleon current operators.

In 3N system we have following expressions for the 1NC:

$$\begin{aligned} \langle \vec{p}', \vec{q}' | j_0^1 | \vec{p}, \vec{q} \rangle &= \int d\vec{p}'' d\vec{q}'' \left\langle \vec{p}', \vec{q}' \left| \frac{1}{2} (1 + \tau(1)_z) F_1^p + \frac{1}{2} (1 - \tau(1)_z) F_1^n \right| \vec{p}'', \vec{q}'' \right\rangle \\ &\quad \left\langle \vec{p}'', \vec{q}'' - \frac{2}{3} \vec{Q} \left| \vec{p}, \vec{q} \right\rangle \right. \end{aligned} \quad (2.63)$$

$$\begin{aligned} \langle \vec{p}', \vec{q}' | j_{\pm}^{1, \text{conv}} | \vec{p}, \vec{q} \rangle &= \frac{1}{m} \int d\vec{p}'' d\vec{q}'' \langle \vec{p}', \vec{q}' | \left[\frac{1}{2} (1 + \tau(1)_z) F_1^p + \frac{1}{2} (1 - \tau(1)_z) F_1^n \right] q_{\pm} \\ &\quad | \vec{p}'', \vec{q}'' \rangle \left\langle \vec{p}'', \vec{q}'' - \frac{2}{3} \vec{Q} \left| \vec{p}, \vec{q} \right\rangle \right. \end{aligned} \quad (2.64)$$

$$\begin{aligned} \langle \vec{p}', \vec{q}' | j_{\pm}^{1, \text{spin}} | \vec{p}, \vec{q} \rangle &= \frac{i}{2m} \int d\vec{p}'' d\vec{q}'' \langle \vec{p}', \vec{q}' | \\ &\quad * \left[\frac{1}{2} (1 + \tau(1)_z) (F_1^p + 2mF_2^p) + \frac{1}{2} (1 - \tau(1)_z) (F_1^n + 2mF_2^n) \right] \\ &\quad * (\vec{\sigma}(1) \times \vec{Q})_{\pm} | \vec{p}'', \vec{q}'' \rangle \left\langle \vec{p}'', \vec{q}'' - \frac{2}{3} \vec{Q} \left| \vec{p}, \vec{q} \right\rangle. \end{aligned} \quad (2.65)$$

In Eq. (2.64) and Eq. (2.65) we present convection and spin currents which combined form a spatial component of the single nucleon current $\vec{j}^1(\mu) \equiv \vec{j}^1(\mu, \text{conv}) + \vec{j}^1(\mu, \text{spin})$. In my thesis I use a model of M. Garu and W. Krümpelmann [55] for which:

$$F_1^p(0) = 1 \quad 2mF_2^p(0) = 1.793 \quad (2.66)$$

$$F_1^n(0) = 0 \quad 2mF_2^n(0) = -1.913 \quad (2.67)$$

2.7 Pion absorption

For the pion absorption, I include explicitly two nucleon current (2NC) as well as 1NC. Thus the absorption operator is $\rho = \rho(1) + \rho(1, 2)$, where absorption on a single nucleon is included in $\rho(1)$ and $\rho(1, 2)$ plays a role of two-body charge current. The matrix element of the single nucleon pion absorption operator $\rho(1)$ in momentum-space for nucleon 1 relies on the nucleon's incoming momentum (\vec{p}) and outgoing momentum (\vec{p}') [56]:

$$\langle \vec{p}' | \rho(1) | \vec{p} \rangle = -\frac{g_A M_{\pi}}{\sqrt{2} F_{\pi}} \frac{(\vec{p}' + \vec{p}) \cdot \vec{\sigma}_1}{2M} (\vec{\tau}_1)_-, \quad (2.68)$$

where the values of the nucleon axial vector coupling, pion decay constant, and negative pion mass are $g_A = 1.29$, $F_{\pi} = 92.4 \text{ MeV}$, and $M_{\pi} = 139.57 \frac{\text{MeV}}{c^2}$, respectively. $\rho(1)$ operates in the spin and isospin spaces and involves the Pauli spin (isospin) operator $\vec{\sigma}_1$ ($\vec{\tau}_1$) for nucleon 1 and the isospin lowering operator $(\vec{\tau}_1)_- \equiv ((\vec{\tau}_1)_x - i(\vec{\tau}_1)_y)/2$. As before I use the average "nucleon mass" $M \equiv \frac{1}{2}(M_p + M_n)$ where the proton mass is M_p and neutron mass is M_n .

The 2N part of ρ at LO has the form [57]

$$\begin{aligned} \langle \vec{p}'_1, \vec{p}'_2 | \rho(1, 2) | \vec{p}_1, \vec{p}_2 \rangle &= \left(v(k_2) \vec{k}_2 \cdot \vec{\sigma}_2 - v(k_1) \vec{k}_1 \cdot \vec{\sigma}_1 \right) \\ &\quad \times \frac{i}{\sqrt{2}} \left[(\vec{\tau}_1 \times \vec{\tau}_2)_x - i(\vec{\tau}_1 \times \vec{\tau}_2)_y \right], \end{aligned} \quad (2.69)$$

where $\vec{k}_1 = \vec{p}'_1 - \vec{p}_1$, $\vec{k}_2 = \vec{p}'_2 - \vec{p}_2$ and the formfactor $v(k)$ reads

$$v(k) = \frac{1}{(2\pi)^3} \frac{g_A M_\pi}{4F_\pi^3} \frac{1}{M_\pi^2 + k^2}. \quad (2.70)$$

In the case of the pion absorption process, we follow a standard procedure including partial wave states for both 2N and 3N induced nuclei. It occurs that in such a case one needs current matrix elements. For 2N this is $\langle \vec{p} + \frac{1}{2}\vec{P}_f | \rho(1) | \vec{p} - \frac{1}{2}\vec{P}_f + \vec{P}_i \rangle$ and for 3N case $\langle \vec{q} + \frac{1}{3}\vec{P}_f | \rho(1) | \vec{q} - \frac{2}{3}\vec{P}_f + \vec{P}_i \rangle$.

For the $\pi^- + {}^2\text{H} \rightarrow n + n$ reaction, the nuclear matrix element for the transition operator is given by:

$$N_{nn}(m_1, m_2, m_d) = {}^{(-)} \langle \vec{p}_0 m_1 m_2 \vec{P}_f = 0 | \rho | \phi_d m_d \vec{P}_i = 0 \rangle, \quad (2.71)$$

where $|\vec{p}_0 m_1 m_2 \vec{P}_f = 0\rangle^{(-)}$ denotes the 2N scattering state [58]. The total absorption rate for this reaction expresses as:

$$\Gamma_{nn} = \frac{(\alpha M'_d)^3 c M_n p_0}{2M_{\pi^-}} \int d\hat{p}_0 \frac{1}{3} \sum_{m_1, m_2, m_d} |N_{nn}(m_1, m_2, m_d)|^2. \quad (2.72)$$

Turning to 3N system I investigate pion absorption in ${}^3\text{He}$ or ${}^3\text{H}$ with various final states. For $\pi^- + {}^3\text{He} \rightarrow n + d$ reaction the most important step in obtaining predictions is calculating the matrix element of the 3N transition operator ρ_{3N} , which is the ρ acting between the initial ${}^3\text{He}$ and the final Nd scattering state immersed in 3N space:

$$N_{nd}(m_n, m_d, m_{3\text{He}}) \equiv {}^{(-)} \langle \Psi_{nd} m_n m_d \vec{P}_f = 0 | \rho_{3N} | \Psi_{3\text{He}} m_{3\text{He}} \vec{P}_i = 0 \rangle. \quad (2.73)$$

Given Eq. (2.73) the total absorption rate may be obtained from the following:

$$\Gamma_{nd} = \mathcal{R} \frac{16 (\alpha^3 M'_{3\text{He}})^3 c M q_0}{9M_{\pi^-}} \int d\hat{q}_0 \frac{1}{2} \sum_{m_n, m_d, m_{3\text{He}}} |N_{nd}(m_n, m_d, m_{3\text{He}})|^2, \quad (2.74)$$

where $M'_{3\text{He}} = \frac{M_{3\text{He}} M_{\pi^-}}{M_{3\text{He}} + M_{\pi^-}}$ is now the reduced mass of the $\pi^- - {}^3\text{He}$ system. The factor $\mathcal{R} = 0.98$ appears due to the finite volume of the ${}^3\text{He}$ charge [59]. The final state energy is expressed in terms of the neutron momentum \vec{q}_0

$$M_\pi + M_{3\text{He}} \approx M_n + M_d + \frac{3}{4} \frac{\vec{q}_0^2}{M}, \quad (2.75)$$

The full 3N breakup is calculated in a similar way and the total absorption rate for $\pi^- + {}^3\text{He} \rightarrow p + n + n$ reaction is defined as follows

$$\begin{aligned} \Gamma_{pnn} = \mathcal{R} \frac{16 (\alpha M'_{3\text{He}})^3 c M}{9M_{\pi^-}} \int d\hat{q} \int_0^{2\pi} d\phi_p \int_0^\pi d\theta_p \sin \theta_p \\ \times \int_0^{p_{max}} dp p^2 \sqrt{\frac{4}{3} (ME_{pq} - p^2)} \frac{1}{2} \sum_{m_1, m_2, m_3, m_{3\text{He}}} |N_{pnn}(m_1, m_2, m_3, m_{3\text{He}})|^2 \end{aligned} \quad (2.76)$$

with

$$N_{pnn}(m_1, m_2, m_3, m_{3\text{He}}) \equiv {}^{(-)} \left\langle \Psi_{pnn} m_1 m_2 m_3 \vec{P}_f = 0 \left| \rho_{3N} \right| \Psi_{3\text{He}} m_{3\text{He}} \vec{P}_i = 0 \right\rangle \quad (2.77)$$

E_{pq} is the internal energy of the final 3N state and can be expressed in terms of the Jacobi relative momenta \vec{p} and \vec{q}

$$M_\pi + M_{3\text{He}} \approx 3M + \frac{\vec{p}^2}{M} + \frac{3}{4} \frac{\vec{q}^2}{M} \equiv 3M + E_{pq} = 3M + \frac{p_{max}^2}{M} = 3M + \frac{3}{4} \frac{q_{max}^2}{M}. \quad (2.78)$$

In Eq. (2.78) p_{max} and q_{max} are maximal kinematically allowed values of Jacobi momenta p and q , respectively.

Analogously, the total absorption rate for $\pi^- + {}^3\text{H} \rightarrow n + n + n$ reads

$$\begin{aligned} \Gamma_{nnn} = \frac{2 (\alpha M'_{3\text{H}})^3 c M}{27M_{\pi^-}} \int d\hat{\mathbf{q}} \int_0^{2\pi} d\phi_p \int_0^\pi d\theta_p \sin \theta_p \\ \times \int_0^{p_{max}} dp p^2 \sqrt{\frac{4}{3} (ME_{pq} - p^2)} \frac{1}{2} \sum_{m_1, m_2, m_3, m_{3\text{H}}} |N_{nnn}(m_1, m_2, m_3, m_{3\text{H}})|^2 \end{aligned} \quad (2.79)$$

with

$$N_{nnn}(m_1, m_2, m_3, m_{3\text{H}}) \equiv {}^{(-)} \left\langle \Psi_{nnn} m_1 m_2 m_3 \vec{P}_f = 0 \left| \rho_{3N} \right| \Psi_{3\text{H}} m_{3\text{H}} \vec{P}_i = 0 \right\rangle. \quad (2.80)$$

In the Results section, I also demonstrate (for processes with three free nucleons in the final state) predictions of the differential absorption rates. The natural domain is defined by energies of outgoing nucleons (E_1, E_2); in such a case the differential absorption rate $d^2\Gamma_{pnn}/(dE_1 dE_2)$ expresses as [58]

$$\begin{aligned} \frac{d^2\Gamma_{pnn}}{dE_1 dE_2} = \mathcal{R} \frac{64 \pi^2 (\alpha M'_{3\text{He}})^3 c M^3}{3M_{\pi^-}} \\ \times \frac{1}{2} \sum_{m_1, m_2, m_3, m_{3\text{He}}} |N_{pnn}(m_1, m_2, m_3, m_{3\text{He}})|^2. \end{aligned} \quad (2.81)$$

The kinematically allowed region is restricted to energies fulfilling the condition

$$-1 \leq \frac{E - 2E_1 - 2E_2}{2\sqrt{E_1 E_2}} \leq 1 \quad (2.82)$$

with $E = E_1 + E_2 + E_3$.

One can also calculate the differential absorption rate with respect to the dimensionless variables x and y which are frequently used in the literature, specifically to build so-called Dalitz plots [60]

$$\begin{aligned} x &= \sqrt{3}(E_1 + 2E_2 - E)/E, \\ y &= (3E_1 - E)/E. \end{aligned} \quad (2.83)$$

Such definition leads to a simple kinematically allowed region, namely to the disk $r^2 \equiv x^2 + y^2 \leq 1$. One can evaluate $d^2\Gamma_{pnn}/(dx dy)$ or (using polar coordinates) $d^2\Gamma_{pnn}/(dr d\phi)$ and relate it with $\frac{d^2\Gamma_{pnn}}{dE_1 dE_2}$. The same can be done for $\frac{d^2\Gamma_{nnn}}{dE_1 dE_2}$, $\frac{d^2\Gamma_{nnn}}{dx dy}$ and $\frac{d^2\Gamma_{nnn}}{dr d\phi}$.

2.8 Theoretical uncertainties

Striving to achieve valuable theoretical results, we cannot omit the estimation of their uncertainty. There are various sources of uncertainty appearing in predictions. The three most important are: the truncation error, the cutoff dependence and the uncertainty related to various models of nuclear interaction. The latter can be easily estimated by computing predictions arising from various models, see discussion below. The way how to estimate the first two types of uncertainties, together with a short discussion of the remaining sources of theoretical errors is given below.

Truncation error

As mentioned above, each subsequent order of the chiral expansion provides us with more and more sophisticated potential which is expected to increase the accuracy of data description. Starting from the leading order (LO) and coming next to NLO, N²LO, N³LO, etc., we take into account more topologies (equivalents of Feynmann diagrams) and resulting potential is expected to provide us with more precise predictions for the regarded process and observables. However, the chiral expansion (as any expansion) in principle can be continued up to the infinity, improving the resulting series. In practice, we are limited to finite, rather small, orders and we would like to find out the uncertainty appearing from cutting off the remaining part of the expansion. That type of theoretical uncertainty is called a truncation error. Various methods to estimate its value have been proposed [35, 61–64]. Typically predictions at lower orders serve as input information to get truncation error at given order. It is worth adding that Bayesian analysis is also used for truncation error estimation.

I use the method proposed in [62]. Let us regard some prediction $X^i(p)$ for observable X which is calculated at i -th order of the chiral expansion with the expansion parameter Q ($i = 0, 2, 3, \dots$)¹. Here p specifies a momentum scale of the reaction. In the case of photodisintegration, p is given by a photon's momentum.

¹As mentioned in Sec. 1, we do not have a first order of expansion because this term in the chiral expansion always vanishes and NLO corresponds to the quadratic term ($\nu = 2$)

If we define the difference between observables at each subsequent order as:

$$\Delta X^{(2)} = |X^{(2)} - X^{(0)}|, \quad \Delta X^{(i>2)} = |X^{(i)} - X^{(i-1)}|, \quad (2.84)$$

than chiral expansion for X can be written as:

$$X = X^{(0)} + \Delta X^{(2)} + \Delta X^{(3)} + \dots + \Delta X^{(i)}. \quad (2.85)$$

The truncation error at i -th order, $\delta X^{(i)}$, is estimated using values of the observable obtained at lower orders as follows:

$$\delta X^{(0)} = Q^2 |X^{(0)}|, \quad (2.86)$$

$$\delta X^{(i)} = \max_{2 \leq j \leq i} (Q^{i+1} |X^{(0)}|, Q^{i+1-j} |\Delta X^{(j)}|). \quad (2.87)$$

Additionally, following [62] I use the actual high-order predictions (if known) to specify uncertainties at lower orders, so that:

$$\delta X^{(i)} \geq \max_{j,k} (|X^{j \geq i} - X^{k \geq i}|) \quad (2.88)$$

and to be conservative I use additional restriction:

$$\delta X^{(i)} \geq Q \delta X^{(i-1)}. \quad (2.89)$$

All the conditions above assume that we use the whole available information at hand. In [65] it was shown that such a method is equivalent to the Bayesian approach proposed there.

Cut-off dependence

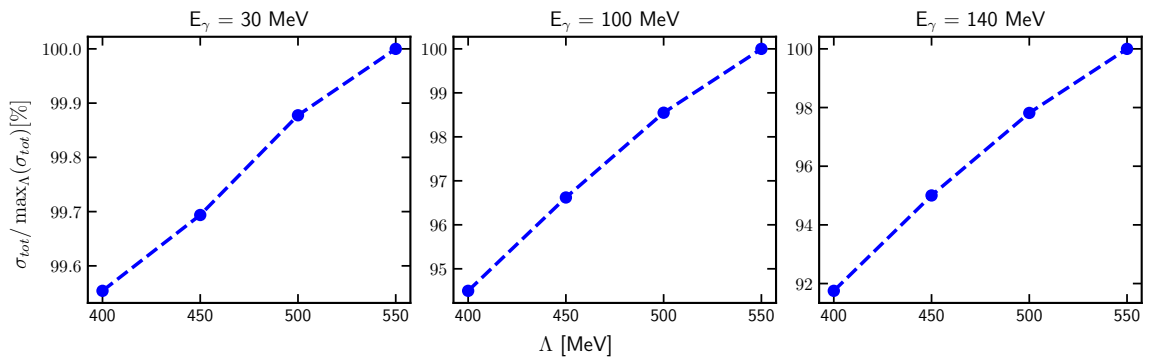


Figure 2.3: Total cross section of the deuteron photodisintegration process (normalized to the maximal cross section among all Λ) as a dependence of the cutoff parameter Λ for three photon energy E_γ values: 30, 100, and 140 MeV.

Another theoretical uncertainty comes from the choice of the cutoff parameter's value of regulator described in the Chapter 1.

In the case of the SMS interaction, its free parameters have been obtained from data for four values of the cutoff parameter Λ : 400, 450, 500 and 550 MeV [1]. Using each of these values, one obtains different predictions which, of course, can further differ from the actual (experimental) value. Therefore the choice of Λ value may affect the quality of the prediction.

To study that I also use the same four values of the Λ parameter, obtaining in that way a set of four predictions each time. That is exemplified in Fig. 2.3 for the deuteron photodisintegration cross section for the photon's energy $E_\gamma = 30$ MeV, 100 MeV and 140 MeV. The SMS model at $N^4\text{LO}^+$ with two-nucleon force is used. Each subfigure shows predictions for the total cross section as a function of the cutoff parameter, normalized to the maximum value among all cross sections obtained with various Λ . As we can see, there is almost linear dependence for that observable with a positive linearity coefficient value: with higher Λ the cross section value increases as well. Note that the higher the photon's energy is, the stronger becomes the cutoff dependence: for $E_\gamma = 30$ MeV the maximal difference between predictions is around 0.5 % while for 140 MeV it increases to more than 8 %. These results are generally within our expectations that the chiral model works better at smaller energies and is therefore less sensitive to the Λ value. Let us remind that Λ governs the behavior of the potential at small internucleon distances and only higher energy transfer probes that distances.

Other theoretical uncertainties

There are obviously more sources of theoretical uncertainties. Our model has several either intrinsic limitations in the precision or some simplifications which may be improved with further developments of the model.

Nuclear currents At the moment, our model is limited to a single nucleon current, which may not be sufficient to accurately describe the processes under consideration. This limitation will be further discussed and tested in Chapter 3. To address this issue, I utilize the Siegert theorem, which enables me to incorporate some contributions from the two-nucleon current, although it does not yet complete a job. It is worth noting that the incorporation of the two-nucleon current can significantly affect the predicted observables, as it includes additional physical effects that are not accounted for in the single-nucleon current. Therefore, the ongoing development of a complete chiral two-nucleon current is of great importance for our model to improve the accuracy of the predictions.

Nonrelativistic approach All the results presented here do not include relativistic corrections. At the lower energies, the relativistic contribution might not be crucial, but at the region with higher energy, we may see a lack of precision. This will be also confirmed and discussed on example of the total cross section for the deuteron photodisintegration (see Fig. 3.2).

Uncertainties in the potential free parameters Since not all the chiral potential parameters are given by the theory, the fitting-to-data procedure is applied to obtain the potential parameters [1]. The values of the free parameter of the SMS NN potential as well as free parameters of the 3N interaction have been obtained from the data by the least square fitting. As any fitting procedure, it introduces an uncertainty to the obtained values which depends on the algorithm's precision as these values are actually

estimators of expectation values only. These errors, in principle, are being propagated to the observables as different sets of parameters lead to different predictions. Indeed, in [1] the whole correlation matrix for free parameters of the SMS NN force is given. Using that knowledge, it is possible to study the propagation of the uncertainty of NN force parameters to 3N observables. It is done in [66,67] for the elastic and inelastic nucleon-deuteron scattering. Resulting uncertainties have been found to be much smaller (typically one order of magnitude) than uncertainties arising from truncation errors or from the cutoff dependence. I expect the same uncertainty level in electromagnetic processes and thus I do not intend to study that theoretical error in the presented thesis. Moreover, the estimation of such errors is computationally expensive, since it requires significant amount of computer processing power (separate calculations for each set of parameters). In the future, it could be interesting to check that type of uncertainty for photodisintegration processes but it should be done after completing all pieces of Hamiltonian, specifically after including many-body electromagnetic currents.

Uncertainties from the numerical method All my results are based on numerical calculations, so we can come up with a lot of places where numerical methods with limited precision comes into the scene. Our approach is based on partial wave decomposition and in practice only a limited number of partial waves is included (usually for 2N scattering we use all channels up to $j^{max} = 4$ which corresponds to 18 partial waves). For 3N calculations we use $j^{max} = 5$ and $J^{max} = 15/2$ which corresponds to 142 partial waves. In addition, I work with a grid of points which is used for the calculation of potential, wave function, numerical integration, etc. The choice of grid affects the final results' precision. Usually, we use a grid of 32 values which was proven to make resulting uncertainty very small [48].

Model choice I focus on the SMS potential, but using another model of interaction in general leads to different predictions. That difference is also a theoretical uncertainty thus we use predictions obtained with the semiphenomenological AV18 model to compare the chiral results. The AV18 model is a widely used and well-established model of nuclear interaction, which has been extensively tested and benchmarked against experimental data. By comparing the predictions obtained from the SMS potential with those obtained from the AV18 model, we can assess the robustness (compared to the AV18 results) of our results and determine the extent to which they depend on the choice of the interaction model. This comparison also helps to identify the strengths and weaknesses of each model and provides insights into the underlying physics of nuclear interactions.

Machine precision Finally, it should be noted that every computer calculation includes limited numerical machine precision which can be noticeable for complex calculations. We perform our calculations via CPU machine, where the particular choice of the processor and memory card may lead to numerical uncertainty. However, we have found that this uncertainty is much smaller than the uncertainties discussed above, and its impact on our results is negligible. We have taken great care to ensure that our calculations are performed using appropriate numerical methods and sufficient computational resources to minimize any numerical errors that may arise. This is done by careful choice of the Fortran compiler and compilation options.

CHAPTER 3

RESULTS

In this chapter, I will present the results of my calculations. I will begin with the deuteron photodisintegration process in Section 3.1, where I will provide predictions for the cross section (Subsection 3.1.1) and polarization observables (Subsection 3.1.2). Next, in Section 3.2, I will present my predictions for the observables in ^3He photodisintegration. Moving on to Section 3.3, I will give the results of calculations for Triton photodisintegration observables. Finally, in Section 3.4, I will discuss the results of the calculations for the pion absorption from the lowest atomic orbital of ^2H , ^3H , and ^3He .

3.1 Deuteron photodisintegration

3.1.1 Cross section

I will show the results of my calculation starting from the deuteron photodisintegration process. One of the most studying observable is obviously the cross section. There are several papers which present measurement results for both differential and total cross section [2, 68–75] and it is interesting to compare our predictions with that experimental results.

In Fig. 3.1 and Fig. 3.2 I present predictions for the total cross section σ_{tot} [μb] which I obtained using the chiral SMS potential at the N^4LO^+ order and with the cut-off parameter $\Lambda = 450$ MeV. From Fig. 3.1, we see that at low photon energies (below 50 MeV) both 1NC predictions and results which include 2N contributions to the electromagnetic current via the Siegert approach, describe experimental results quite well qualitatively. We observe that predictions based on the 1NC describe the data only up to approx. 10 MeV. Beyond that energy the 1NC current is clearly not enough to describe cross section as corresponding predictions are well below the data. In that region 1NC+Siegert predictions deliver better data description but overestimate the data. The difference between 1NC and 1NC+Siegert cross section grows with increasing photon energies. At 5 MeV the difference between 1NC predictions and 1NC+Siegert is $297.54 \mu\text{b}$ (10.8 %), increasing energy to 10 MeV it is $304.28 \mu\text{b}$ (20.4 %) and at 20 MeV it is $229.50 \mu\text{b}$ (39.2 %).

Here and later the relative difference between a set of predictions (x_1, x_2, \dots, x_N) is calculated using the formula:

$$\Delta = \frac{\max(x) - \min(x)}{\frac{1}{N} \sum_{i=1}^N x_i} \cdot 100\%, \quad (3.1)$$

so in the specific case of comparison the data with predictions based on 1NC current and "1NC + Siegert" we calculate the relative difference as $\Delta = \frac{|\sigma^{1NC+Siegert} - \sigma^{1N}|}{0.5(\sigma^{1NC+Siegert} + \sigma^{1N})}$.

From Fig. 3.1 we see that the gap between these predictions continues increasing even more with larger energies. The cross section predictions corrected via Siegert 2N contribution reproduce experimental data better than 1NC model. However, Fig. 3.1 reveals the approximated character of the Siegert approach. It is clear that one has to take with caution Siegert predictions at very small energies. Also above 20 MeV there is a gap between Siegert results and experimental data, which points that more elaborated 2N current should be included in the future. The observed discrepancy cannot be explained by the cut-off dependence (see e.g. Fig. 3.5b below) or by the low order of chiral potential (see e.g. Fig. 3.3 or Fig. 3.5a below).

While my main goal is to describe deuteron photodisintegration at energies $E_\gamma \lesssim 50$ MeV, where predictions seem to describe experimental data quite well, it is also interesting to check how present theory works at higher energies. Above $E_\gamma = 50$ MeV I find that the discrepancy with experimental data is not only quantitative but also qualitative see Fig. 3.2. This starts already above $E_\gamma = 50$ MeV and is especially pronounced at peak around 300 MeV seen in the experimental data from [72] which is not reflected in my predictions. The reason for such discrepancy is most likely coming from the relativistic effects which we do not take into account within this work. It is also confirmed by the calculations in [20], where authors discuss various NN potentials applied to the deuteron photodisintegration. Despite using much simpler models of the nuclear force than those used in this thesis, their predictions, which include some relativistic effects, show that such a peak appears in their predictions.

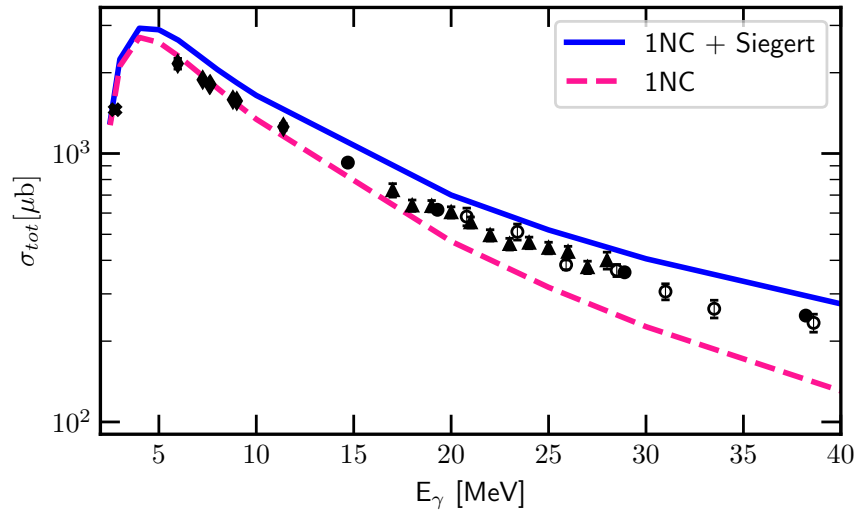


Figure 3.1: Total cross section σ_{tot} for the deuteron photodisintegration process as a function of the photon energy E_γ . The solid blue line presents results obtained with 1NC+Siegert and dashed pink line - predictions based on the 1NC. In both cases the SMS N^4LO^+ $\Lambda = 450$ MeV force is used. The experimental data are from [72] (black filled circles), [68] (empty circles), [2] (triangles), [70] (bold cross "X") and [71] (diamonds).

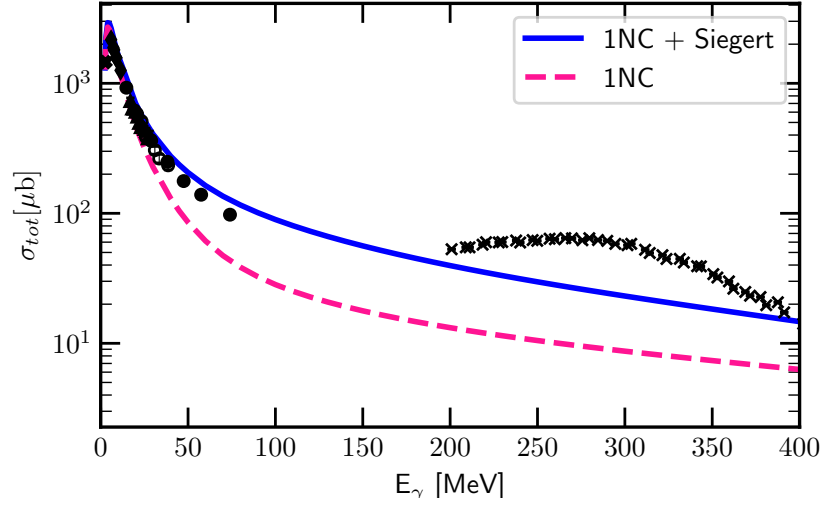


Figure 3.2: The same as in Fig. 3.1 but for the energy range 2.5 - 400 MeV. The experimental data are the same as in Fig. 3.1 but supplemented by the data above $E_\gamma = 200$ MeV from [69] (crosses).

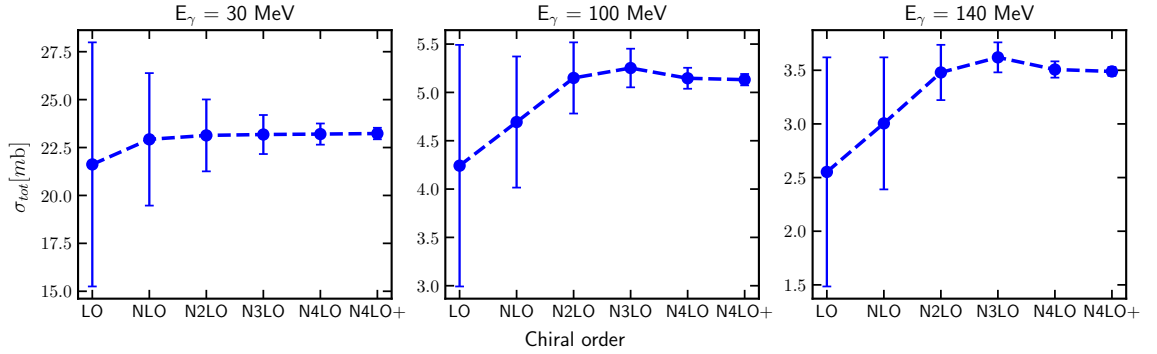


Figure 3.3: Total cross section for the deuteron photodisintegration process as a dependence on the chiral order for three photon energy E_γ values: 30, 100 and 140 MeV. Error bands show an estimated truncation error at each order.

In Fig. 3.3 I present the total cross-section for the deuteron photodisintegration at three photon energy values: 30, 100 and 140 MeV as a function of the chiral order. Error bars show truncation errors calculated using Eq. 2.86 - 2.89. One can see that the truncation errors are being reduced with each consecutive chiral order. At LO uncertainty is the biggest: 29.46 % at $E_\gamma = 30$ MeV, 29.46 % at $E_\gamma = 100$ MeV and 41.82 % at $E_\gamma = 140$ MeV. At N^4LO^+ it is hardly visible at the presented scale and amounts up to 1.3 % for each energy (however increasing with the reaction energy). For each energy, the prediction is within the uncertainty range at lower orders. We see that at lower energy σ_{tot} already at NLO reaches value which remains practically unchanged at higher orders. Contrarily, at two higher energies, contributions from higher orders are necessary to obtain stable predictions.

Figures 3.4 and 3.5 show my predictions for the differential cross section $\frac{d\sigma}{d\Omega}$. In both figures, the top, middle, and bottom row shows predictions at $E_\gamma = 30$, 100 and 140 MeV,

respectively. For all predictions, the contributions of the 2N current are taken into account via the Siegert theorem, and unless stated otherwise, I utilize the SMS $N^4\text{LO}^+$ potential. The left column of Fig. 3.4 shows the predictions obtained at different chiral orders (from LO to $N^4\text{LO}^+$) and with $\Lambda = 450$ MeV. Looking at the best predictions ($N^4\text{LO}^+$, $\Lambda = 450$ MeV) for each energy, I conclude that the higher the photon energy, the larger difference between the theoretical predictions and experimental data is. At $E_\gamma = 30$ MeV (top panel) my predictions almost perfectly match the data and the difference is almost always within the tripled experimental uncertainties. Moving to $E_\gamma = 100$ MeV (middle row) the description of the data is deteriorating: theoretical predictions still match the data qualitatively, but the gap for proton emission angle θ_p in range ($60^\circ < \theta_p < 130^\circ$) is up to 32 % (of the predicted value) and relative difference (calculated with Eq. (3.1)) is up to 7 %. At the highest energy (bottom row), it is even hard to say about good qualitative description: the general trend of the angular dependence is presented, but the predictions are far from the experimental points. The relative difference between experimental data and predictions obtained with $N^4\text{LO}^+$ and $\Lambda = 450$ MeV at 30 MeV is less than 13 % and absolute difference is $< 3.07 \frac{\mu\text{b}}{\text{sr}}$. At 100 MeV discrepancy is larger and the relative difference reaches 46% with absolute difference up to $1.39 \frac{\mu\text{b}}{\text{sr}}$. Coming to 140 MeV the relative difference increases up to 48.6 % and absolute - $1.93 \frac{\mu\text{b}}{\text{sr}}$. What may be helpful for a better data description is a 2N current and relativistic correction mentioned earlier. We observe improvements introduced by each subsequent chiral order, but stabilization shows that some ingredients beyond 2N potential are missing.

The obtained results at each energy confirm the convergence of the predictions concerning the chiral order. We see that the cross section at LO is far from both experimental data and the most advanced $N^4\text{LO}^+$ predictions, and the higher the photon energy, the larger this difference is. With each subsequent chiral order, the curves are more closer to each other and the difference between $N^4\text{LO}$ and $N^4\text{LO}^+$ is hardly visible at the scale used in Fig. 3.3. The relative difference between these two predictions at $E_\gamma = 30$ MeV around the point of maximum ($\theta_p = 80^\circ$) is 0.05 % which is $0.02 \frac{\mu\text{b}}{\text{sr}}$; at 100 MeV and $\theta_p = 107^\circ$ it is 0.79 % ($0.025 \frac{\mu\text{b}}{\text{sr}}$); and at 140 MeV (same angle) it is 1.8 % ($0.043 \frac{\mu\text{b}}{\text{sr}}$). Having such small differences between predictions from the two highest chiral orders, I can conclude that predictions are converged and using NN potential beyond $N^4\text{LO}^+$ chiral orders would rather not bring significant contribution to the cross section values. The difference with experimental data is systematic and is not related to the chiral order.

Predictions obtained with the AV18 potential (dashed-dotted purple line in the Fig. 3.4 left) are very similar to these from the $N^4\text{LO}^+$ SMS force at lower energies (relative difference at $E_\gamma = 30$ MeV is 0.06 % at the point of maximum $\theta_p = 80^\circ$) and with increasing energy to 140 MeV it grows up to 3.1 % at the same scattering angle. It can be connected with increasing uncertainty of the chiral potential, but AV18 can be struggling with high energies as well. The similar discrepancy with the data observed for both potentials once again shows that other components of Hamiltonian become important at that energies.

In the right column of the Fig. 3.4 I compare predictions based on various assumptions on nuclear current and dynamical mechanism. I again use SMS $N^4\text{LO}^+$, $\Lambda = 450$ MeV force. At the lowest energy predictions comprising the plane-wave component only (without rescattering part) and taking currents as SNC+Siegert, show relatively small deviation from the full predictions, but the difference increases at larger energies. At $E_\gamma = 30$ MeV the relative difference is 10 % ($4.03 \frac{\mu\text{b}}{\text{sr}}$) at $\theta_p = 80^\circ$. The same difference at 100 MeV and the same angle is 4 % ($0.21 \frac{\mu\text{b}}{\text{sr}}$) and at 140 MeV it is 7 % ($0.21 \frac{\mu\text{b}}{\text{sr}}$).

In contrast, predictions without a two-body current component (1NC) have a much larger gap with a full prediction: the difference is 46.5 % ($13.67 \frac{\mu\text{b}}{\text{sr}}$) at 30 MeV, 78.6 % ($2.88 \frac{\mu\text{b}}{\text{sr}}$) at 100 MeV and 77.8 % ($1.68 \frac{\mu\text{b}}{\text{sr}}$) at 140 MeV at the same $\theta_p = 80^\circ$. Obviously, 2NC contributions are extremely important in this case, the difference connected with them is much bigger than theoretical uncertainties or even rescattering contribution. For other scattering angles, especially $\theta_p = 0^\circ$ or $\theta_p = 180^\circ$, the role of two-body current or FSI is relatively even more pronounced.

The Fig. 3.5 (left) presents theoretical truncation uncertainties. That confirms our expectations that for the regarded photo reaction chiral order N^4LO^+ can produce converged predictions: the black band (representing truncation error at N^4LO^+) is hardly visible for the $E_\gamma = 30$ MeV (the relative error for N^4LO^+ at 80° is only 0.12 %) and is also quite narrow for larger energies (at 140 MeV the error at the same angle is 1.46 %). At the lower chiral orders, this band is obviously much wider: at N^2LO it is 1.25 % at $E_\gamma = 30$ MeV and 15.0 % at $E_\gamma = 140$ MeV. I note, that the magnitude of the truncation error is only very tiny depending on the scattering angle.

Last but not least, in the right column of Fig. 3.5 I show the cut-off dependence of the differential cross section. In the ideal case, that dependence is so weak that the choice of the parameter Λ would not introduce significant changes. In practice the choice of this parameter is important as it makes a noticeable variation in prediction at higher energies. Namely, at $E_\gamma = 30$ MeV the cut-off dependence is so tiny that, in fact, all the lines (for different Λ values) overlap each other and we cannot distinguish them with the naked eye: the relative difference at the maximum of the cross section is 0.08 %. This is approximately $\frac{2}{3}$ smaller than the truncation error discussed above. However, with increasing photon energy up to 100 MeV and 140 MeV (middle and bottom rows of the right column of Fig. 3.5) the spread becomes bigger: the uncertainty related to the Λ -dependence is 3.35 % at 100 MeV and 5.66 % at 140 MeV (the same θ_p). Thus at two higher energies, the cut-off dependence becomes more important than truncation errors at N^4LO^+ . That shows, that proper choice of the Λ is important. However, if I restrict myself to $\Lambda = 450$ MeV and 500 MeV, the dependence drops to 1.98 % at $E_\gamma = 140$ MeV. Such a restriction is advocated by a better description of the scattering data delivered by the SMS potential for those two values of Λ .

In the Fig. 2.3 we have already seen that the total cross section for the same energies has the cut-off spread around 4.5 % for 100 MeV and 8 % for 140 MeV. For $E_\gamma = 30$ MeV it is below 1 %. It means that even cut-off dependence for that total cross section remains relatively small, especially at the lower energies. Note, that the biggest relative difference arise from regions with θ_p close to 0° and 180° .

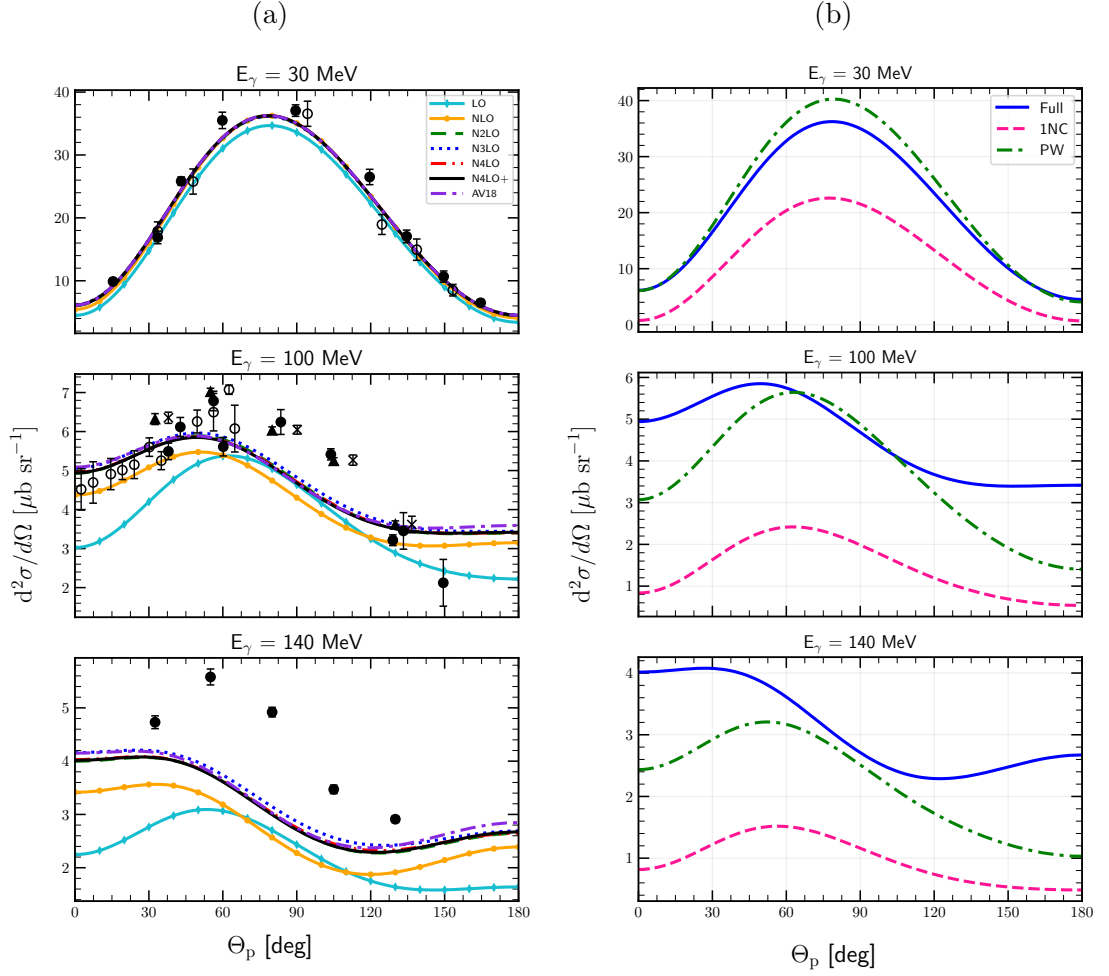


Figure 3.4: Differential cross section $\frac{d^2\sigma}{d\Omega}$ as a function of the outgoing proton momentum polar angle θ_p in the center of mass frame for the photon energy 30 MeV (top), 100 MeV (middle) and 140 MeV (bottom). **(a)** Results obtained using the SMS potential at different chiral orders (from LO to N^4LO^+) with the cut-off parameter $\Lambda = 450$ MeV and 2NC contributions taken via the Siegert theorem. For the sake of comparison, predictions obtained with the AV18 potential are shown by a dashed-dotted purple line. Data points (filled and empty circles) are from [74] for $E_\gamma = 30$ and 100 MeV and from [75] for $E_\gamma = 140$ MeV. **(b)** Predictions obtained with the chiral N^4LO^+ potential and $\Lambda = 450$ MeV with various models of nuclear current and scattering state. The blue solid curve represents our most complete predictions comprising the plane-wave plus rescattering parts and 1NC+Siegert current operator (the same as N^4LO^+ line in (a)). The pink dashed curve shows predictions obtained with the single-nucleon current only (without applying the Siegert theorem) and the green dashed-dotted curve represents predictions with the full current (1NC + Siegert) but plane-wave part only.

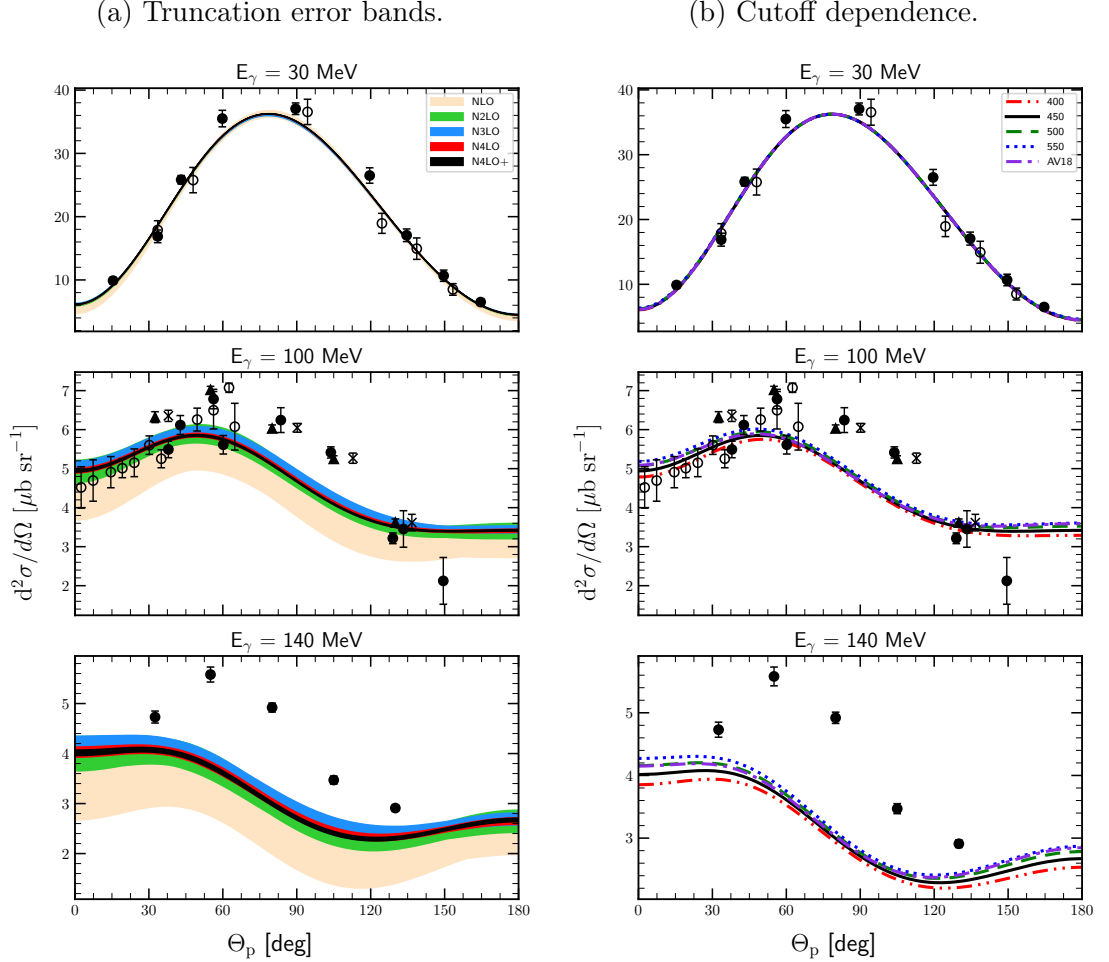


Figure 3.5: Theoretical uncertainties for the differential cross section $\frac{d^2\sigma}{d\Omega}$ as a function of the outgoing proton's momentum polar angle θ_p in the center of the mass frame for the photon energy 30 MeV (top row), 100 MeV (middle row), and 140 MeV (bottom row). **(a)** The truncation error bands obtained using the SMS potential at different chiral orders (from NLO to N⁴LO⁺) with the cut-off parameter $\Lambda = 450$ MeV and 2NC contributions taking via the Siegert approach. **(b)** Results obtained using different values of the cut-off parameter Λ . The double-dotted-dashed red curve, the solid black line, the dashed green line and the dotted blue line represents predictions obtained with $\Lambda = 400, 450, 500$ and 550 MeV respectively and the chiral potential N⁴LO⁺. Data points are the same as in Fig. 3.4a.

3.1.2 Polarization observables

In this subsection, I will present my predictions for the selected polarization observables in the deuteron photodisintegration process at two photon energies: $E_\gamma = 30$ MeV and $E_\gamma = 100$ MeV. A priori, various polarization states and measurements are thinkable for the $\gamma + d$ scattering. Polarization of the target deuteron leads to the deuteron analyzing power. Similarly using the polarized photons results in the photon asymmetry measurements. Using both polarized photon and deuteron allows for spin correlation measurement. Finally, detecting the spin polarization of at least one nucleon in the final state would deliver final polarization or spin transfer coefficients. However, such experiments are very challenging and, up to my best knowledge, have not been done yet at regarded here photon energies. Thus, in the following, I will restrict myself to results for polarization observables arising from the polarization of the initial particles.

I start with deuteron vector iT_{11} and tensor T_{20} , T_{21} and T_{22} analyzing power, which arises from various spin states of the deuteron.

Deuteron tensor analyzing powers can be calculated via cross section as it is defined in [73]:

$$\frac{d\sigma}{d\Omega} = \frac{d\sigma_0}{d\Omega} \left\{ 1 - \sqrt{3/4} P_z \sin \theta_H \sin \phi_H T_{11} + \sqrt{1/2} P_{zz} \left[(3/2 \cos^2 \theta_H - 1/2) T_{20} - \sqrt{3/8} \sin 2\theta_H \cos \phi_H T_{21} + \sqrt{3/8} \sin^2 \theta_H \cos 2\phi_H T_{22} \right] \right\}, \quad (3.2)$$

where σ_0 is the unpolarized cross section, P_z (P_{zz}) the vector (tensor) target polarization, θ_H - the angle between polarization axis and photon momentum, and ϕ_H - is the angle between the polarization plane (containing the polarization axis and momentum of the photon), and the reaction plane (containing the momenta of the proton and neutron).

In the Figures 3.6 (a, b) and 3.7(a,b) I show my predictions at $E_\gamma = 30$ MeV, for the T_{20} , T_{21} , T_{22} and iT_{11} respectively as functions of the outgoing proton momentum polar angle θ_p in the centre of the mass (CM) frame. Each of them is organized in a similar way: the top panel shows a dependence of the predictions on the chiral order of the potential. The middle subfigure is showing a correspondent truncation error for each of the predictions from a top row (except LO, because its uncertainty is too large and will spoil the clarity of the figure). The last (bottom) panel shows the cut-off dependence at the chiral order $N^4\text{LO}^+$. All results have been obtained using 1NC+Siegert model of nuclear current.

All the analyzing powers presented here show excellent convergence upon a chiral order as it is hard to distinguish the predictions from each subsequent order starting from the $N^2\text{LO}$. The relative width of the $N^4\text{LO}^+$ truncation band for T_{20} , T_{21} and T_{22} are 0.06 %, 0.05 % and 0.19 %, respectively (at $\theta_p = 90^\circ$, 60° and 90° , respectively). The slowest convergence is observed for iT_{11} (Fig. 3.7b) where we can recognize $N^2\text{LO}$ band in the figure. Nevertheless, at the $N^4\text{LO}^+$ the width truncation band at $\theta_p = 20^\circ$ (maximum point) is only a 0.2 %. The cut-off dependence for all regarded observables is weak and predictions for each value of the Λ are hardly separable with the naked eye. The relative spread of the predictions based on various Λ at the same angles as above are 0.87 %, 0.94 %, 3.42 % and 0.68 % for T_{20} , T_{21} , T_{22} and iT_{11} , respectively.

Corresponding predictions at the photon energy $E_\gamma = 100$ MeV (Figs. 3.8 and 3.9) preserve similar trends for each observable. In general, predictions are being converged starting even from the $N^2\text{LO}$ and only for the iT_{11} I find that truncation error's bands

are noticeably wide even at $N^4\text{LO}$ and $N^4\text{LO}^+$. Cutoff dependence at this energy is a bit stronger compared to those at $E_\gamma = 30\text{ MeV}$, especially for T_{22} and iT_{11} analyzing powers (Fig. 3.9 vs Fig. 3.7), where one can see the slightly stronger discrepancy at the maxima and minima points.

The choice of Λ does not affect predictions substantially even at that higher energy: the relative spread among all cut-offs for T_{20} is 1.54 % around the point of maximum ($\theta_p = 90^\circ$). For other components of the tensor analyzing power spread amounts up to: 0.14 % at $\theta_p = 60^\circ$ for T_{21} ; 3.68 % at $\theta_p = 90^\circ$ for T_{22} ; and 4.91 % at $\theta_p = 75^\circ$ for iT_{11} . We see again that iT_{11} has much larger spread in the maximum and is more sensitive to the cut-off choice. However, summarizing my findings for the deuteron tensor analyzing powers, I conclude that cut-off dependence is generally weak also at $E_\gamma = 100\text{ MeV}$.

Turning our attention to the chiral order convergence, we observe that predictions are mostly converged starting either from $N^2\text{LO}$ or $N^3\text{LO}$. The relative width of $N^4\text{LO}^+$ truncation band for T_{20} , T_{21} and T_{22} are 0.7 %, 0.7 % and 0.04 % respectively (at the same angles as used above). Another case is iT_{11} , for which this width is much larger: 6.8 % at $\theta_p = 20^\circ$. The truncation uncertainty for all analyzing powers is much lower than one, related to the choice of the cut-off parameter. However, iT_{11} seems to be more sensitive both to the choice of the cut-off parameter and to the chiral order than other regarded observables. Even for iT_{11} , the cut-off spread is almost twice larger than the truncation error. Standing out of other tensor components, iT_{11} can be useful for the investigation of the cut-off dependence of the model. Of course, we can repeat once more that our model is less accurate at higher energies which is reflected in a stronger cut-off dependence and slower chiral convergence. However, I conclude that even at these energies tensor analyzing powers are well converged with respect to the chiral order.

Comparison of the predictions obtained using the chiral $N^4\text{LO}^+$ potential $\Lambda = 450\text{ MeV}$ with ones obtained taking AV18 potential show a very good agreement: the relative difference at $E_\gamma = 30\text{ MeV}$ is below 6 % for the regarded tensor analyzing powers at specified angles. Picture at $E_\gamma = 100\text{ MeV}$ is even better: the difference does not exceed 4 % for all observables and a whole range of scattering angles.

In Fig. 3.10 together with our most advanced "Full" predictions ($N^4\text{LO}^+$, $\Lambda = 450\text{ MeV}$, the Siegert theorem), at $E_\gamma = 30\text{ MeV}$ I show predictions obtained with 1NC only and the Siegert predictions but with plane-wave contribution without rescattering part. In the case of deuteron's tensor analyzing power components, the contribution of rescattering part is important for T_{20} , T_{21} and T_{22} (the relative difference is up to 20 % in extremes). and crucial for iT_{11} where the PW part equals to zero. The 2NC component taken into account via Siegert theorem has a dominant contribution here. We see that 1NC predictions are absolutely away from the "Full" predictions and in the case of iT_{11} does not even reflect complete prediction qualitatively.

Fig. 3.11 presents similar results but for $E_\gamma = 100\text{ MeV}$ and it is interesting that the difference between Full and 1NC prediction becomes smaller and it is especially visible for T_{22} . At this energy, the relative difference between "Full" and 1NC predictions at $\theta_p = 90^\circ$ is 43.6 % compared to 122.8 % at $E_\gamma = 30\text{ MeV}$. Similarly, the difference for T_{20} at $E_\gamma = 30\text{ MeV}(\theta_p = 90^\circ)$ is 91.4 % and at $E_\gamma = 100\text{ MeV}$ it drops to 28.8 %. This may also be affected by the fact that values at $\theta_p = 90^\circ$ are quite small for the Full prediction, nevertheless, the difference still becomes smaller at the $E_\gamma = 100\text{ MeV}$. This trend is noticeable by looking also on the results presented below. Nevertheless, in both cases 2NC (via the Siegert) brings sufficient contributions and cannot be omitted for obtaining the full picture.

In the following figures, I will compare my predictions with experimental data. In some cases, I will keep a similar way as it was done in [73] where due to experimental conditions results are given not at single photon energy, but for a specific ranges of E_γ . In the Figures 3.12 - 3.18 I show an angular dependence of the T_{2i} ($i = 0, 1, 2$) for a specific energy bands: 25–45 MeV, 45–70 MeV, 70–100 MeV, and 230–330 MeV. The solid blue line shows an average value of the observable in the specified energy intervals: obtained at $N^4\text{LO}^+$ with $\Lambda = 450$ MeV, while the pink dashed line is a prediction obtained with the same setup but without using contributions from Siegert approach (single nucleon current only). Bands for each prediction specify the spread of predictions due to the energy band.

One clearly sees that the data description is better for the predictions with Siegert contributions included and the 1NC alone is not able to describe the experiment properly. Our Full model nicely describes data up to $E_\gamma = 70$ MeV. With increasing energy (above 100 MeV), the difference between predicted values and experimental data becomes larger (especially for T_{22}), which shows a necessity of improving the theoretical model before applying it to higher energies. Nevertheless, even with approximations used, the data description remains reasonable. We observe that quite often and in particular in Fig. 3.17 and Fig. 3.18 the data description is worse for smaller angles. Especially for the tensor analyzing power T_{22} the group of data point lying closer to $\theta_p = 30^\circ$ are farther from the theoretical prediction than second group. In Fig. 3.18 the description of data points for T_{20} seem to be better with the 1NC (dashed line), but in this case, it is only an accidental match as we do not observe similar trend for any other angular range or for different observables. In addition, experimental uncertainties are larger at small angles, and in all cases our description is inside 3σ uncertainty.

In the Figure 3.19 the energy dependence of T_{20} and T_{22} at specific angle $\theta_p = 88^\circ$ is presented for the energy range 0-400 MeV. Besides my predictions I also demonstrate the experimental data from [73] and [76] as well as theoretical calculations from [77]. For T_{20} all models are able to describe experimental data well even for high energies. On the other hand, T_{22} is not described so well: for the energies below 140 MeV the predictions are within uncertainties of experimental data, but further the difference with the data increases. Above 140 MeV Full predictions do not reflect the qualitative nature of the data. Namely, I observe that data points start ascending which is not represented in my predictions. Theoretical predictions from [77] (brown dashed curve) are also not able to describe data quantitatively for T_{22} , but increasing of T_{22} towards data is present. The predictions in [77] are obtained with a one-body current using the Bonn one-boson-exchange potential in coordinate space (OBEPR) NN potential with the major part of meson exchange currents (MEC) included implicitly via the Siegert operators plus explicit pion exchange currents (MEC), isobar configurations (IC) and the leading order of relativistic corrections (RC). So authors use a different potential, but probably the main difference in predictions is coming from the more advanced model of the current operator and the RC included there. We see that experimental errors are quite large which is not so surprising giving that the experiment was conducted back in 1989. New experiments would be a great support in development of the nuclear interactions as we expect relativistic calculations in the future [78].

The Fig. 3.20 presents similar results to the Fig. 3.19 but with various values of the cutoff parameter. The deviation between these predictions is rather small (especially below 150 MeV), while the difference with the calculation from [77] and experimental data remains as discussed above.

Similar picture is seen in the Figures 3.21 and 3.22 where I show an energy dependence of the mean of deuteron analyzing powers over specific angular ranges (following the data from [73]). In Fig. 3.21 we see that only predictions for T_{20} are able to reflect the experimental results, while for T_{21} and T_{22} my results are reasonable (quantitative-wise) only for lower energies and difference in data becomes larger when energy increases. Predictions for T_{21} and T_{22} once more confirm an insufficiency of 1NC and the importance of 2-nucleon current contributions. The description is better for bigger angles Fig. 3.22): at lower energies (below 140 MeV) the correspondence to experimental data is good for all three observables but above that threshold, all predictions (especially for T_{22}) move away from the measurement data. Again, big uncertainty of the data calls for the experiment to be repeated.

In the Fig. 3.23 I demonstrate predictions for the photon asymmetry Σ_γ for the deuteron photodisintegration with $E_\gamma = 20$ MeV (a) and 60 MeV (b) together with the experimental data of [79–82]. Both (a) and (b) figures are organized similarly to the figures I showed above for the tensor analyzing powers (e.g. Fig. 3.7). That is the top panel is aimed to demonstrate predictions obtained with the chiral SMS potential at different orders of the chiral expansion, the middle one shows a truncation error and the bottom one shows the cut-off dependence. For that observable we see an excellent convergence with respect to the chiral order. For both regarded energies predictions at different orders are very close to each other except the LO and NLO curves. Nevertheless, at $E_\gamma = 60$ MeV the truncation error bands reveal some uncertainty connected with the chiral order and it is expected that even some higher chiral orders would still contribute to the predictions at this energy. The relative width of the truncation band are 0.26 %, 5.04 %, 5.05 %, 5.73 % and 14.96 % for $N^4\text{LO}^+$, $N^4\text{LO}$, $N^3\text{LO}$, $N^2\text{LO}$ and NLO respectively and at $\theta_p = 90^\circ$.

The cut-off dependence is also much stronger at 60 MeV. One clearly sees that predictions are different for various values of the Λ . The relative difference between predictions to the cut-off parameter at 20 MeV is 0.26 % while at the photon energy 60 MeV it is 4.41 % (both calculated at $\theta_p = 90^\circ$). So the theoretical uncertainty related to regulator value is nearly 17 times bigger than due to the truncation error ($4.41/0.26 = 16.96$).

Comparing my predictions to experimental data, I observe that for the lower energy predictions are almost perfectly overlapping with experimental points within the error bars. For a few data points our predictions are outside data error bars, but they are still within 3σ range. For 60 MeV, experimental data points are systematically below theoretical curves, especially in the middle of the angular range. It seems that some systematic uncertainty is presented in predictions and ad hoc multiplication by some factor (around 0.8) could help predictions be more similar to experimental data. But very likely the observed discrepancy points to the simplified character of the model used here.

In the Fig. 3.24 the predictions obtained with the Full set of components (plane wave + rescattering and 1NC + Siegert, solid blue curve) are shown versus predictions obtained without rescattering (green dashed-dotted line) and without contribution from the Siegert (pink dashed line) for the same photon energies as above: $E_\gamma = 20$ MeV (left panel) and $E_\gamma = 60$ MeV (right panel). For the $E_\gamma = 20$ MeV the difference between Full and PW is quite small, whereas 1NC is noticeably differs from the Full prediction, especially around the smallest and largest angle values. For the $E_\gamma = 60$ MeV the difference between such predictions is larger: we see not only quantitative, but also qualitative variations. The 1NC curve has much larger values and its shape becomes more asymmetric with respect to the $\theta_p = 90^\circ$ point.

In the Fig. 3.25 (left) I present a dependence of the photon asymmetry Σ_γ on the photon energy at a fixed value of the outgoing proton polar direction $\theta_p = 90^\circ$ (following the data given at [83] and [80]). It is noticeable that with increasing energy, the predictions are systematically above the experimental data and the discrepancy grows with energy. This trend was also observed in the angular dependence of the asymmetry at 60 MeV so I conclude that within our framework, Σ_γ is sensitive to the initial photon energy and some theoretical contributions are missing to get satisfactory predictions at higher energies. From the Fig. 3.25 we can say that large discrepancy with data starts already above $E_\gamma = 35$ MeV.¹

The right panel of the Fig. 3.25 shows an impact of the different model components to the obtained predictions. We see that the difference between the Full predictions (solid blue line) and the one obtained with a 1NC only (without the Siegert contribution) is larger than the difference with predictions with plane-wave part only (without rescattering). Both these incomplete predictions are farther from the experimental data, (for PW at larger energies only) and have a different curve shape as well.

The proton polarization is demonstrated in Fig. 3.26 for the photon energy 30 MeV(a) and 100 MeV(b). In this case even at higher energy (such as 100 MeV) predictions reveal neither slower convergence concerning the chiral order nor stronger cut-off dependence. Figures for both energies show that only next-to-leading order brings a relatively high contribution while taking into account other subsequent orders does not change predictions significantly. In the case of the cut-off dependence, we see that curves for each value of Λ are very close to each other. The relative difference of the predictions with respect to the cut-off parameter is 4.04 % at the minimum point $\theta_p = 130^\circ$ of $E_\gamma = 30$ MeV and 5.62 % at $\theta_p = 160^\circ$ and $E_\gamma = 100$ MeV. The dependence is slightly stronger for higher energy, but both values are comparable. Again, the cut-off-related uncertainty exceeds the truncation error.

Predictions for the neutron polarization at the energies 2.75 MeV and 100 MeV are shown in the Fig. 3.27. The choice of energy is conditioned by the availability of experimental data, which were taken in 1965 in Livermore [84] and in 1986 at TRIUMF facility [85]. In the case of $E_\gamma = 2.75$ MeV (Fig. 3.27a), we see that predictions reflect the behavior of experimental data points qualitatively, having more or less a constant offset of the values. A similar offset was obtained also in [20], where various approaches were presented. Authors compare different models which leads to very similar theoretical results even though different potentials are used with and without relativistic correction. One of the theoretical predictions is included even in the experimental papers [84] and authors state that there might be a systematic error in the calibration of the analyzing power of the neutron polarimeter which could affect experimental results precision. Interestingly, predictions clearly show a symmetrical form of the curve, while the experimental data have some deviations from the symmetrical form. It can be a sign that some problem with the data can be in this case (taking into account also that the experiment had been done in 1965). In [84] authors even make a plot of the theoretical curve multiplied by the factor 0.879 which almost perfectly overlaps with experimental data afterward.

At the energy $E_\gamma = 100$ MeV (Fig. 3.27b) my predictions describe the data very well. For most of the data points, predicted values are within error bars, and only some of the points (e.g. around 50°) have a prediction in distance more than one standard deviation. Nevertheless, these data points look like they are out of general trend and may be a result

¹It is worth to note that data of [80] are above these from [83] (however still inside 3σ experimental error bands) and remain in agreement with my predictions even at $E_\gamma = 60$ MeV.

of imprecise measurement. Observing the stability of my predictions on the chiral order and regulator value I conclude that nucleon polarizations are not the observables, which, even measured with much better precision, than it was done in [84] or [85] would be an indicator of the model convergence or stability.

Concluding my results of the deuteron photodisintegration predictions, I can point that predictions for $E_\gamma = 30$ MeV (and lower) are very stable with respect to the potential parameters (chiral order or the regulator). It shows an ability for a good data description as well. For a higher energies (especially above 100 MeV) the quality of predictions becomes lower: the dependency on the cut-off value is higher as well as discrepancy with experimental data. Still, predictions are converged with respect to the chiral order. The general problem is a lack of 2N current and in the case of higher energies - relativistic corrections are missing.



Figure 3.6: The deuteron tensor analyzing powers T_{20} (a) and T_{21} (b) as a function of the outgoing proton angle θ_p in the centre of the mass frame for the photon energy $E_\gamma = 30$ MeV. The top row presents results obtained using the SMS potential at different chiral orders (from LO to $N^4\text{LO}^+$) with the cut-off parameter $\Lambda = 450$ MeV. The middle row shows truncation errors for each chiral order starting from NLO and the bottom row presents a cut-off dependence at $N^4\text{LO}^+$. For the sake of comparison, predictions obtained with the AV18 potential are given as well. For all predictions 1NC+Siegert model is used.



Figure 3.7: The same as in Fig. 3.6 but for the deuteron tensor analyzing power T_{22} (left column (a)) and the deuteron vector analyzing power iT_{11} (right column (b)).



Figure 3.8: The deuteron tensor analyzing powers T_{20} (a) and T_{21} (b) as a function of the outgoing proton angle θ_p in the center of mass frame for the photon energy $E_\gamma = 100$ MeV. The top row presents results obtained using the SMS potential at different chiral orders (from LO to $N^4\text{LO}^+$) with the cut-off parameter $\Lambda = 450$ MeV. The middle row shows truncation errors for each chiral order starting from NLO and the bottom row presents a cut-off dependence at $N^4\text{LO}^+$. For the sake of comparison, predictions obtained with the AV18 potential are given as well. For all predictions 1NC+Siebert model is used.



Figure 3.9: The same as in Fig. 3.8 but for the deuteron tensor analyzing power T_{22} (left column (a)) and the deuteron vector analyzing power iT_{11} (right column (b)).



Figure 3.10: The deuteron tensor analyzing powers T_{20} , T_{21} , T_{22} and the deuteron vector analyzing power iT_{11} as a function of the outgoing proton angle θ_p in the CM frame at $E_\gamma = 30$ MeV. Similarly to Fig. 3.4b predictions obtained with chiral $N^4\text{LO}^+$ potential and $\Lambda = 450$ MeV are presented for three theoretical models. The blue solid line is the most complete prediction we have (plane-wave plus rescattering parts, 1NC + Siegert), the pink dashed line shows predictions obtained with single-nucleon current only (1NC) - without the Siegert contributions and the green dashed-dotted line is a prediction in which we neglect the rescattering part and stick to the plane-wave part only but keeping the Siegert contributions.


 Figure 3.11: The same as in Fig. 3.10 but for $E_\gamma = 100$ MeV.


Figure 3.12: Tensor analyzing powers T_{20} , T_{21} and T_{22} as a function of the outgoing proton angle θ_p in the CM frame. The solid blue line is the mean value of my predictions obtained at energy values from 25 to 45 MeV with the SMS potential at $N^4\text{LO}^+$ chiral order and with $\Lambda = 450$ MeV and with 1NC used together with the Siegert approach. The pink dashed line is a similar prediction but with the 1NC only. The corresponding bands show the limits of predictions in the regarded energy region. Filled circles are experimental data from [73] for the same energy range.

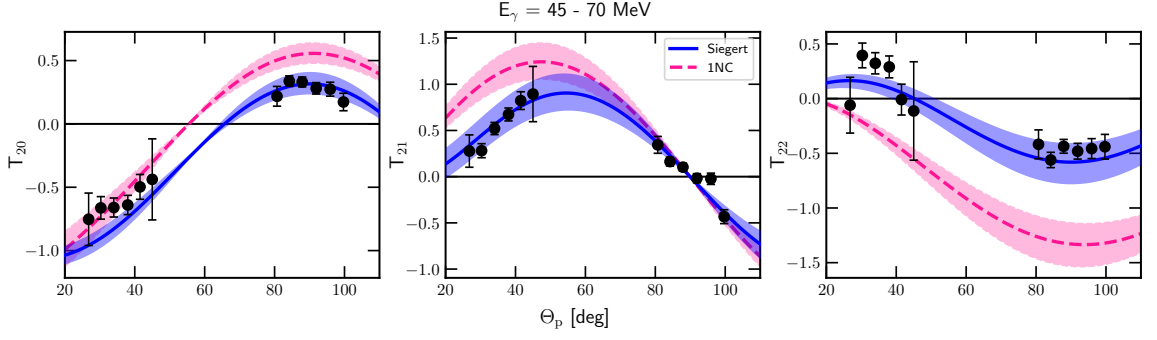


Figure 3.13: The same as in Fig. 3.12 but for energy bin 45 – 70 MeV.

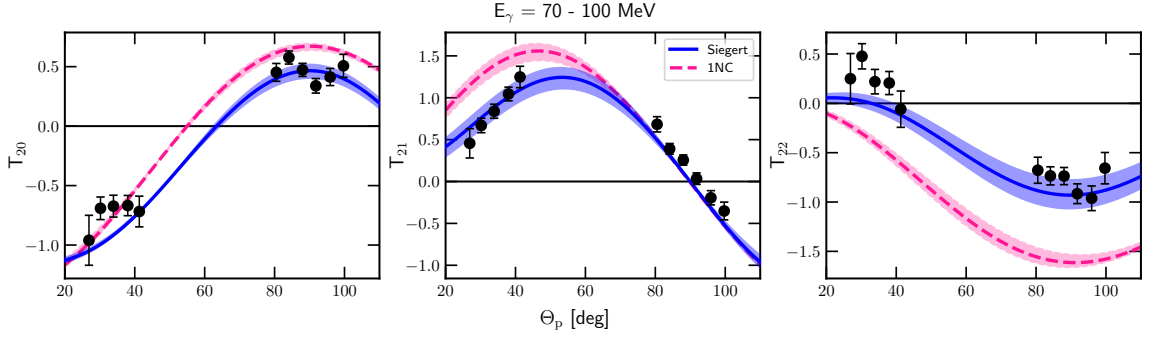


Figure 3.14: The same as in Fig. 3.12 but for energy bin 70 – 100 MeV.

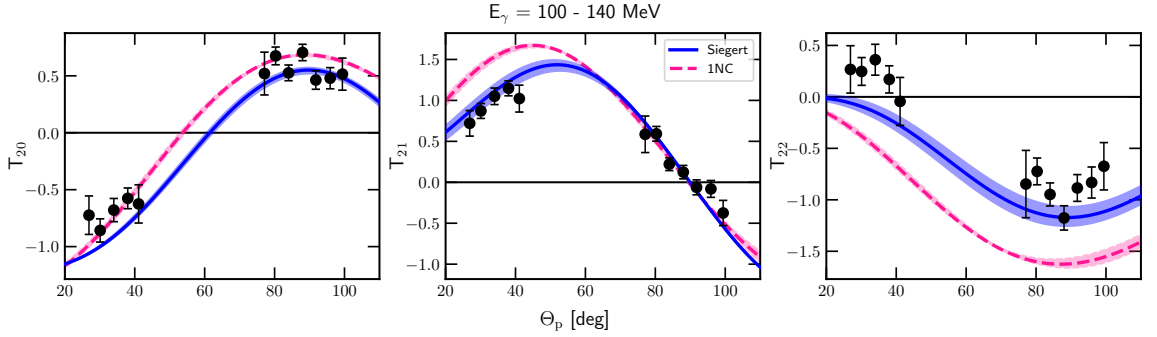


Figure 3.15: The same as in Fig. 3.12 but for energy bin 100 – 140 MeV.

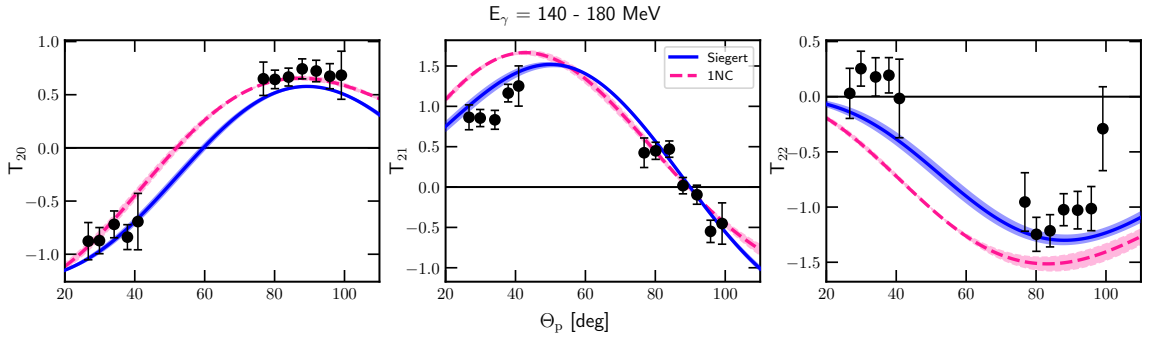


Figure 3.16: The same as in Fig. 3.12 but for energy bin 140 – 180 MeV



Figure 3.17: The same as in Fig. 3.12 but for energy bin 180 – 230 MeV



Figure 3.18: The same as in Fig. 3.12 but for energy bin 230 – 330 MeV

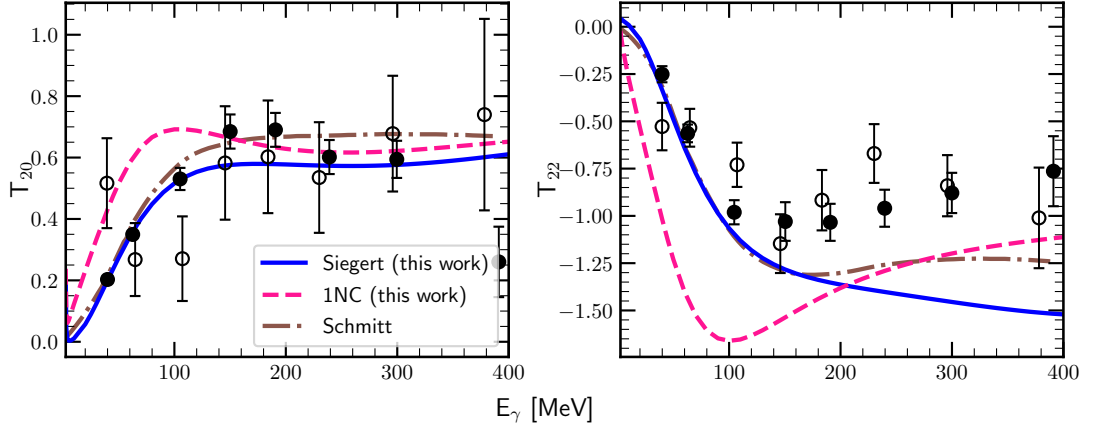


Figure 3.19: The tensor analyzing powers T_{20} (left) and T_{22} (right) as a function of the photon energy E_γ at fixed outgoing proton angle $\theta_p = 88^\circ$ in the center of mass frame. My predictions (blue solid line) are obtained with the SMS potential at the chiral order $N^4\text{LO}^+$, with the cut-off parameter $\Lambda = 450\text{ MeV}$ and with 2NC contributions included via the Siegert theorem. The dashed pink curve shows predictions obtained with the same interaction but without 2NC contributions. The dashed-dotted brown curve presents theoretical results from [77]. Experimental data are taken from [73] (filled circles) and [76] (empty circles).



Figure 3.20: The tensor analyzing powers T_{20} (left) and T_{22} (right) as a function of the photon energy E_γ at fixed outgoing proton angle $\theta_p = 88^\circ$ in the center of mass frame. My predictions have been obtained with the SMS potential at the chiral order $N^4\text{LO}^+$, with the different values of the cut-off parameter Λ (from 400 MeV to 550 MeV). The dashed-dotted brown curve presents theoretical results from [77]. Experimental data are taken from [73] (filled circles) and [76] (empty circles).



Figure 3.21: The averaged tensor analyzing powers T_{20} (left), T_{21} (middle) and T_{22} (right) as a function of the photon energy for the outgoing proton momentum polar angle θ_p in range $24^\circ - 48^\circ$ in the center of mass frame. The solid blue curve is a mean value of my predictions at energy values ranges from 25 to 45 MeV, obtained with the SMS potential at $N^4\text{LO}^+$ chiral order and with $\Lambda = 450$ MeV and with 1NC used together with the Siegert approach. The pink dashed curve represents similar predictions but with the nuclear current reduced to the 1NC only. The corresponding bands show predictions at border energies 25 and 45 MeV. The filled circles are experimental data from [73] for the same energy range.

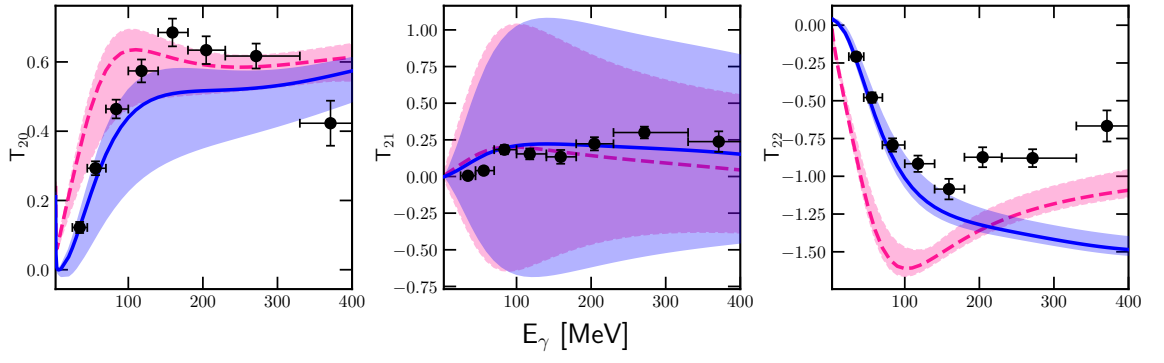


Figure 3.22: The same as in the Fig. 3.21 but for the θ_p in range $70^\circ - 102^\circ$.

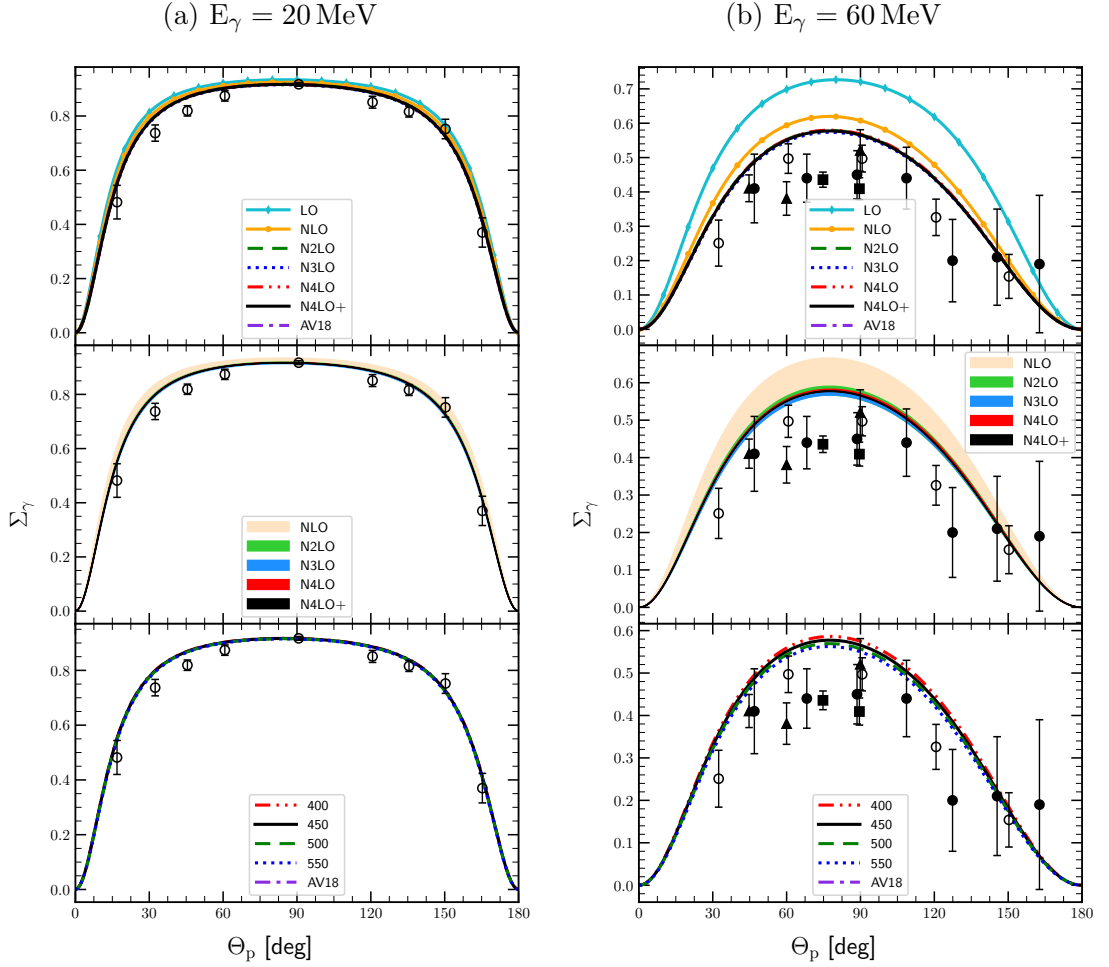


Figure 3.23: The photon asymmetry Σ_γ as a function of the outgoing proton angle in the center of mass frame for the photon energy 20 MeV(a) and 60 MeV(b). The top row presents results obtained using the SMS potential with chiral orders from LO to $N^4\text{LO}^+$ and with the cut-off parameter $\Lambda = 450$ MeV. The middle row shows truncation errors for each chiral order starting from NLO and the bottom row presents a cut-off dependence for the chiral potential $N^4\text{LO}^+$. Filled circles are experimental data from [79], empty circles - from [80], filled squares - from [81] and triangles are from [82]. For the sake of comparison, predictions obtained with the AV18 potential are given by the dashed-dotted curve as well.



Figure 3.24: The photon asymmetry Σ_γ as a function of the outgoing proton angle θ_p in the CM frame at $E_\gamma = 20$ MeV (left) and $E_\gamma = 60$ MeV (right). Similarly to Fig. 3.4b predictions obtained with chiral $N^4\text{LO}^+$ potential and $\Lambda = 450$ MeV are presented for three theoretical models. The blue solid line is the most complete prediction we have (plane-wave plus rescattering parts, 1NC + Siegert), the pink dashed line shows predictions obtained with single-nucleon current only (1NC) - without the Siegert contributions and the green dashed-dotted line is a prediction in which we neglect the rescattering part and stick to the plane-wave part only but keeping the Siegert contributions. Filled circles are experimental data from [79], empty circles - from [80], filled squares - from [81] and triangles are from [82].

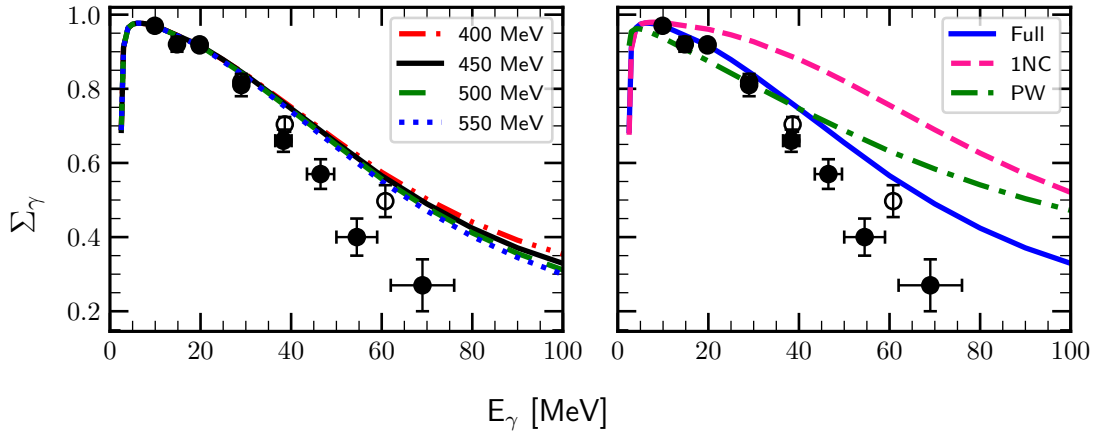


Figure 3.25: The photon asymmetry Σ_γ as a function of the photon energy at the fixed outgoing proton's momentum polar angle $\theta_p = 90^\circ$. On the left panel, each curve corresponds to the particular value of the cut-off parameter and chiral potential used here is the $N^4\text{LO}^+$ one. On the right panel, the blue solid curve represents our most complete predictions comprising the plane-wave plus rescattering parts and 1NC+Siegert current propagator (the same as 450 MeV line in left). The pink dashed curve shows predictions obtained with the single-nucleon current only (without applying the Siegert theorem) and the green dashed-dotted curve represents predictions with the full current (1NC + Siegert) but plane-wave part only. Filled circles are experimental data from [83], empty circles - from [80].



Figure 3.26: Proton polarization $P_y(p)$ as a function of the outgoing proton's momentum polar angle in the center of mass frame with the photon energy 30 MeV (a) and 100 MeV (b). The top figures present results obtained using potential with different chiral orders (from LO to N⁴LO⁺) with cut-off parameter $\Lambda = 450$ MeV. The middle panel shows truncation errors for each chiral order starting from NLO and bottom figures present a cut-off dependence of predictions based on the SMS N⁴LO⁺ potential. For the sake of comparison, predictions obtained with the AV18 potential are shown as well.



Figure 3.27: The same as in Fig. 3.26 but for the neutron polarization $P_y(n)$ and at photon energies 2.75 MeV (a) and 100 MeV (b). Data are from [84] (empty circles) and [85] (filled circles).

3.2 Helium-3 photodisintegration

3.2.1 Three-body breakup

In this section I will discuss results for ${}^3\text{He} \rightarrow p + p + n$ differential cross-section obtained with the 1NC + Siegert model of nuclear current. For three free nucleons in the final state, it is convenient to introduce, as a kinematical variable, the arc-length of the S-curve. For a given direction of two momenta \hat{p}_1 and \hat{p}_2 , the S-curve spans in the plane defined by kinetic energies of the same two nucleons, E_1 and E_2 .

For three particles and known initial energy and momenta five kinematical variables² are required to define the final kinematics. We choose four variables as directions of outgoing nucleons no 1 and 2: $\theta_1, \phi_1, \theta_2$ and ϕ_2 , with the z -axis aligned to the photon momentum. Choosing E_1 as the fifth variable would introduce ambiguity, as in some cases two values of E_2 could be allowed. Instead, the location on the S-curve defines the kinematical configuration unambiguously. The various possible locations of the S-curve in $E_1 - E_2$ plane, as well as the convention on choosing the $S = 0$ point is given in Fig. 1 of [49].

In the Fig. 3.28 I demonstrate a differential cross section $\frac{d^5\sigma}{d\Omega_1 d\Omega_2 dS}$ as a function of the S arc length and as in the previous section, I study the convergence with respect to chiral order and the cut-off dependence. The photon energy is $E_\gamma = 30$ MeV; the kinematic configuration $\theta_1 = 15^\circ, \phi_1 = 0^\circ, \theta_2 = 15^\circ, \phi_2 = 180^\circ$ and predictions have been obtained without 3NF.³ On the left, we see that only NLO and N²LO introduce relatively large truncation errors. The maximal width of a band for NLO is 37.6 % at $S = 10$ MeV, for N²LO it is 12.4 % at the same S-value and it is gradually decreasing coming to 0.13 % at N⁴LO⁺. The cut-off spread(right) is bigger around maxima values but remains below 3 %. It reaches 0.78 % at the minimum point ($S = 10$ MeV).

With larger energy $E_\gamma = 100$ MeV, for which predictions are demonstrated in the Fig. 3.29, both truncation error and cut-off spread become larger. The truncation band at the maximum point at $S = 10$ MeV for NLO is 55.0 % decreasing to 2.2 % at N⁴LO⁺ which still is around 3 times larger than it was for predictions at $E_\gamma = 30$ MeV. The cut-off spread also becomes larger with increasing energy value: 9.0 % at the same (maximum) point which is also ~ 3 times bigger than the one we observed for the lower energy.

Results for the same $E_\gamma = 100$ MeV but other angular configuration $\theta_1 = 75^\circ, \phi_1 = 75^\circ, \theta_2 = 75^\circ, \phi_2 = 105^\circ$ are given in Fig. 3.30. The top row shows results obtained with 2NF only, while predictions obtained with 3NF are shown on the bottom row. It seems that 3NF does not change much the convergence with respect to the chiral order: truncation error band at the point of maximum $S = 35$ MeV (N⁴LO⁺) is 1.11 % and 1.16 % with and without 3NF, respectively. As it is almost the same, I conclude that inclusion N²LO 3NF practically does not affect chiral order convergence. Note, 3NF at N²LO has been used for all forces above NLO.

The cut-off dependence, in turn, is affected by the presence of 3NF. Predictions with 2NF only have 13.7 % spread at the same maximum point $S = 35$ MeV, while predictions with 3NF have only 1.23 % relative spread, so the difference is tremendous.

Similar trends are present also in other configurations, demonstrated for the comparison: Figs.3.31, Figs.3.32 and Figs.3.33.

²Among nine variables describing final state \vec{p}_1, \vec{p}_2 and \vec{p}_3 , four can be derived from energy and momentum conservation laws.

³Different kinematic configurations $\theta_1, \phi_1, \theta_2$ and ϕ_2 have been tested with a step of 15° and most interesting cases(showing the largest discrepancies) are presented in this work.

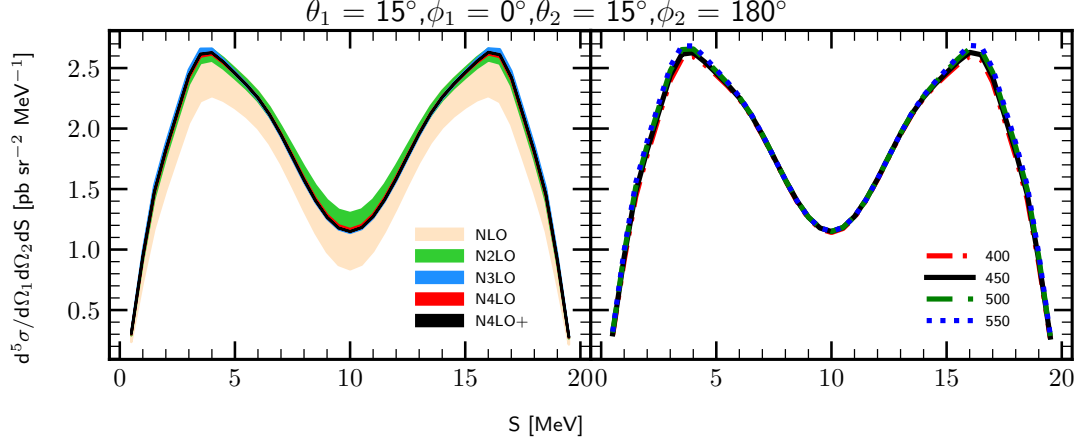


Figure 3.28: The five-fold differential cross section for the photon energy $E_\gamma = 30$ MeV for the kinematic configuration $\theta_1 = 15^\circ$, $\phi_1 = 0^\circ$, $\theta_2 = 15^\circ$, $\phi_2 = 180^\circ$. The left figure presents truncation error bands obtained using the SMS potential with chiral orders from NLO to $N^4\text{LO}^+$, and with cut-off parameter $\Lambda = 450$ MeV. The right figure presents a cut-off dependence at $N^4\text{LO}^+$. Results are obtained with two-nucleon force only and 1NC current and Siegert theorem used for 2NC contributions.

The exclusive cross-sections shown above, in Figs. 3.28-3.33 are small and unfortunately below the possibilities of current experimental techniques. The semi-inclusive measurement is more likely to be performed, thus in Figs 3.34 and 3.35 I show the differential cross section $\frac{d^3\sigma}{d\Omega_p dE_p}$. I choose the same photon energies as above: $E_\gamma = 30$ MeV and $E_\gamma = 100$ MeV. Each figure consists of subfigures where each row presents results for a proton momenta polar angle $\theta_p = 10^\circ, 50^\circ, 90^\circ, 130^\circ$ and 170° . The left part of each subfigure shows detected chiral order dependence while the right - the cut-off dependence.

At the photon energy 30 MeV the chiral dependence is relatively weak: at the maximum point ($E_p \simeq 3.8$ MeV) the relative difference varies between 12 % and 28 % at LO for different angles. This difference decreases with each subsequent order resulting in maximum 0.15 % at $N^4\text{LO}^+$. At the energy $E_\gamma = 100$ MeV truncation errors are larger: at the maximum around $E_p \simeq 1.46$ MeV the discrepancy is around 40 % (NLO), 15 % (N2LO), coming to 1.5 % at $N^4\text{LO}^+$.

A typical cut-off uncertainty at $E_\gamma = 30$ MeV is around 2 % and at $E_\gamma = 100$ MeV increases up to 8 % for all angles and at the same values of E_p as regarded above.

Observed small uncertainties allow me to conclude that the semi-inclusive cross-section $\frac{d^3\sigma}{d\Omega_p dE_p}$ is not useful in studies aiming on pin-down the details of the chiral force.



Figure 3.29: The same as in Fig. 3.28 but for the photon energy $E_\gamma = 100$ MeV



Figure 3.30: The same as in the Fig. 3.29 but for the kinematic configuration at $\theta_1 = 75^\circ$, $\phi_1 = 75^\circ$, $\theta_2 = 75^\circ$ and $\phi_2 = 105^\circ$. Results obtained with the chiral SMS 2N force are presented on the top row. The same, but with the N²LO 3NF included is presented on the bottom row (starting from the N²LO - where 3NF appears for the first time).

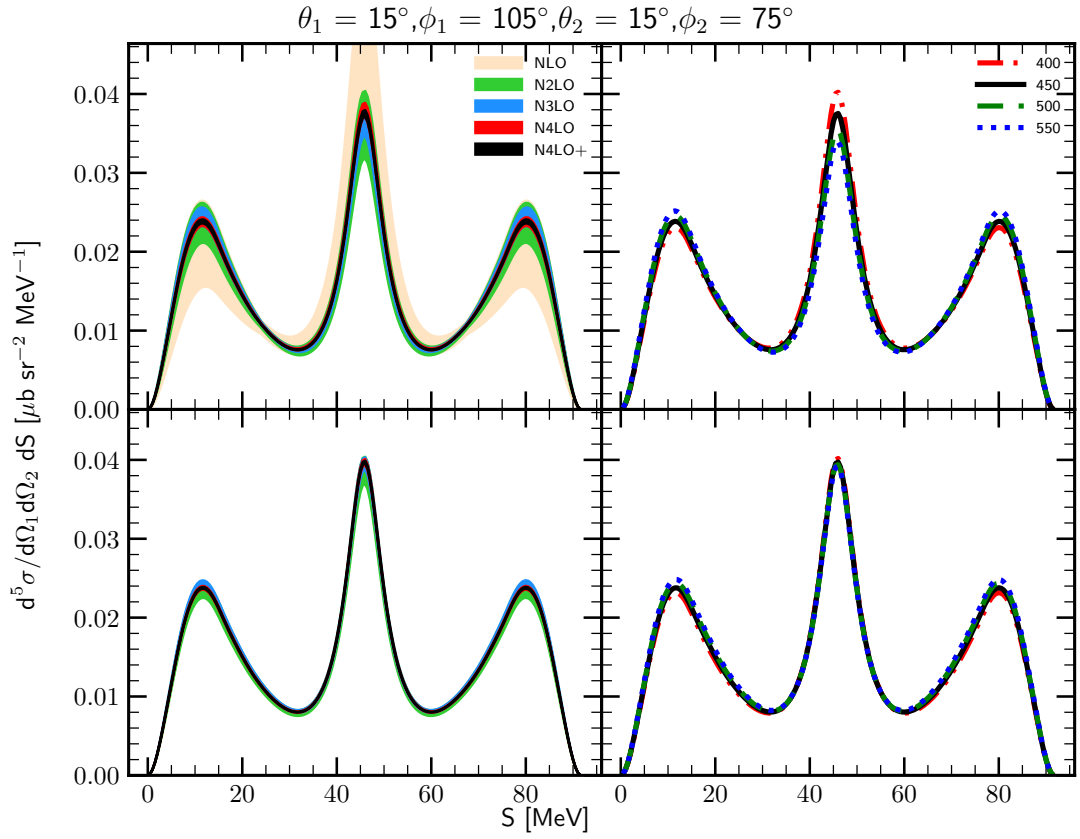


Figure 3.31: The same as in the Fig. 3.30 but for the kinematic configuration at $\theta_1 = 15^\circ$, $\phi_1 = 105^\circ$, $\theta_2 = 15^\circ$ and $\phi_2 = 75^\circ$.

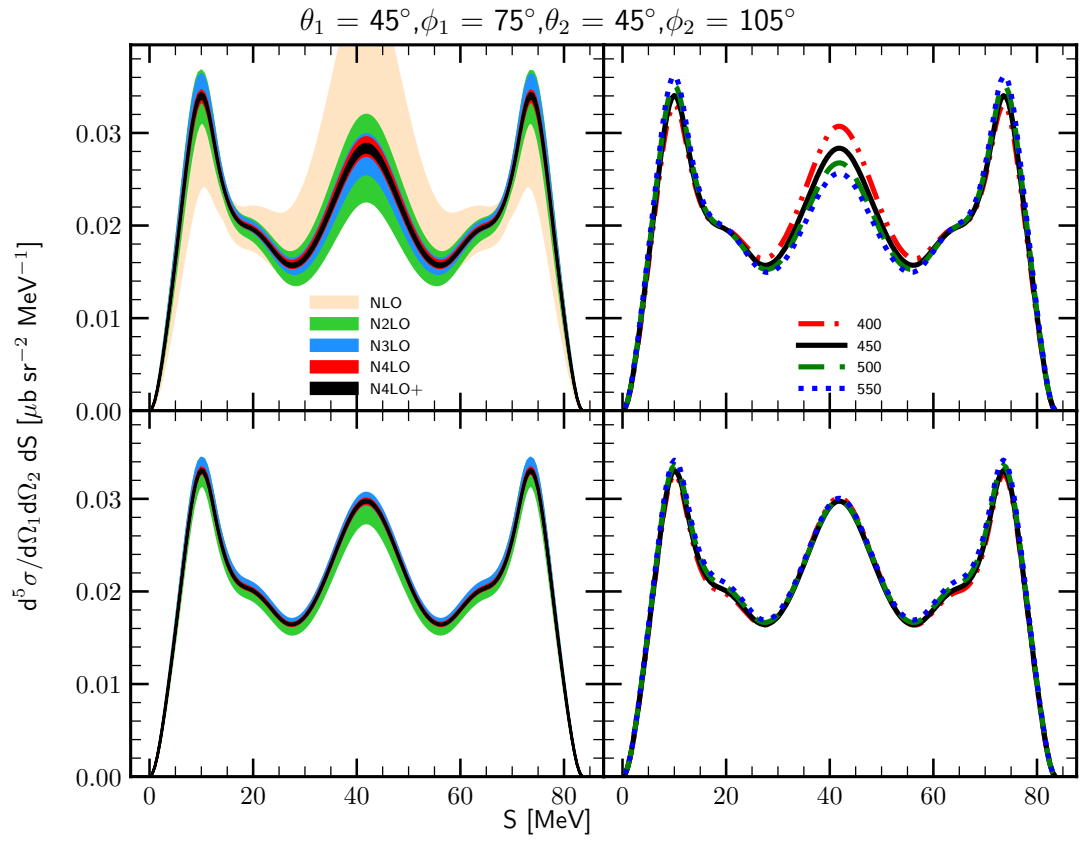


Figure 3.32: The same as in the Fig. 3.31 but for the different kinematic configuration.

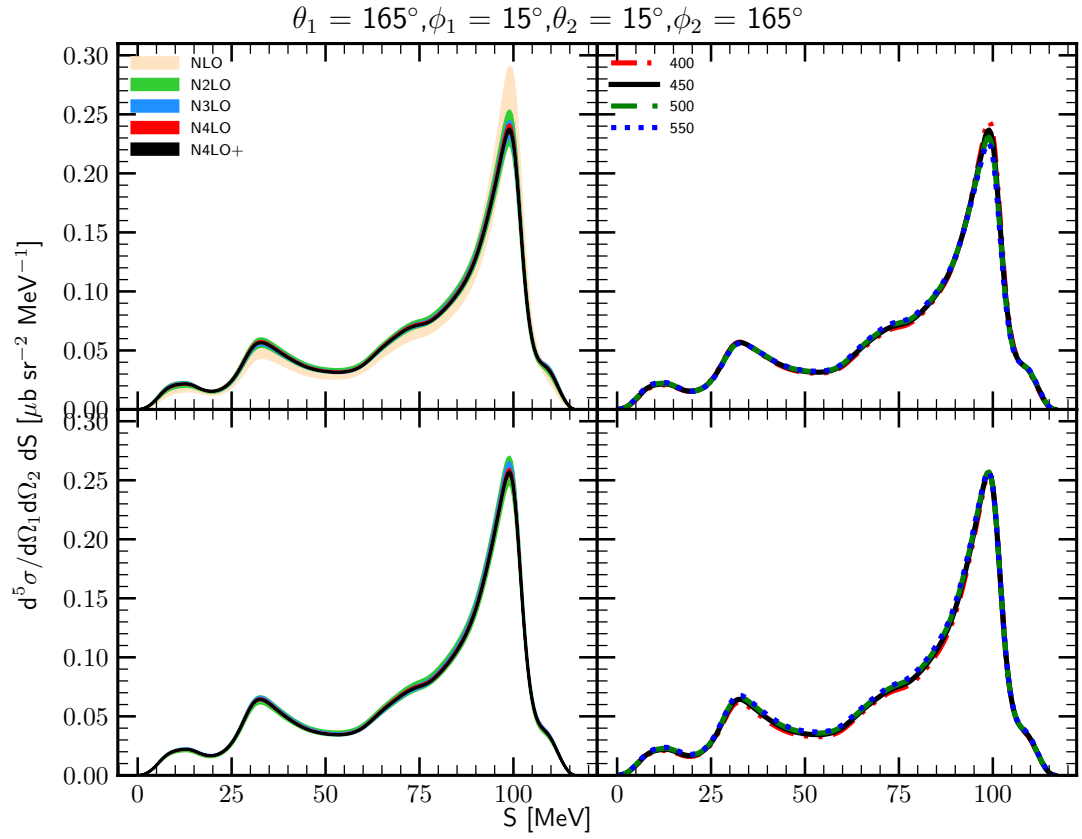


Figure 3.33: The same as in the Fig. 3.32 but for the kinematic configuration at $\theta_1 = 165^\circ$, $\phi_1 = 15^\circ$, $\theta_2 = 15^\circ$ and $\phi_2 = 165^\circ$.

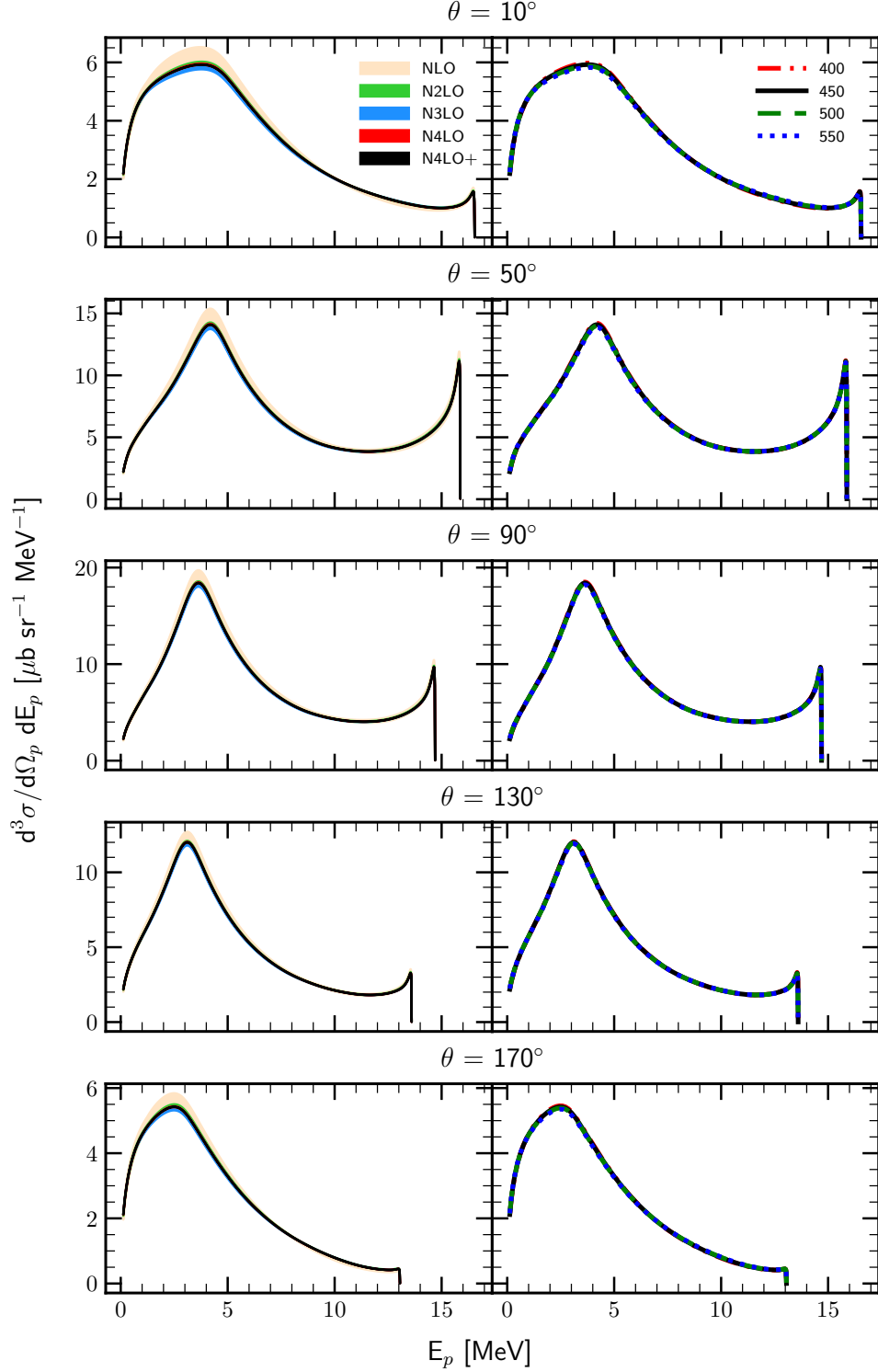


Figure 3.34: The semi-inclusive differential cross section $\frac{d^3\sigma}{d\Omega_p dE_p}$ at $E_\gamma = 30$ MeV $\phi_1 = 0^\circ$ as a function of outgoing proton energy E_p . Each row represents predictions for different values of the outgoing proton's momentum polar angle θ_p : 10° , 50° , 90° , 130° and 170° . The left figure presents truncation error bands obtained using the SMS potential with chiral orders from NLO to $N^4\text{LO}^+$, and with cut-off parameter $\Lambda = 450$ MeV. The right figure presents a cut-off dependence at $N^4\text{LO}^+$. Predictions have been obtained with the SMS NN potential but neglecting 3NF.


 Figure 3.35: The same as in Fig. 3.34 but for $E_\gamma = 100$ MeV.

3.2.2 Two-body breakup

The differential cross section $d\sigma/d\Omega_d$ for the ${}^3\text{He}+\gamma \rightarrow d+p$ reaction is presented in the Fig. 3.36 (for the photon energy $E_\gamma = 30$ MeV) and in the Fig. 3.37 (for $E_\gamma = 100$ MeV). We see a significant enlargement of both truncation and cut-off uncertainties with increasing photon energy. The relative spread of the truncation error at the maximum point ($\theta_p = 105^\circ$) for the lower energy is 0.05 % at N^4LO^+ , while for the larger energy similar spread is 0.45 % (at N^4LO^+ , $\theta_p = 120^\circ$).

The cut-off dependence is also stronger for the larger energy: it is 1.45 % at 30 MeV and 4.01 % at 100 MeV (at the points of maximum).

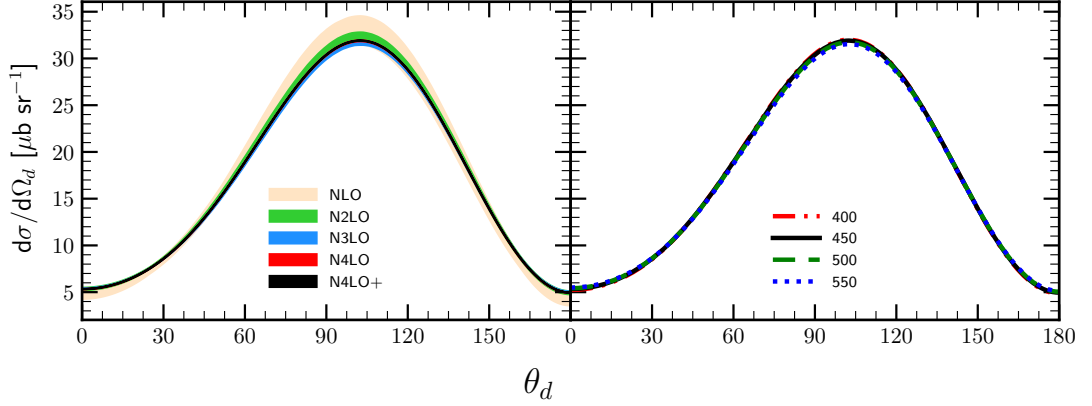


Figure 3.36: Differential cross section for the two-body photodisintegration of ${}^3\text{He}$ as a function of the $d - \gamma$ angle in CM. The initial photon energy $E_\gamma = 30$ MeV and NN with 2NF was used.

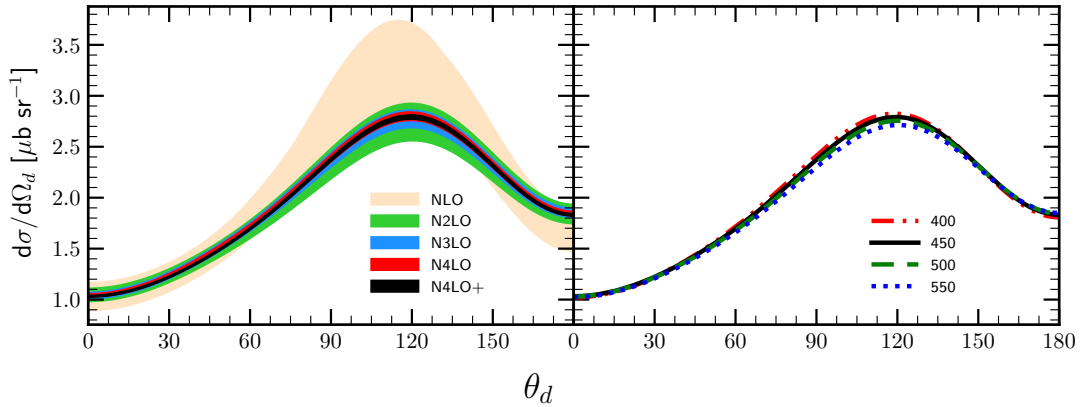


Figure 3.37: The same as in the Fig. 3.36 but for the photon energy $E_\gamma = 100$ MeV

3.3 Triton 3N photodisintegration

In this section, I will discuss results for ${}^3\text{H} \rightarrow n + n + p$ process in the case when two neutrons are detected and similarly to the previous chapter, I present the convergence of predictions and their cut-off dependence.

In the Fig. 3.38 I present a differential cross section $\frac{d^5\sigma}{d\Omega_1 d\Omega_2 dS}$ as a function of the S arc length. The photon energy is $E_\gamma = 30$ MeV and the kinematic configuration $\theta_1 = 15^\circ$, $\phi_1 = 0^\circ$, $\theta_2 = 15^\circ$, $\phi_2 = 180^\circ$; predictions have been obtained without 3NF. We see that only NLO and N²LO introduce relatively large truncation errors. The maximal width of a band for NLO is 30.95 % at $S = 10$ MeV, for N²LO it is 6.79 % at the same point and it is gradually decreasing coming to 0.10 % at N⁴LO⁺. The cut-off spread around maxima values is 6.25 % (at $S = 4$ MeV) and it is 1.81 % at $S = 10$ MeV.

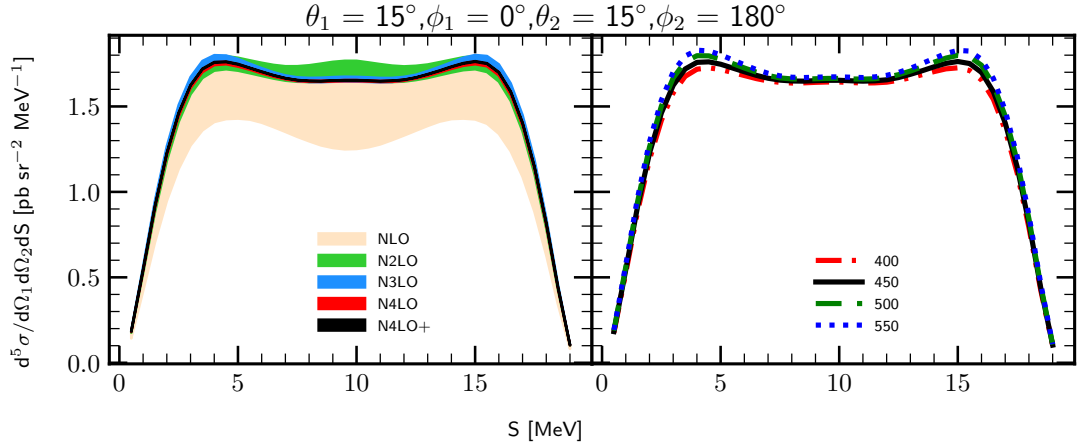


Figure 3.38: The five-fold differential cross section for the photon energy $E_\gamma = 30$ MeV for the kinematic configuration $\theta_1 = 15^\circ$, $\phi_1 = 0^\circ$, $\theta_2 = 15^\circ$, $\phi_2 = 180^\circ$ with detected particles proton (number 1) and neutron (number 2). The left figure presents truncation error bands obtained using potential with chiral orders from NLO to N⁴LO⁺, and with cut-off parameter $\Lambda = 450$ MeV. The right figure presents a cut-off dependence at N⁴LO⁺. Results are obtained with two-nucleon force only and 1NC current plus Siegert.

At bigger energy $E_\gamma = 100$ MeV demonstrated in the Fig. 3.39, the truncation band at the maximum point $S = 10$ MeV for NLO is 50.26 % decreases to 2.00 % at N⁴LO⁺. The cut-off spread also becomes larger with increasing energy value: 9.52 % at the same maximum.

The truncation error bands and cut-off dependence are very similar to what was found for the three-body Helium-3 photodisintegration and the relative errors have similar magnitudes.

Results for other angular configurations with $E_\gamma = 30$ MeV and at $\theta_1 = 75^\circ$, $\phi_1 = 75^\circ$, $\theta_2 = 75^\circ$, $\phi_2 = 105^\circ$ are demonstrated in Fig. 3.40. Both truncation errors and cut-off dependence are smaller with such configuration: the relative width of the truncation band at NLO is 9.39 % (at the maximum point $S = 8$ MeV) and drops to only 0.1 % at N⁴LO⁺. The relative cut-off spread is 0.93 % at the same point.

At the bigger energy $E_\gamma = 100$ MeV demonstrated in Fig. 3.41 uncertainties grow. The truncation bands are 44.42 % and 2.09 % (at NLO and N⁴LO⁺ respectively) and the cut-off spread is 13.04 % (all at $S = 35$ MeV in maximum).



Figure 3.39: The same as in the Fig. 3.38 but for the photon energy $E_\gamma = 100$ MeV.

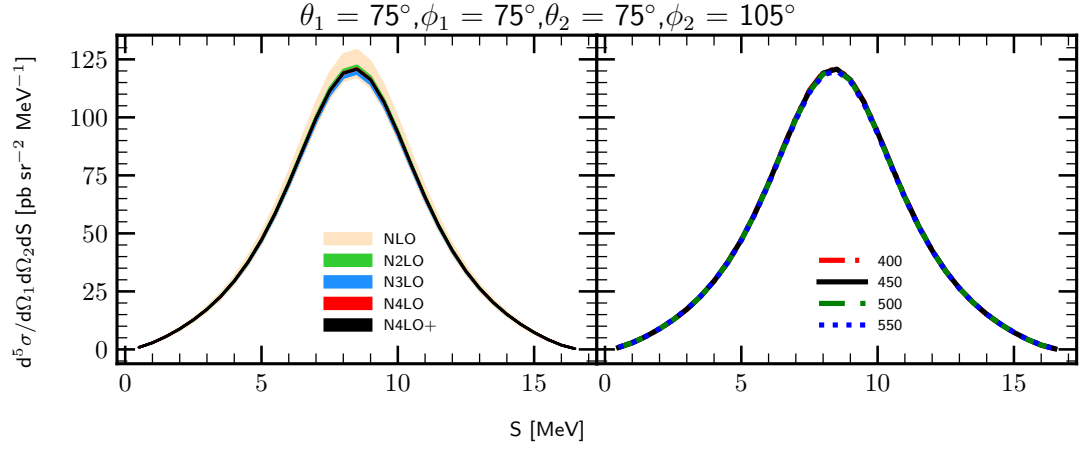
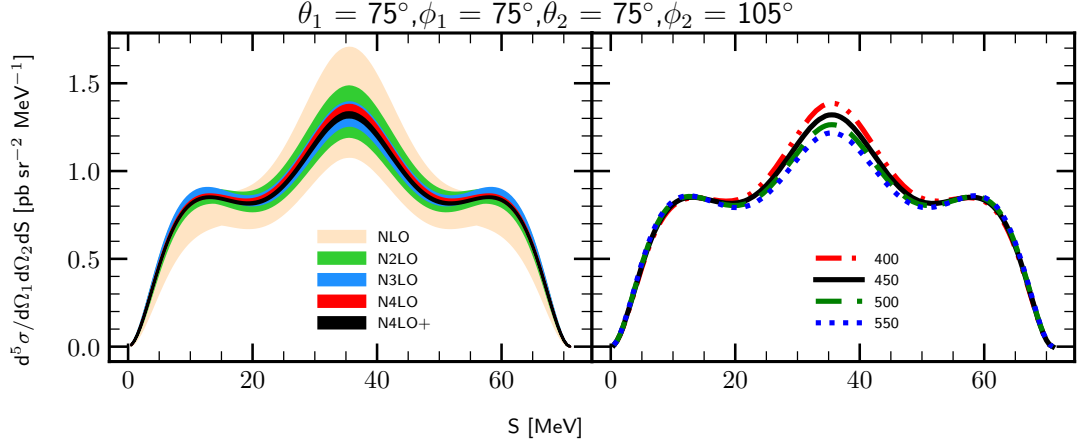
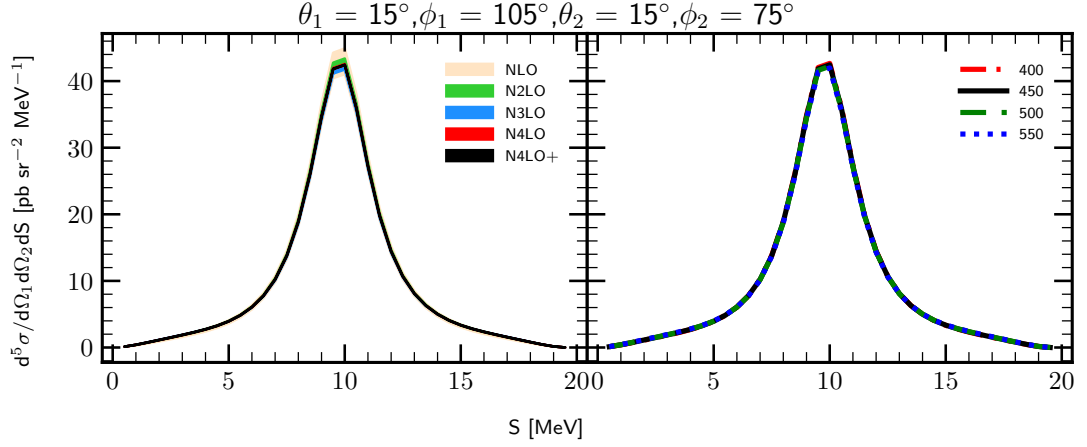
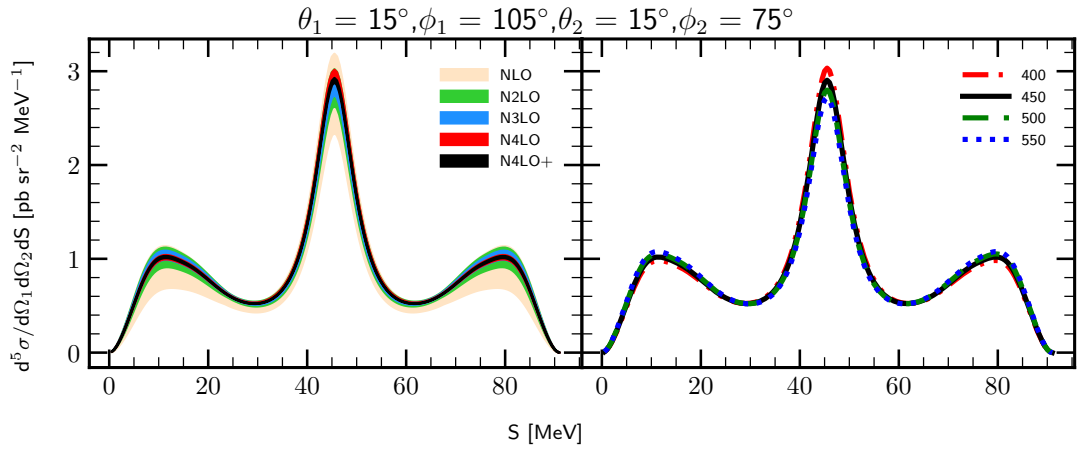


Figure 3.40: The same as in the Fig. 3.38 but for the kinematic configuration with $\theta_1 = 75^\circ$, $\phi_1 = 75^\circ$, $\theta_2 = 75^\circ$, $\phi_2 = 105^\circ$.

Similar trends are present also in other examples, demonstrated for the comparison in Figs. 3.42-3.47.


 Figure 3.41: The same as in the Fig. 3.40 but for the photon energy $E_\gamma = 100$ MeV.

 Figure 3.42: The same as in the Fig. 3.40 but for the kinematic configuration with $\theta_1 = 15^\circ$, $\phi_1 = 105^\circ$, $\theta_2 = 15^\circ$, $\phi_2 = 75^\circ$.

 Figure 3.43: The same as in the Fig. 3.42 but for the photon energy $E_\gamma = 100$ MeV.

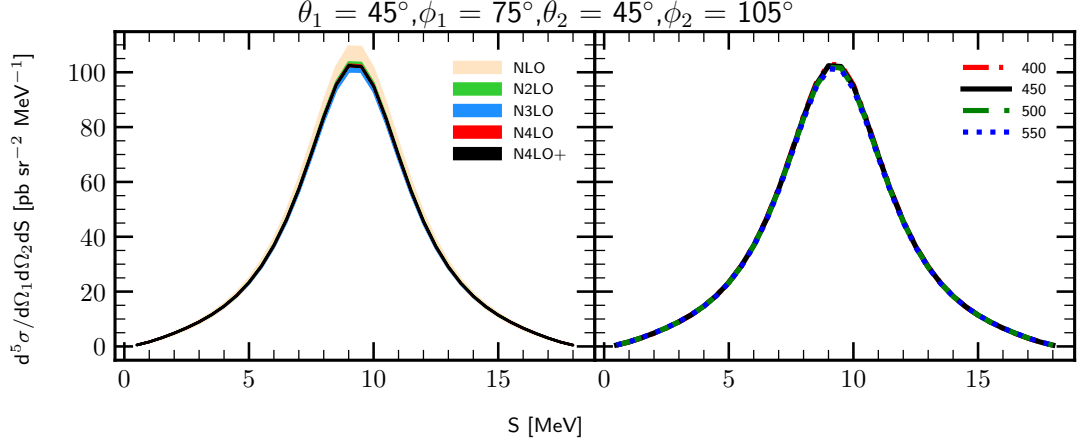


Figure 3.44: The same as in the Fig. 3.42 but for the kinematic configuration with $\theta_1 = 45^\circ$, $\phi_1 = 75^\circ$, $\theta_2 = 45^\circ$, $\phi_2 = 105^\circ$.

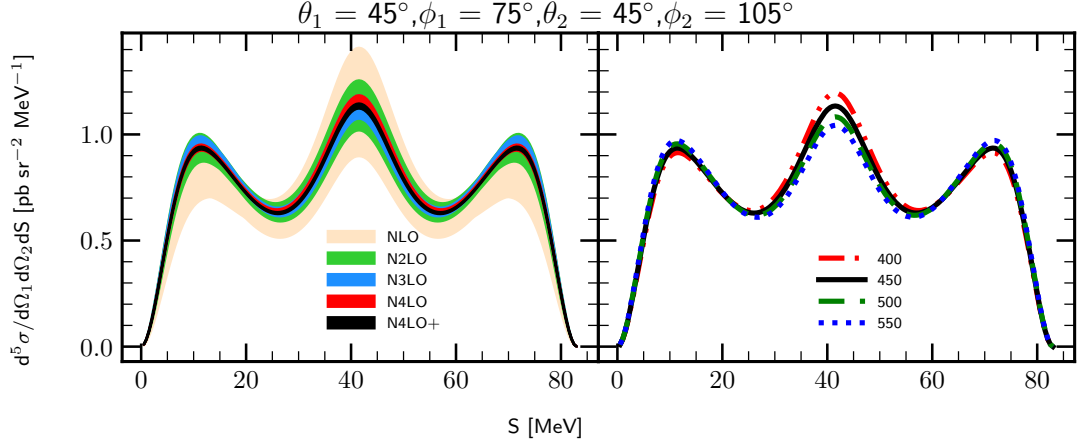


Figure 3.45: The same as in the Fig. 3.44 but for the photon energy $E_\gamma = 100$ MeV.

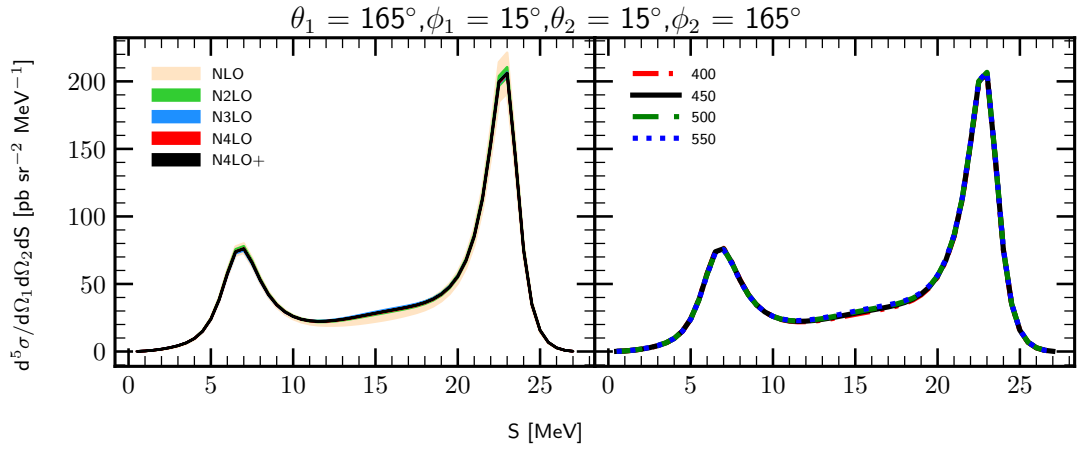


Figure 3.46: The same as in the Fig. 3.44 but for the kinematic configuration with $\theta_1 = 165^\circ$, $\phi_1 = 15^\circ$, $\theta_2 = 15^\circ$, $\phi_2 = 165^\circ$.

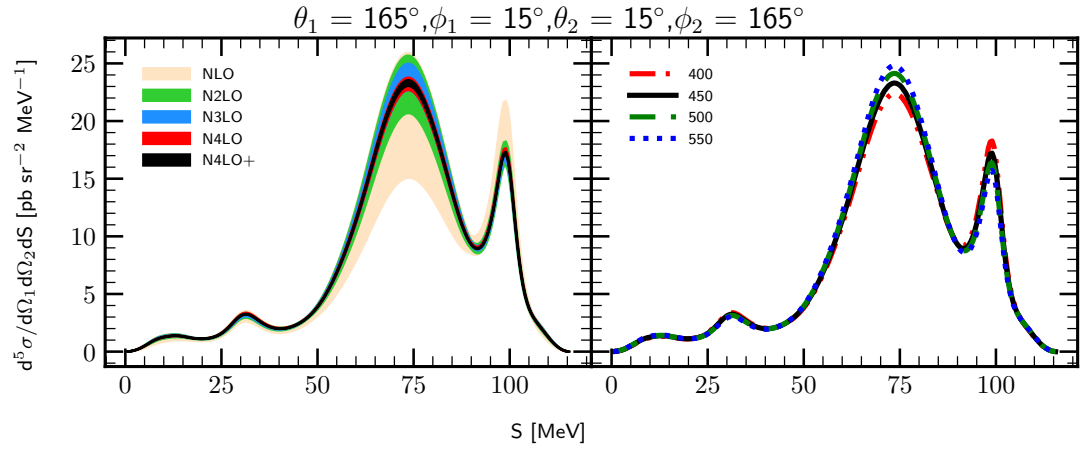


Figure 3.47: The same as in the Fig. 3.46 but for the photon energy $E_\gamma = 100$ MeV.

3.4 Pion absorption from the lowest atomic orbital

3.4.1 Pion absorption in ^2H

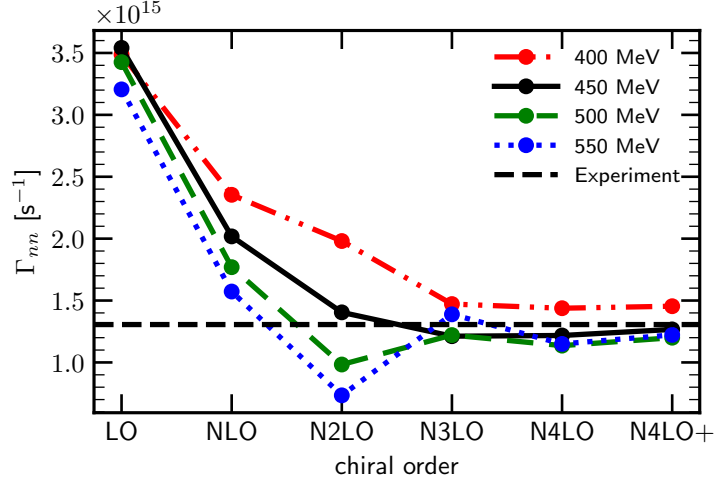


Figure 3.48: Absorption rate for the $\pi^- + ^2\text{H} \rightarrow n + n$ reaction. The rates were calculated using the SMS force with different chiral orders and cut-off values. The results were obtained using the single-nucleon transition operator and supplemented by two-nucleon contributions at the leading order. The figure shows the results obtained using the plane wave (PW) plus two-neutron rescattering (Full) parts. The experimental value is extracted from the hadronic ground-state broadening in pionic deuterium and is taken from Refs. [86, 87].

In Fig. 3.48 the absorption rate Γ_{nn} is shown for the process $\pi^- + ^2\text{H} \rightarrow n + n$ as a function of the chiral order (horizontal axis) and the cutoff parameter (different lines) together with experimental data extracted from [86, 87]. We see a significant difference between predictions obtained using different Λ . The impact of chiral orders is large at LO and NLO (each subsequent order differs from the previous by $\sim 40\%$ and $\sim 30\%$, respectively) and is gradually decreasing, and N^3LO - N^4LO - N^4LO^+ steps are almost invisible (the relative difference between subsequent orders is $\sim 5\%$). The comparison with experimental data shows that our predictions converge to a correct value coming closely to it all large chiral orders and Λ s except $\Lambda = 450$ MeV which is clearly separated from other predictions. The bias $\Gamma_{nn}^{550} - \Gamma_{nn}^{exp}$ is still $0.178 \times 10^{15} \text{ s}^{-1}$ which is 12.7% . Such a result reveals that NN interaction with $\Lambda = 450$ MeV is inadequate in data description. However, using it gives an additional measure of uncertainty related to the cut-off parameter value.

3.4.2 Pion absorption in ^3He

In Fig. 3.49 and 3.50 the total pion absorption rates are presented as a function of the chiral order and for different values of the cut-off parameter for $\pi^- + ^3\text{He} \rightarrow p + n + n$ and $\pi^- + ^3\text{He} \rightarrow n + d$ reactions, respectively. Both figures show that with fixed chiral order the arrangement of absorption rates obtained with various values of the cut-off parameter remains the same, namely with increasing Λ , the absorption rate decreases. The only exception in both cases appears at N^3LO where prediction with $\Lambda = 550$ MeV goes above

other predictions. At the next order, N⁴LO, it comes back to the usual arrangement. This behavior may be connected to the ³He wave function resulting from the 3NF used for the calculation. In order to prove that, I show in Fig. 3.51 a corresponding figure for a ³He proton radius r_p calculated with and without 3NF (left and right panels, respectively). Results obtained with the 3NF show also a deviation at N³LO where $\Lambda = 550$ MeV and $\Lambda = 500$ MeV are very close to each other while for the radius computed without the 3NF a clear separation is present. Nevertheless, the spread of predictions concerning the cut-off values seen in Fig. 3.51 is much smaller with the 3NF and deviation seems to be not crucial as the total difference between predictions in this case is very small.

There are also experimental data for the Γ_{pnn} and Γ_{nd} available on the market. As it was discussed in [88], experimental data for the Γ_{pnn} and Γ_{nd} can be extracted from [89–91] and it is

$$\Gamma_{pnn}^{\text{exp.}} = (2.47 \pm 0.65) \times 10^{16} \text{ s}^{-1} \quad (3.3)$$

$$\Gamma_{nd}^{\text{exp.}} = (6.8 \pm 1.9) \times 10^{15} \text{ s}^{-1}. \quad (3.4)$$

My predictions can be summarized as follows:

$$\Gamma_{pnn} = (1.28_{-0.14}^{+0.29} \pm 1.02) \times 10^{16} \text{ s}^{-1} \quad (3.5)$$

$$\Gamma_{nd} = (2.0_{-0.6}^{+1.0} \pm 1.6) \times 10^{15} \text{ s}^{-1} \quad (3.6)$$

$$(3.7)$$

where the first error is related to the cut-off parameter and the second one to the chiral order (truncation error).

We see that our predictions, presented in Figs. 3.49 and 3.50, are smaller than experimental values, but they overlap each other within the uncertainty range, giving large experimental errors as well as theoretical ones.

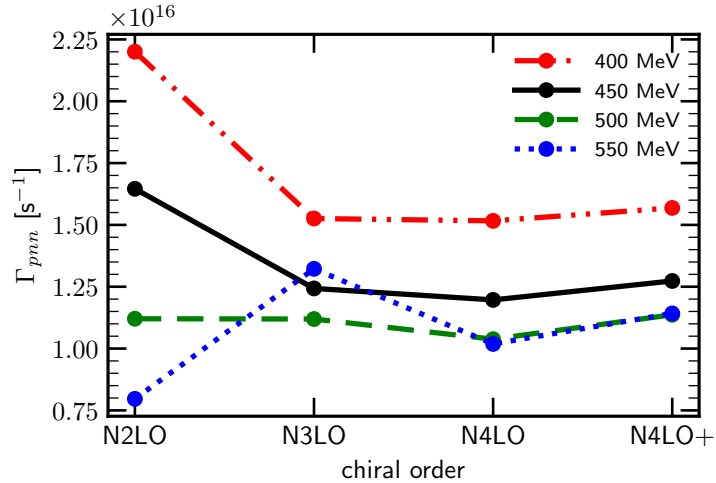
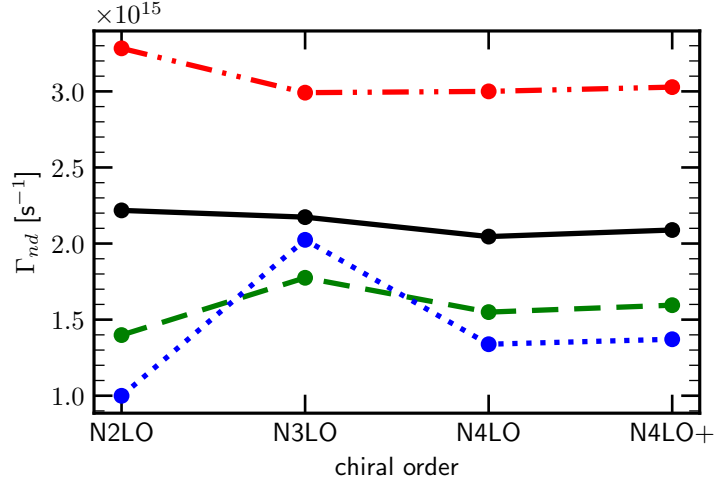
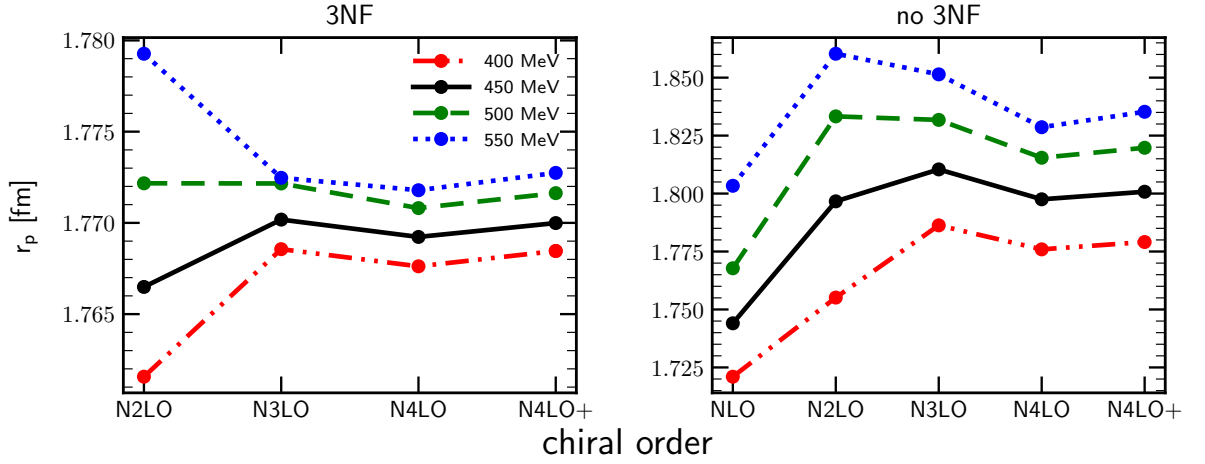


Figure 3.49: Absorption rate for $\pi^- + {}^3\text{He} \rightarrow p + n + n$ reaction as a function of the chiral order and with different values of the cut-off parameter Λ . Predictions were obtained with the SMS NN interaction at a given order combined with N²LO 3NF.


 Figure 3.50: The same as in Fig. 3.49, but for $\pi^- + {}^3\text{He} \rightarrow n + d$ reaction.

 Figure 3.51: Proton radius r_p for ${}^3\text{He}$ nuclei as a function of the chiral order calculated with different values of the cut-off parameter Λ . The radius was calculated with 2NF and 3NF (left panel) or with 2NF only (right panel).

By its nature, the total absorption rates cannot deliver details on the distribution of contributions arising from various dynamical ingredients to the absorption process in the phase space. Thus in the following, I show various intensity plots revealing phase-space regions of special interest.

Let me remind that in the case of absorption rates, only two kinetical variables are necessary to define the exclusive kinematical configuration. That is, because for that process there is full rotational symmetry, as none of the vectors define the (z) -axis.

In Figs. 3.52 and 3.53 I show such intensity plots for the double differential absorption rates $d^2\Gamma_{pnn}/dE_1dE_2$ for the $\pi^- + {}^3\text{He} \rightarrow p + n + n$ process as functions of the nucleons energies (assuming nucleon number 1 to be a proton) and of the Dalitz coordinates (x and y), respectively.

The coordinates x and y are defined as:

Table 3.1: Absorption rates in the four regions of the phase space I_i defined in Ref. [60] for the $\pi^- + {}^3\text{He} \rightarrow p + n + n$ reaction calculated with the chiral SMS NN potential supplemented by 3NF at N²LO with different values of the cutoff parameter Λ .

Λ (MeV)	Normalized absorption rates Γ_i			
	I_1	I_2	I_3	I_4
400	0.804	0.152	0.029	0.016
450	0.797	0.152	0.032	0.019
500	0.792	0.152	0.035	0.021
550	0.793	0.151	0.036	0.020
Gotta <i>et al.</i> [60]	0.844	0.099	0.033	0.023

$$\begin{aligned} x &= 3(E_1 + 2E_2 - E)/E, \\ y &= (3E_1 - E)/E, \end{aligned} \tag{3.8}$$

where E is a total kinetic 3N energy. These coordinates are restricted to the region where $r^2 \equiv x^2 + y^2 \leq 1$.

Each of the two figures consists of four panels representing predictions obtained with different values of the cut-off parameter Λ . The difference between predictions which can be immediately noticed with the naked eye is that the area of the central region (corresponding to the smallest rates) becomes larger with increasing Λ . It coheres to what we saw in Fig. 3.49 where the total absorption rate was inversely correlated with the cut-off parameter. The dominant contribution comes from the region with the lowest proton energy values of $E_1 \rightarrow 0$ where both neutron energies have similar large values. This is a situation of quasi-free scattering(QFS) - when a proton is a spectator and both neutrons share equally all energy.

Another region with a high absorption rate is the neutron-neutron final state interaction configuration (FSI(nn)). It is located at high E_1 values when a proton gets two-thirds part of the total energy while neutrons both get one-sixth of it. It means that proton's kinetic energy is four times larger than neutron's. In Fig. 3.52 we see this region at the very right region (with $E_1 \rightarrow 85$) with rapid growth of the absorption rate and it is observed at every value of the cut-off parameter. The very same region is presented in Fig. 3.53 at $y \rightarrow 1$.

In [88] we have shown the comparison of our predictions with one more experimental data, from [60]. In that paper, the authors consider four specific regions (I_i for $i = 1, 2, 3, 4$) and give experimental results for each of them separately. The renormalization procedure was applied to our predictions in order to compare results with experimental data. Following [60], we divide the predictions for each particular region (Γ_i) by the total value $\sum_{i=1}^4 \Gamma_i$. Results are presented in the Table 3.1.

We see that our predictions are very close to experimental results and retrieve the same pattern of the absorption rate distribution over the regarded regions.

Next in Figs. 3.54 and 3.55 I show similar intensity plots for the predictions obtained with plane wave component only (without rescattering part). They reveal that the difference of predictions obtained without rescattering part with ones including it (Figs. 3.52 and 3.53) is very large. Predicted values are a few times larger and the distribution of dominant areas is completely different. The FSI(nn) region is not presented here in the

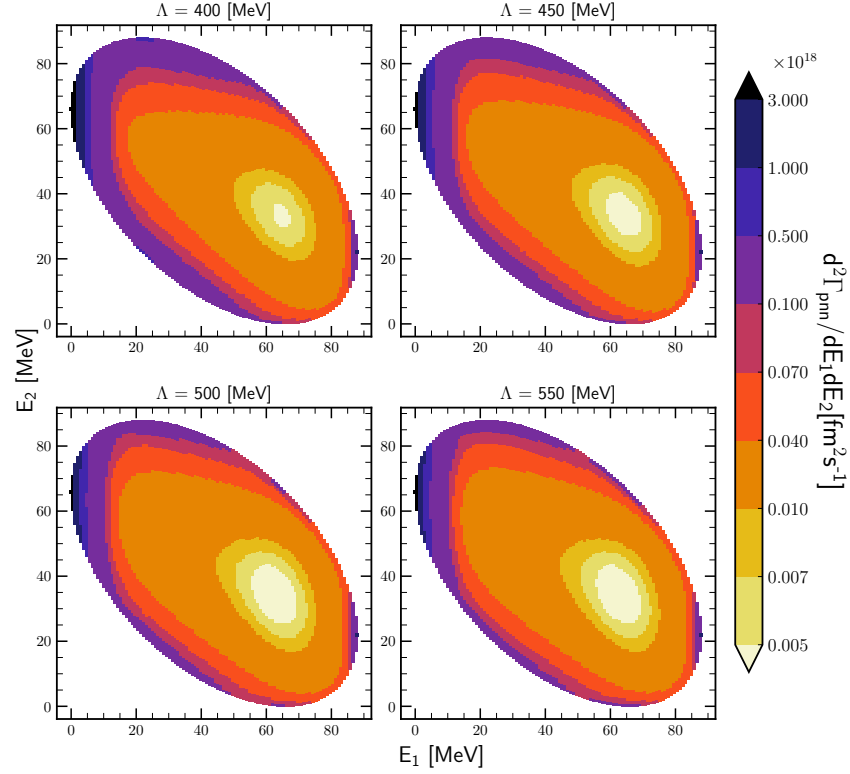


Figure 3.52: Intensity plots for the double differential absorption rates $d^2\Gamma_{pn}/dE_1 dE_2$ for the $\pi^- + {}^3\text{He} \rightarrow p + n + n$ process, obtained using the SMS NN potential with all contributions possible: plane wave + rescattering, 1NC+2NC, 2NF+3NF. Each panel presents predictions obtained with different values of the cut-off parameter Λ : from $\Lambda = 400$ MeV (upper left) to $\Lambda = 550$ MeV (lower right). Nucleon 1 is a proton.

sense that there is no peak concerning other regions. That is natural, as the FSI(nn) peak arises from strong interaction in the final state, which by definition is not in the plane wave approximation. On the contrary, the QFS region is presented. Results of Figs. 3.54 and 3.55 tell us that one has to take into account the rescattering part in order to obtain realistic predictions for that process.

Results have been obtained with plane wave plus rescattering parts but with the single nucleon current only are presented in Figs. 3.56 and 3.57. As previously, each panel in the figures presents predictions obtained with different values of the cut-off parameter Λ . In contrast to the combinations shown above, the change in the cut-off value has a larger impact here: we observe that there is a different pattern in each panel. It does not change dramatically, but two peaks inside the figure become more or less clear. On the other hand, the distribution of the absorption rate is very different from the one, obtained with a more complete components setup (Figs. 3.52 and 3.53).

Figs. 3.58 and 3.59 show prediction obtained using similar dynamical components as in Figs. 3.52 and 3.53, but each panel includes predictions obtained with different chiral orders of the SMS potential. We see that predictions are not sensitive to the chiral order and even N^2LO predictions are pretty much similar to ones obtained with the most advanced N^4LO potential.

Presented above intensity plots correspond to exclusive processes with two particles detected. Now we would like to test if the same behavior of the capture rate is observed for

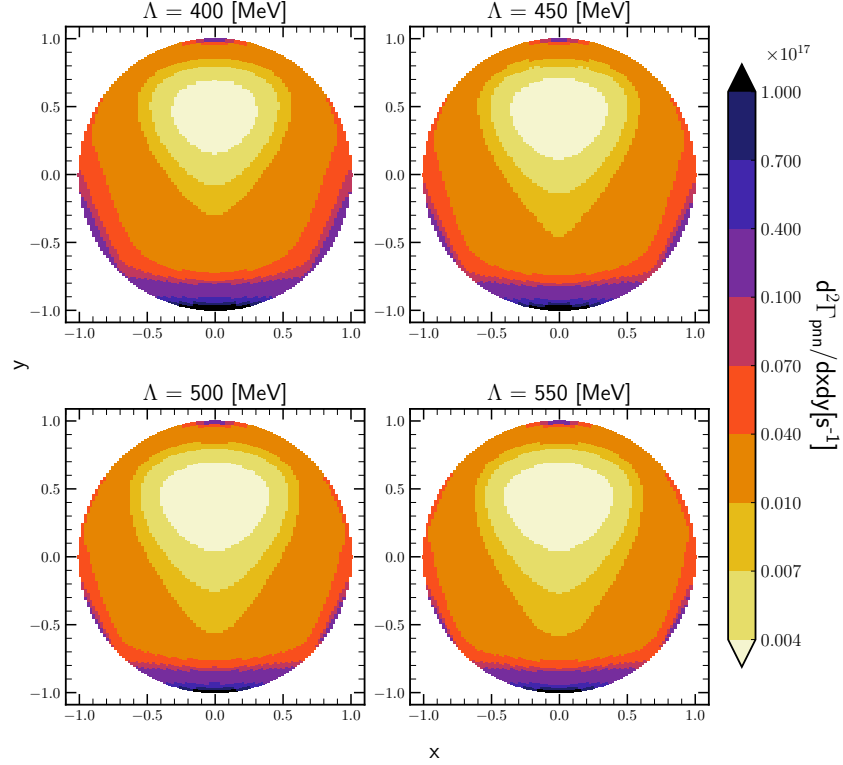


Figure 3.53: The same as in Fig. 3.52 but for the double differential absorption rates $d^2\Gamma_{pnn}/dx dy$.

the semi-inclusive observables. Thus following figures demonstrate the same phenomena but from a different point of view. Namely in Fig. 3.60 I show differential absorption rate $d\Gamma_{pnn}/dE_p$ that is the same as in e.g. Fig. 3.58, but integrated over E_n . All the results are obtained with the most advanced setup (plane wave + rescattering, 1NC+2NC, 2NF+3NF). The left panel consists of the results with $\Lambda = 450$ MeV and each curve corresponds to a particular chiral order. An interesting region here is a maximum of $d\Gamma_{pnn}/dE_p$ which corresponds to the bottom part of the circles from Fig. 3.58. At the point of maximum N²LO prediction distinguishes from other results as its point of maximum is noticeably higher. At $E_p = 0.92$ MeV (maximum point) the value of N²LO is 1.37 times larger than one from N⁴LO⁺ (3.44×10^{17} fm s⁻¹ vs 2.52×10^{17} fm s⁻¹) - the relative difference is 31.1 %. At the same time, the relative difference between all the predictions except for N²LO is 8.3 %.

The right panel of the Fig. 3.60 shows a cut-off dependence of the predictions obtained with the SMS NN chiral potential at N⁴LO⁺ supplemented by N²LO 3NF. In this case, the maximum point is interesting as well. We see that predictions with $\Lambda = 500$ MeV and 550 MeV are quite close to each other: the relative difference between them at $E_p = 0.92$ MeV is only 1.5 %. In turn the spread between $\Lambda = 400$ MeV, 450 MeV and 500 MeV is 40 % (at the same E_p). This cut-off dependence is hidden when looking at the colormaps Fig. 3.52, but from this perspective it is clearly presented. Anyway, the highest Λ , the biggest $d\Gamma_{pnn}/dE_p$ is seen. That observable could be an intensity test for the cut-off value, however, it requires measurement at low proton energy ($\sim 0.8 - 1.0$ MeV) which is an experimental challenge.

Similarly in Fig. 3.61 $d\Gamma_{pnn}/dE_n$ is presented. We observe similar trends as above

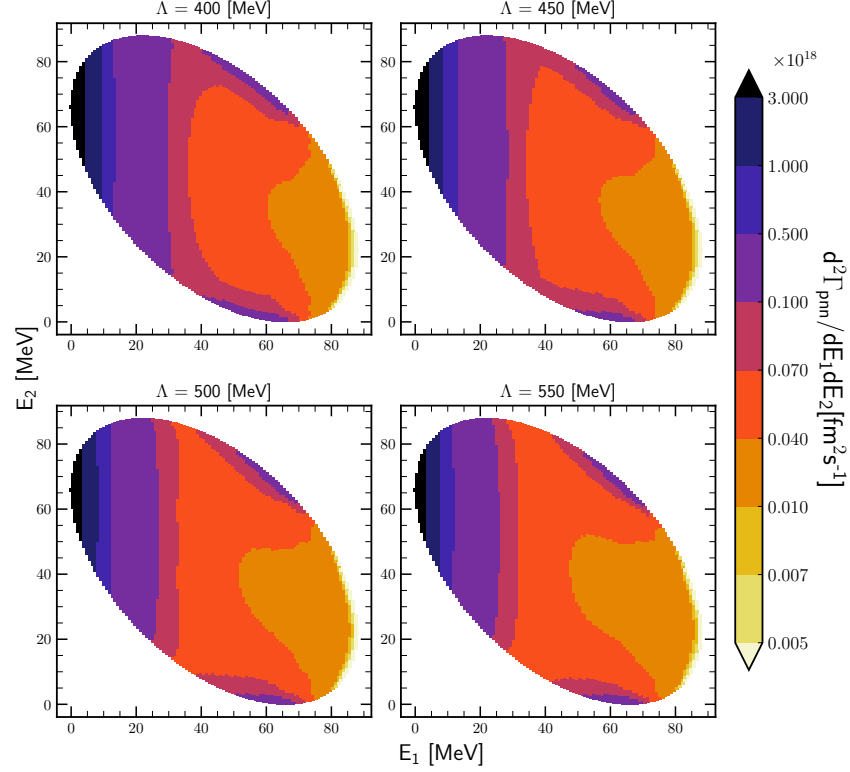


Figure 3.54: Intensity plots for the double differential absorption rates $d^2\Gamma_{pn}/dE_1 dE_2$ for the $\pi^- + {}^3\text{He} \rightarrow p + n + n$ process obtained using the SMS NN potential at N^4LO^+ supplemented by N^2LO 3NF with plane wave part only (without rescattering). All other contributions are the same as in Fig. 3.52: 1NC + 2NC and 2NF+3NF. Each panel presents predictions obtained with different values of the cut-off parameter Λ : from $\Lambda = 400$ MeV (upper left) to $\Lambda = 550$ MeV (lower right). Nucleon 1 is a proton.

(they are also shown up at the maximum point, which is around $E_n = 66.9$ MeV now): the difference between N^2LO and N^4LO^+ predictions at this point is 29.0%; the relative difference between all the predictions except for N^2LO is much smaller, but still is approx. 7.5%; the N^4LO^+ predictions are also very similar for $\Lambda = 500$ MeV and 550 MeV (the spread is 1.6%) while all remaining predictions are quite distinguished - the spread is 39.1%. I find that observable very interesting in the context of experimental studies as a measurement of neutron at $E \approx 70$ MeV is nowadays within our reach.

Moving to the next figures, Fig. 3.62 and Fig. 3.63, I show 1-dim dependence of the absorption rate on the Dalitz coordinates $r = \sqrt{x^2 + y^2}$ and $\phi = \arctan \frac{y}{x}$, respectively. A similar trend is preserved, namely chiral order figures show that N^2LO predictions outstand from all other predictions, and noticeable cut-off dependence is observed.

In general, we can conclude that predictions are converged starting from the N^3LO chiral order (for NN force) as most of the demonstrated results show that the difference between N^3LO , N^4LO and N^4LO^+ is negligible. At the same time, we observe a strong cut-off dependence with predictions obtained with $\Lambda = 500$ MeV and 550 MeV being very similar, but with a large spread of all the rest results. This nature of the cut-off dependence is also reflected in the total absorption rate, presented in Fig. 3.49.

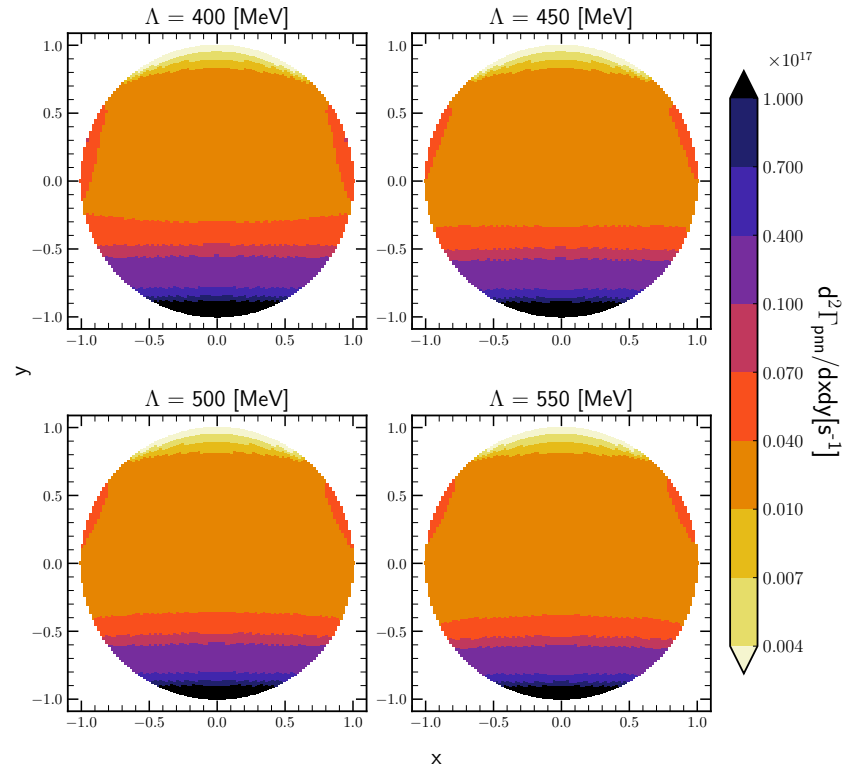


Figure 3.55: The same as in Fig. 3.54 but for the double differential absorption rates $d^2\Gamma_{pnn}/dx dy$.

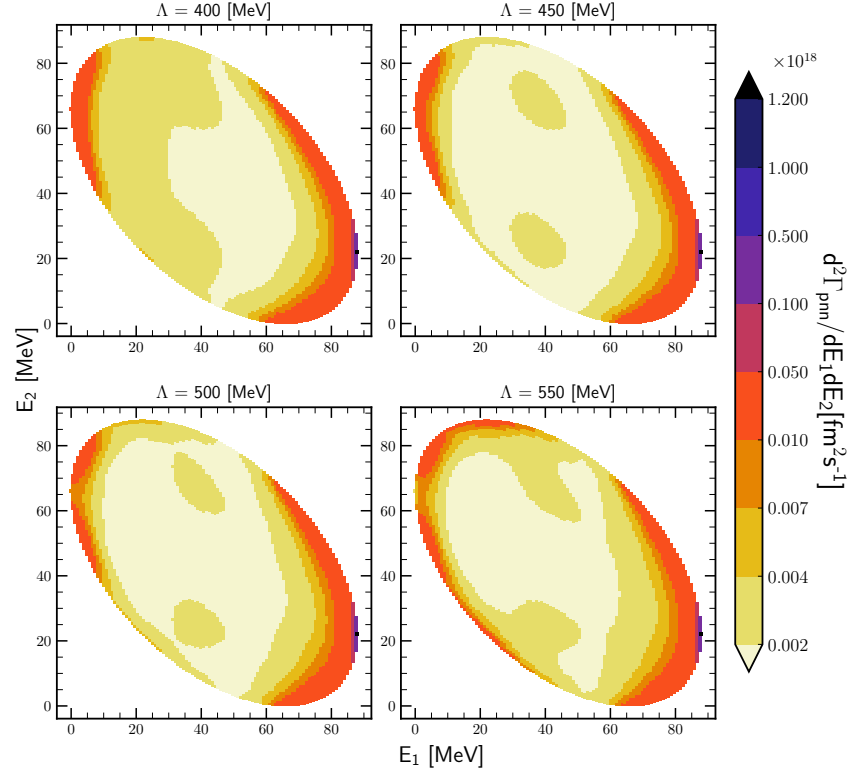


Figure 3.56: Intensity plots for the double differential absorption rates $d^2\Gamma_{pn}/dE_1 dE_2$ for the $\pi^- + {}^3\text{He} \rightarrow p + n + n$ process obtained using the SMS NN potential at N^4LO^+ supplemented by N^2LO 3NF with 1NC only (without 2N) currents. All other contributions are the same as in Fig. 3.52: PWIAS+RESC and 2NF+3NF. Each panel presents predictions obtained with different values of the cut-off parameter Λ : from $\Lambda = 400$ MeV (upper left) to $\Lambda = 550$ MeV (lower right). Nucleon 1 is a proton.

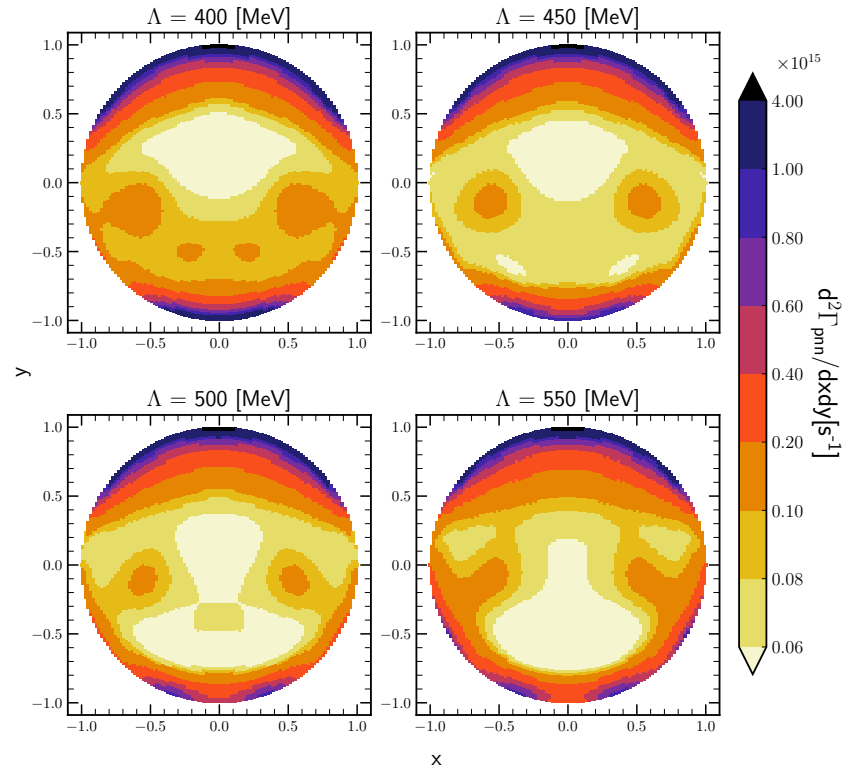


Figure 3.57: The same as in Fig. 3.56 but for the double differential absorption rates $d^2\Gamma_{pnn}/dx dy$.

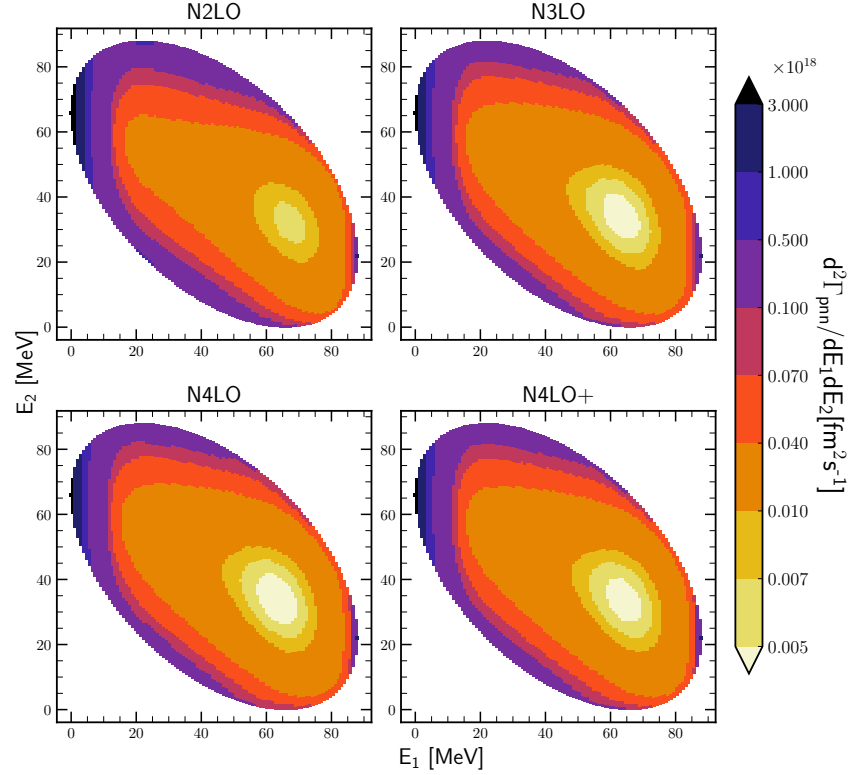


Figure 3.58: Intensity plots for the double differential absorption rates $d^2\Gamma_{pn}/dE_1 dE_2$ for the $\pi^- + {}^3\text{He} \rightarrow p + n + n$ process obtained using the SMS potential at N^4LO^+ with all contributions possible: plane wave + rescattering, 1NC+2NC, 2NF+3NF. Each panel presents predictions obtained with different chiral orders of the SMS NN potential: from N^2LO (upper left) to N^4LO^+ (lower right) and with $\Lambda = 450$ MeV. Nucleon 1 is a proton. 3NF was taken as N^2LO in each case.

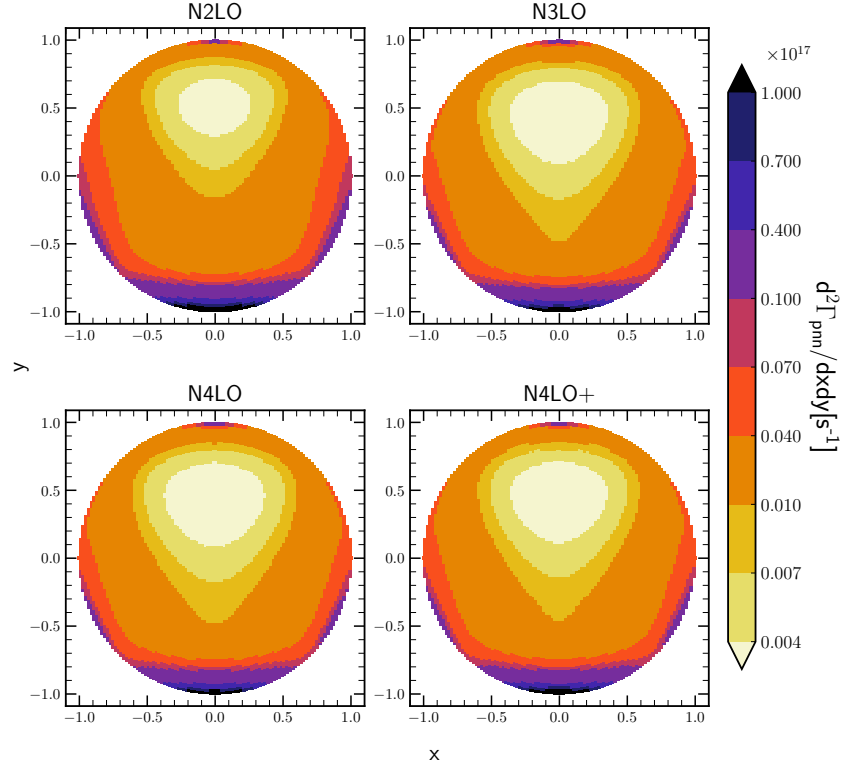


Figure 3.59: The same as in Fig. 3.58 but for the double differential absorption rates $d^2\Gamma_{pnn}/dxdy$.

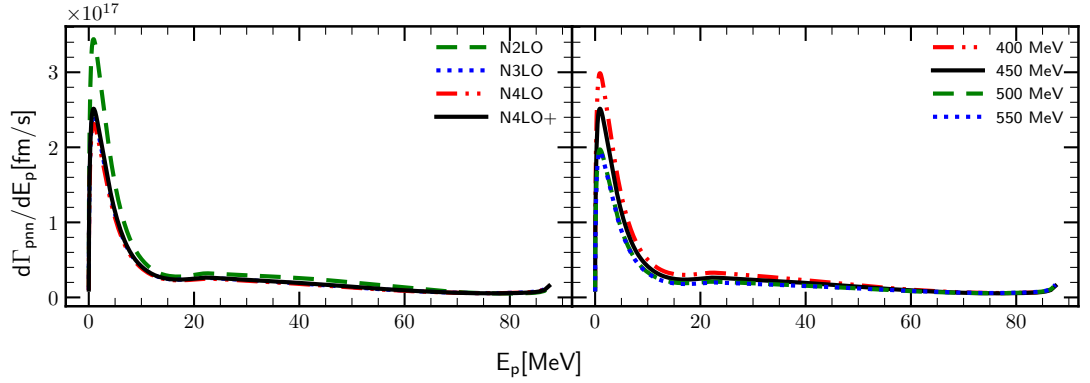


Figure 3.60: Differential absorption rate $d\Gamma_{pnn}/dE_p$ as a function of the proton energy E_p for the $\pi^- + {}^3\text{He} \rightarrow p + n + n$ process. Left panel shows results obtained with the NN $N^2\text{LO}$ (green dashed line), $N^3\text{LO}$ (blue dotted line), $N^4\text{LO}$ (red dashed-double-dotted line) and $N^4\text{LO}^+$ (black solid line) chiral orders plus $N^2\text{LO}$ 3NF, and with $\Lambda = 450$ MeV. The right panel includes results obtained with the $N^4\text{LO}^+$ SMS NN potential plus $N^2\text{LO}$ 3NF with different values of the Λ : 400 MeV (red dashed-double-dotted line), Λ : 450 MeV (black solid line), Λ : 500 MeV (green dashed line) and Λ : 550 MeV (blue dotted line). All predictions were obtained with "FULL-(1NC+2N)-(2NF+3NF)" setup.

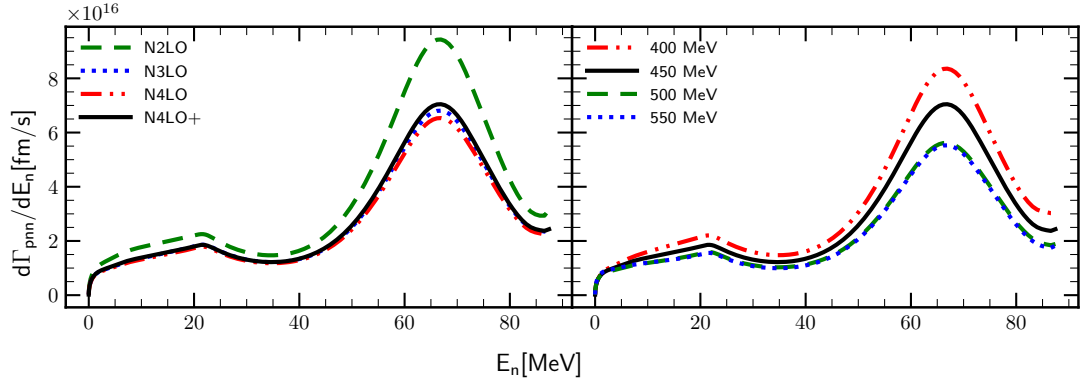


Figure 3.61: The same as in Fig. 3.60 but for the differential absorption rate $d\Gamma_{pnn}/dE_n$ as a function of the neutron energy E_n .

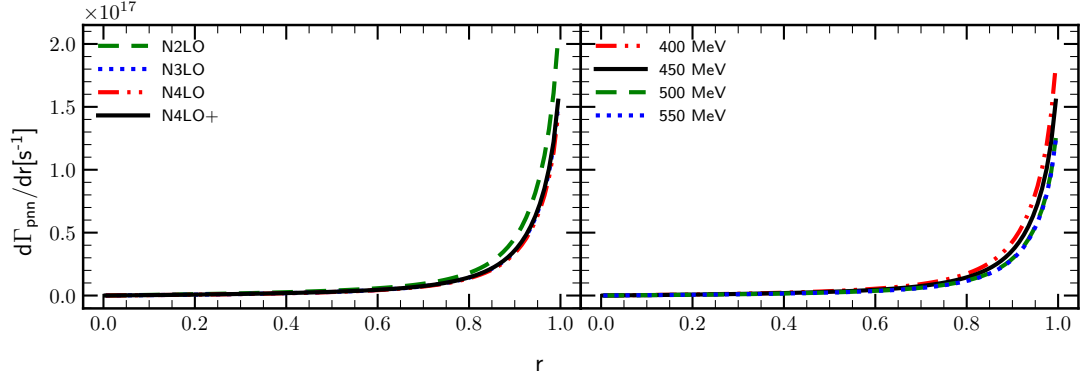


Figure 3.62: The same as in Fig. 3.60 but for the differential absorption rate $d\Gamma_{pnn}/dr$ as a function of the parameter r of the Dalitz coordinates: $r = \sqrt{x^2 + y^2}$.

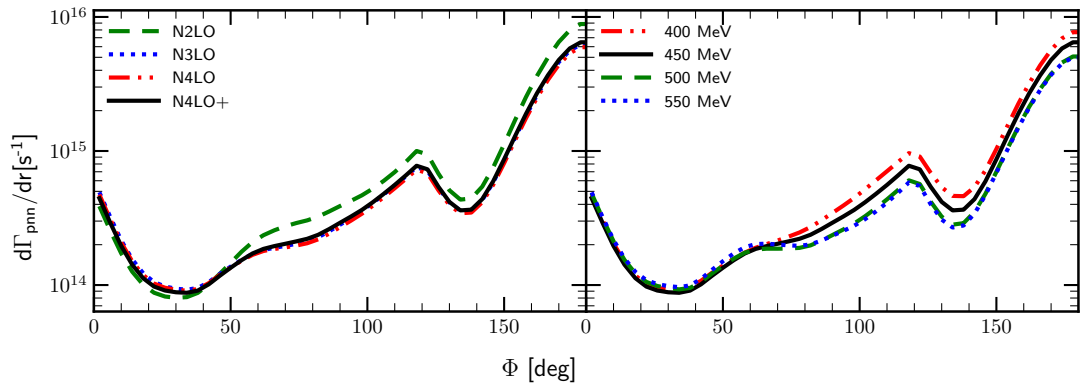


Figure 3.63: The same as in Fig. 3.62 but for the differential absorption rate $d\Gamma_{pnn}/d\phi$ as a function of the azimuthal angle ϕ of the Dalitz coordinates: $\phi = \arctan \frac{y}{x}$.

3.4.3 Pion absorption in ${}^3\text{H}$

In this subsection, I will show the results of calculations for the $\pi^- + {}^3\text{H} \rightarrow n + n + n$ process. In this case, only a three-body breakup is allowed as no two-body configuration can be composed out of three neutrons.

The total absorption rate Γ_{nnn} for that process is shown in Fig. 3.64 as a function of the chiral order of the SMS NN potential while each curve represents different cut-off values used to obtain the prediction. The most advanced dynamical model was used in this case, namely Plane wave plus rescattering part, both single- and two-nucleon currents and two-nucleon plus three-nucleon interaction.

Similarly to the three-body break-up of ${}^3\text{He}$, we see that with each subsequent chiral order predictions become closer to each other, so the cut-off dependence gets weaker. Also, the prediction with $\Lambda = 550$ MeV at N^3LO is strangely above the prediction with $\Lambda = 500$ MeV. We can also notice, that at N^4LO predictions with cut-off values 500 MeV and 550 MeV are much closer to each other than to results obtained with other Λ s.

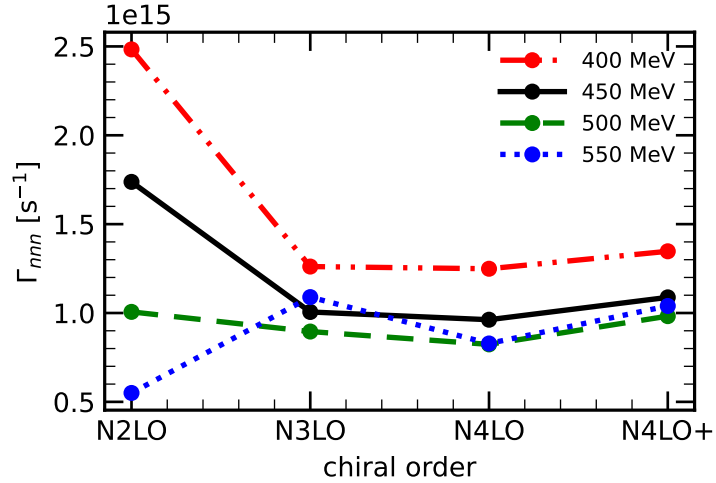


Figure 3.64: Absorption rate for $\pi^- + {}^3\text{H} \rightarrow n + n + n$ reaction as a function of the chiral order with different values of the cut-off parameter Λ . Predictions were obtained with 3NF at N^2LO .

In Figs. 3.65 and 3.66 I show intensity plots for the double differential absorption rates $d^2\Gamma_{nnn}/dE_1dE_2$ for the $\pi^- + {}^3\text{H} \rightarrow n + n + n$ process as functions of the nucleons energies (Fig. 3.65) and of the Dalitz coordinates (Fig. 3.66), respectively. Each panel in the figures presents predictions obtained with different values of the cut-off parameter Λ . On the contrary to the ${}^3\text{He}$ case, we see a symmetric distribution of the absorption rate with respect to the center of the figure. It is because of the symmetry of the three-body system as we have three identical particles - neutrons. The dominant contribution comes from QFS(nn) regions - where one of the neutrons is a spectator and has the lowest energy (close to 0) and the rest two are sharing almost all the energy equally. In Fig. 3.65 these regions are around $(E_1, E_2) = (0, 65), (65, 0)$ and $(65, 65)$ MeV. Same regions are presented in Fig. 3.66 at around $(x, y) = (0, -1), (-0.85, 0.5)$ and $(0.85, 0.5)$. We see that predictions are not sensitive to the cut-off value. The only difference that can be noticed is in the distribution of the region with the lowest values of the Γ_{nnn} (the center of each figure). It is mostly probably caused by the fact that the very small values introduce larger calculational uncertainties.

Figs. 3.67 and 3.68 show similar intensity plots but each panel includes predictions obtained with different chiral orders of the SMS NN potential. Each of the panels shows very similar distributions of the absorption rate, except for the N²LO one, where the central region (with lowest Γ_{nnn} values) is less pronounced.

It is further confirmed by the Fig. 3.69 (left panel) where differential absorption rate $d\Gamma_{nnn}/dE_n$ at N²LO has much larger peaks (at around $E_n = 0$ MeV and $E_n = 68$ MeV) while all the rest predictions are relatively close to each other. On the right panel of Fig. 3.69 we see that only the prediction obtained with $\Lambda = 400$ MeV is different from the rest. It is interesting to notice, as such a difference could not be observed from the colormaps.

Very similar tendency is observed in Figs. 3.70 and 3.71. In these figures I show differential absorption rate with respect to the Dalitz radial coordinates r and ϕ , respectively. The same as in Fig. 3.69 we see that N²LO and $\Lambda = 400$ MeV predictions are different from the rest, while all the other predictions are very close to each other.

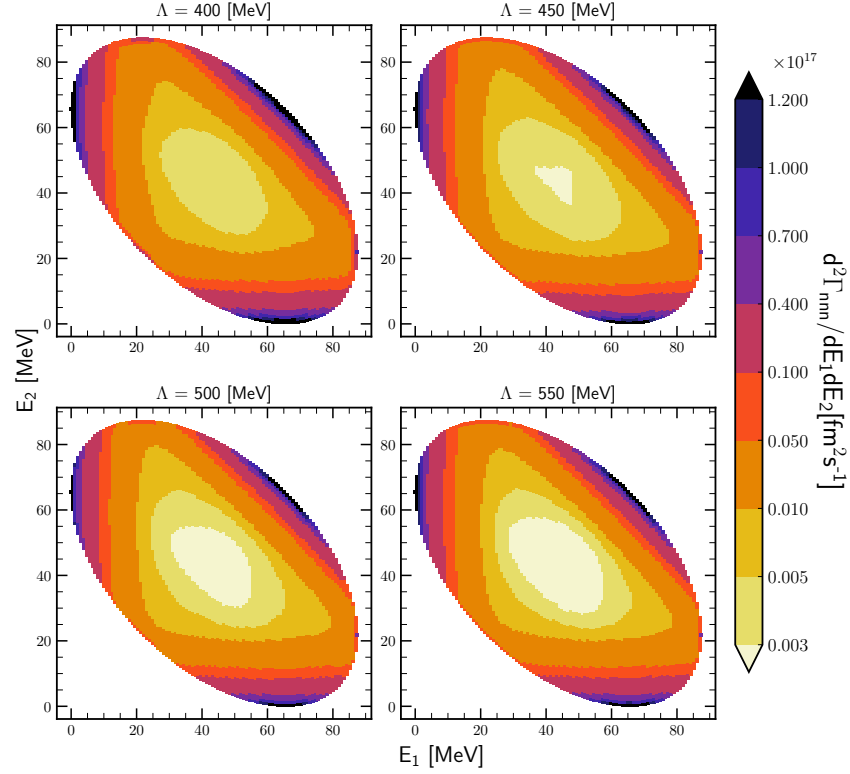


Figure 3.65: Intensity plots for the double differential absorption rates $d^2\Gamma_{nnn}/dE_1dE_2$ for the $\pi^- + {}^3\text{H} \rightarrow n + n + n$ process obtained using the SMS NN potential at N⁴LO⁺ supplemented by N²LO 3NF with all ingredients possible: plane wave + rescattering, 1NC+2NC, 2NF+3NF. Each panel presents predictions obtained with different values of the cut-off parameter Λ : from 400 MeV (upper left) to 550 MeV (lower right).

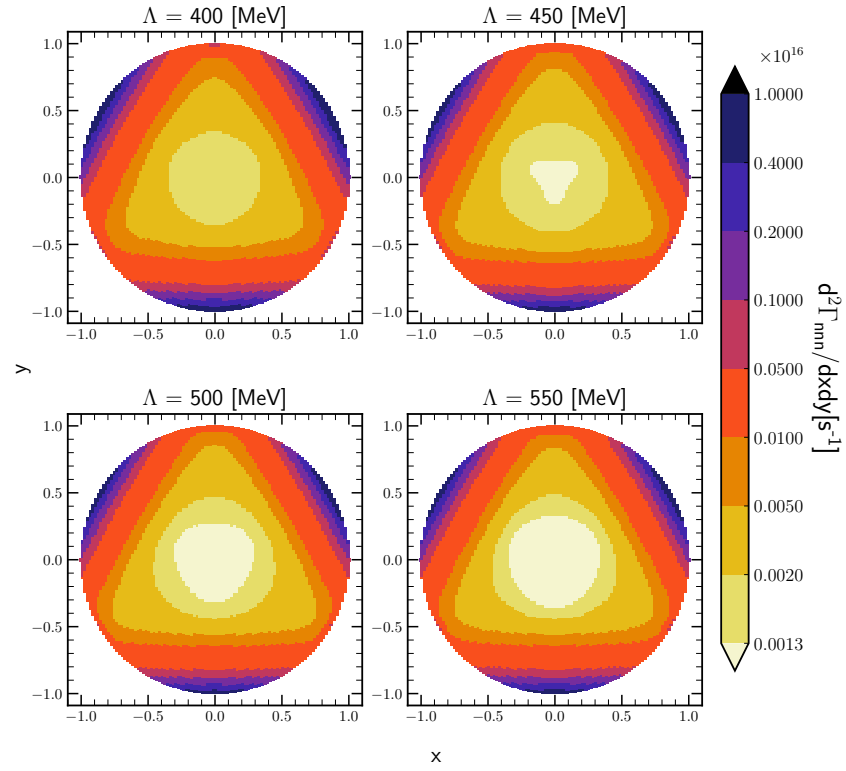


Figure 3.66: The same as in Fig. 3.65 but for the double differential absorption rates $d^2\Gamma_{nnn}/dx dy$.

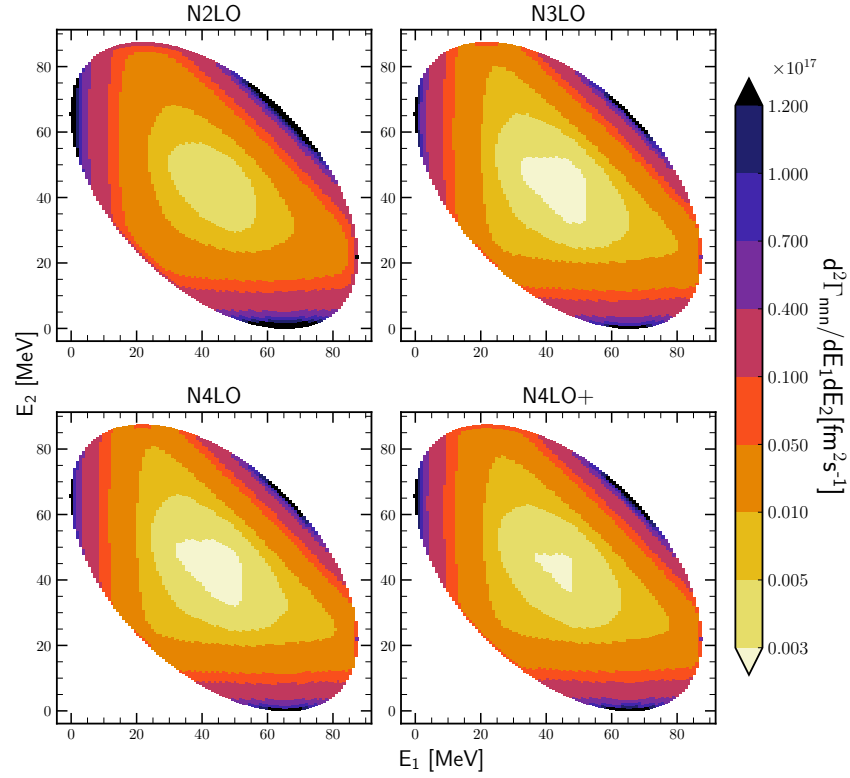


Figure 3.67: Intensity plots for the double differential absorption rates $d^2\Gamma_{nn}/dE_1 dE_2$ for the $\pi^- + {}^3\text{H} \rightarrow n + n + n$ process obtained using the SMS potential at N^4LO^+ with all contributions possible: plane wave + rescattering, 1NC+2NC, 2NF+3NF. Each panel presents predictions obtained with different chiral orders of the SMS potential: from N^2LO (upper left) to N^4LO^+ (lower right) and with $\Lambda = 450$ MeV.

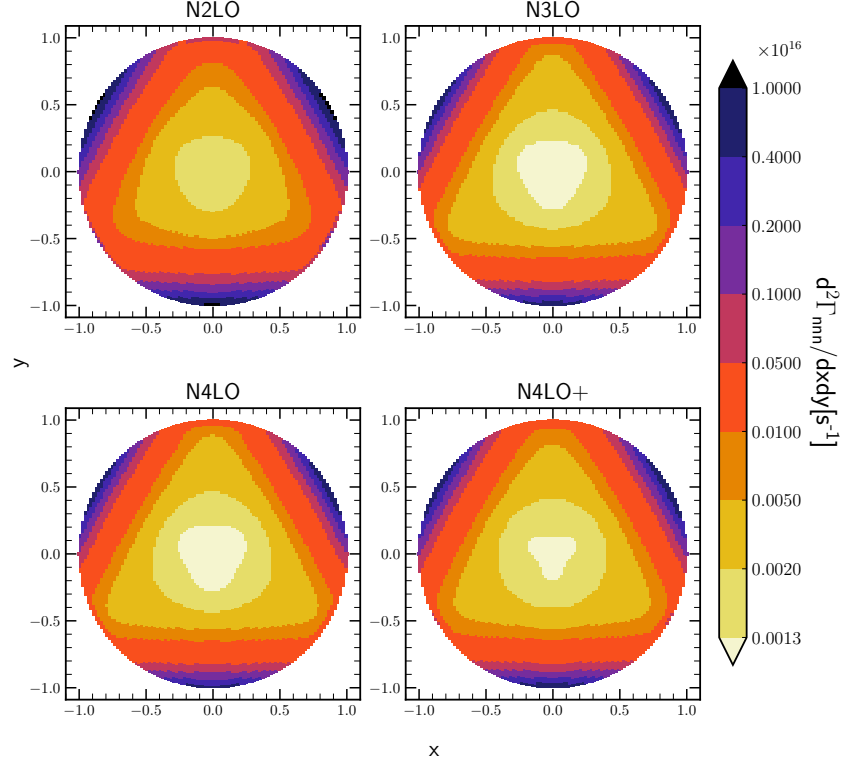


Figure 3.68: The same as in Fig. 3.67 but for the double differential absorption rates $d^2\Gamma_{nnn}/dxdy$.

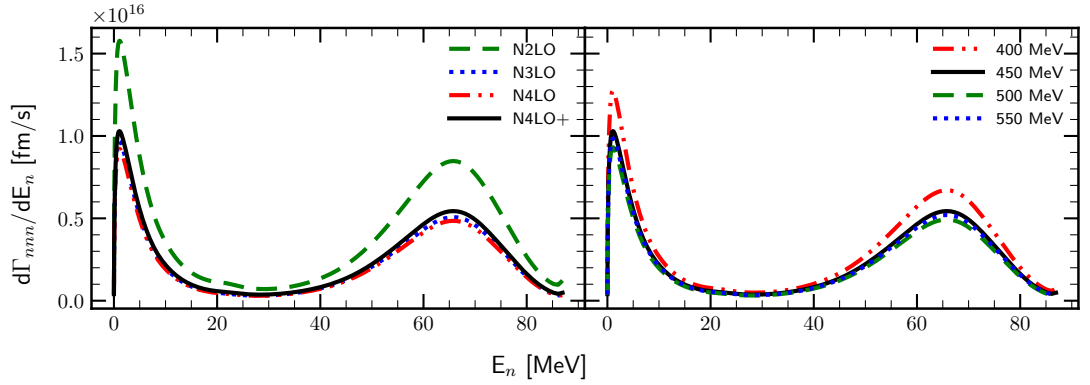


Figure 3.69: Differential absorption rate $d\Gamma_{nnn}/dE_n$ as a function of the neutron energy E_n for the $\pi^- + 3H \rightarrow n + n + n$ process. Left panel shows results obtained with NN force at glsn2lo (green dashed line), $N^3\text{LO}$ (blue dotted line), $N^4\text{LO}$ (red dashed-double-dotted line) and $N^4\text{LO}^+$ (black solid line) chiral orders, and with $\Lambda = 450$ MeV. The $N^2\text{LO}$ 3NF was used. The right panel includes results obtained with the $N^4\text{LO}^+$ NN SMS potential supplemented by the $N^2\text{LO}$ 3NF with different values of the Λ : 400 MeV (red dashed-double-dotted line), Λ : 450 MeV (black solid line), Λ : 500 MeV (green dashed line line) and Λ : 550 MeV (blue dotted line). All predictions were obtained with "FULL-(1NC+2N)-(2NF+3NF)" setup.

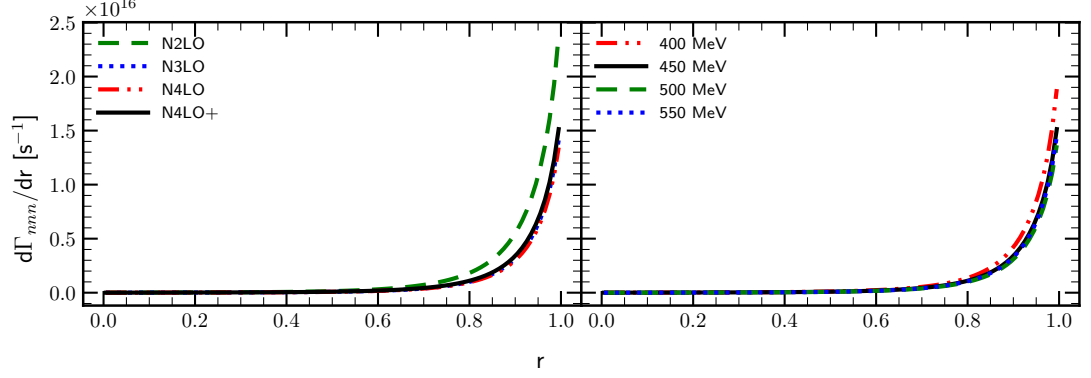


Figure 3.70: The same as in Fig. 3.69 but for the differential absorption rate $d\Gamma_{nnn}/dr$ as a function of the parameter r of the Dalitz coordinates: $r = \sqrt{x^2 + y^2}$.

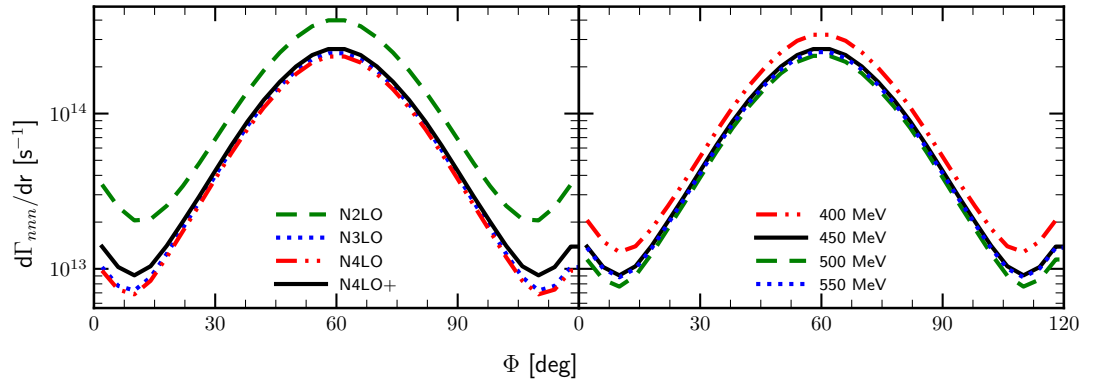


Figure 3.71: The same as in Fig. 3.70 but for the differential absorption rate $d\Gamma_{nnn}/d\phi$ as a function of the azimuthal angle ϕ of the Dalitz coordinates: $\phi = \arctan \frac{y}{x}$.

CHAPTER 4

SUMMARY

In this thesis, I investigated ${}^2\text{H}$, ${}^3\text{H}$ and ${}^3\text{He}$ photodisintegration processes as well as pion absorption by the same nuclei. To analyze these reactions and to calculate predictions for observables I used a chiral model of interaction namely the most advanced SMS nucleon-nucleon chiral potential up to N^4LO^+ order augmented by the consistently regularized three-nucleon force at N^2LO . Results prepared with the semi-phenomenological AV18 potential have been shown as a reference point. The current operator is restricted to the single-nucleon part only. Both processes are studied in the momentum space. The standard Lippmann-Schwinger equation is solved to get the t -operator and consequently 2N scattering state. For the three-nucleon processes, the formalism of Faddeev equations has been applied. I solved corresponding equations for Faddeev components both for the bound and 3N scattering states. In that way, I include all initial state as well as final state interactions. I am also able to test the importance of FSI by restricting components to only plane wave approximation. The used formalism allows me to study not only the total cross section or capture rates but also various differential cross sections and polarization observables. The latter ones are very important to test the model and to compare with experimental data. That also allows me to conclude on the sensitivity of various observables on studied effects and to pick up observables which after measurement could deliver the most valuable information.

The main goal of this work was to investigate the quality of currently available predictions based on the semi-phenomenological SMS interactions if applied to the studied here processes. Such information is necessary due to expected two- and more- nucleon currents at higher orders of chiral expansion, consistent with the SMS potential. Various features of the model can be studied in that context. Firstly, I investigated if the predictions based on the SMS interaction are converged with respect to the chiral order. It would then be a hint whether the development of higher-order contributions to the potential is required. In most of the results, I observe very converged predictions since there is a small difference between the last two investigated chiral orders: N^4LO and N^4LO^+ . This difference in most of the regarded cases does not exceed a few percent. Another piece of evidence is the width of the truncation band for N^4LO^+ predictions. For the deuteron photodisintegration process, observables have a maximum truncation error below 1 % for the two studied photon energies: $E_\gamma = 30 \text{ MeV}$ and $E_\gamma = 100 \text{ MeV}$. The same trend is presented also for other regarded reactions as well. This leads us towards a conclusion that further chiral orders would not improve the predictions much and the current model

shows satisfactory convergence. This is also confirmed by the AV18 predictions which are always very close to $N^4\text{LO}^+$ (see e.g. Fig. 3.8, Fig. 3.26 etc.).

The other interesting point in the investigation of chiral potential is its dependence on the value of its intrinsic cut-off parameter Λ , the four values of which (400, 450, 500 and 550 MeV) were investigated. I have shown that the relative spread of predictions concerning the cutoff value is higher for the higher energies. For example, the spread of the differential cross section for ^3He photodisintegration at $E_\gamma = 30$ MeV at the characteristic point (maximum) is around 3 %, while at $E_\gamma = 100$ MeV it is three times larger - around 3 % (see Fig. 3.28, Fig. 3.29 and discussions). Nevertheless, usually for higher energies the difference between the predictions obtained with different values of Λ is smaller than the difference with experimental data (when it is available) which is visible in Fig. 3.5(b).

I have also studied the role of the various dynamical components of the model by checking how they influence the predicted values. Namely, I compare predictions obtained with plane wave part only (first term in the Eq. (2.31)), with those taking into account the final state interaction, as well as predictions with and without 2N current contributions (introduced via the Siegert approach). For example, in the Fig. 3.4b we see predictions for the deuteron photodisintegration cross section obtained without rescattering part, without 2N contributions and full predictions. The contribution of rescattering processes is relatively small for the predictions at $E_\gamma = 30$ MeV, but is increasing with larger energies. The analysis of the relative difference at the specific θ_p value does not show this trend (the differences are 10 %, 7 % and 4 % for $E_\gamma = 30, 100$ and 140 MeV respectively at $\theta_p = 80^\circ$), but we see that at the lower energy predicted cross section values are qualitatively very similar and they differ mainly around the maximum point. In contrast, for the larger energies, predictions differ qualitatively, and the analyzed point depicts the region where the difference is relatively small. The difference between the full predictions and the ones, where only 1NC was used is much bigger: even for the lowest energy inclusion of two-body currents changes the cross section by around 50 % and for the larger two it grows up to $\sim 78\%$. Clearly, both rescattering part and 2NC contributions are very important and bring significant contributions. Similar trend is visible also for other observables (see e.g. Fig. 3.10) and processes (see Figs. 3.52, 3.54, 3.56 to compare contributions for the pion absorption on ^3He).

That complex pattern reveals the interplay between interaction and the current operator, and is one more recommendation after derivation fully consistent model, i.e. with consistent 2N forces, 3N forces, and one-, two- and three-body currents. Such a model must be applied only within the readable scheme to compute observables. My work culminated in the preparation of such a scheme, both analytical and numerical sides, and now we are ready to study more sophisticated Hamiltonians.

Giving mentioned above results, we can also conclude that the current version of the chiral SMS potential is of very high quality: it rather does not require any additional development in the sense of adding higher chiral orders or regularization. Contrary, the 2NC should be completely derived as it is expected to bring a significant contribution and thus improvements in our understanding of electromagnetic processes.

Among the studied processes and observables, I would like to point out the following main conclusions:

1. *The most sensitive to FSI are for (observables, energies)*
2. 2NC is very important for the regarded processes and observables. Even including it via the Siegert theorem allows seeing significant improvements (e.g. Figs. 3.2,

- 3.6 and 3.8 for the deuteron photodisintegration process). For the pion absorption process, I took into account full 2NC and the difference between Fig. 3.52 and Fig. 3.56 (1NC only) is a proof of its importance.
3. The importance of 3NF is less obvious looking at my results. For example, for ${}^3\text{He}$ photodisintegration in Fig. 3.30 3NF makes cutoff dependence weaker, but the difference between predictions with and without 3NF is not very big.
 4. Investigation of the differential cross section is beneficial compared to the total cross sections as it allows us to see smaller details of the model in a sense of convergence and cutoff dependence. One may observe the reason for particular discrepancies (e.g. some singularity point which causes computational problems). It is also less computationally expensive as the total cross section is obtained via integration of the differential cross section through the whole region.
 5. It would be interesting to check experimentally if theoretical uncertainties appearing at some configurations would be also reflected in the data. For example, we see that the kinematical configuration presented in Fig. 3.28 is less sensitive to the model parameters than the one in Fig. 3.30. So measuring the data for ${}^3\text{He}$ gives more possibilities to test the model as lots of configurations for the differential cross section are possible.
 6. For $\pi+{}^3\text{H}$ there are 3 neutrons in the final state. It is one of very few such situations and it allows us to investigate the neutron-neutron nucleon force. Moreover, it even allows us to investigate the neutron-neutron-neutron force. Such a situation is hardly reproducible in experiments as neutrons are hard to detect, but we can still analyze theoretical predictions and make conclusions. It is very important for the construction of the complete model of nucleon-nucleon 2N and 3N interactions.
 7. In my opinion, for the pion absorption it would be interesting to have a measurement data for FSI(nn) region. As we do not have a fully consistent 2NC, it would be beneficial to take into account experimental data when analyzing predictions obtained by approximations or (in future) by fully consistent 2NC. Comparing results from Fig. 3.52 and Fig. 3.54 we see a huge difference in the region around $E_1 = 85 \text{ MeV}$, $E_2 = 21 \text{ MeV}$, where the FSI(nn) is.
 8. Our Full model nicely describes data up to $E_\gamma = \sim 70 \text{ MeV}$. It is not a strict value, but the general trend is that for higher energies the difference between the model and the data is growing. For example, predictions for the total cross section and the tensor analyzing powers for the deuteron photodisintegration nicely describe experimental data even up to $E_\gamma = 100 \text{ MeV}$ (Fig. 3.2, Fig. 3.19), but photon asymmetry starts deteriorating even after $E_\gamma = 40 \text{ MeV}$ (Fig. 3.25).

BIBLIOGRAPHY

- [1] P. Reinert, H. Krebs, and E. Epelbaum. Semilocal momentum-space regularized chiral two-nucleon potentials up to fifth order. *Eur. Phys. J.*, A54(5):86, 2018.
- [2] D. M. Skopik, Y. M. Shin, M. C. Phenneger, and J. J. Murphy. Photodisintegration of deuterium determined from the electrodisintegration process. *Phys. Rev. C*, 9:531–536, Feb 1974.
- [3] F. F. Liu, D. E. Lundquist, and B. H. Wiik. Measurements of the polarization of protons from deuteron photodisintegration. *Phys. Rev.*, 165:1478–1482, Jan 1968.
- [4] Reinhold Kose, Bjoern Martin, Rainer Runkel, Helmut Wahlen, and Karl Heinz Kissler. Measurements of the polarization of protons from deuteron photodisintegration for photon energies between 282 and 405 MeV. *Zeitschrift für Physik A Hadrons and nuclei*, 220:305–320, 1969.
- [5] T. Kamae, I. Arai, T. Fujii, H. Ikeda, N. Kajiura, S. Kawabata, K. Nakamura, K. Ogawa, H. Takeda, and Y. Watase. Observation of an anomalous structure in proton polarization from deuteron photodisintegration. *Phys. Rev. Lett.*, 38:468–471, Feb 1977.
- [6] Andrew L. Cooper, K. J. Kelly, E. Machado, I. Pogrebnyak, J. Surbrook, C. Tysor, P. Thompson, M. Emamian, B. Walsh, B. Carlin, J. R. Dermigny, A. E. Champagne, and T. B. Clegg. Development of a variable-energy, high-intensity, pulsed-mode ion source for low-energy nuclear astrophysics studies. *Review of Scientific Instruments*, 89(8):083301, 2018.
- [7] A.P. Tonchev, M. Boswell, C.R. Howell, H.J. Karwowski, J.H. Kelley, W. Tornow, and Y.K. Wu. The high intensity γ -ray source (hi γ s) and recent results. *Nuclear Instruments and Methods in Physics Research Section B: Beam Interactions with Materials and Atoms*, 241(1):170–175, 2005. The Application of Accelerators in Research and Industry.
- [8] J Bermuth, P Merle, C Carasco, D Baumann, R Böhm, D Bosnar, M Ding, M.O Distler, J Friedrich, J.M Friedrich, J Golak, W Glöckle, M Hauger, W Heil, P Jennewein, J Jourdan, H Kamada, A Klein, M Kohl, B Krusche, K.W Krygier, H Merkel, U Müller, R Neuhausen, A Nogga, Ch Normand, E Otten, Th Pospischil, M Potokar,

- D Rohe, H Schmieden, J Schmiedeskamp, M Seimetz, I Sick, S Širca, R Skibiński, G Testa, Th Walcher, G Warren, M Weis, H Witała, H Wöhrle, and M Zeier. The neutron charge form factor and target analyzing powers from $^3\text{He}(e\rightarrow,e'n)$ scattering. *Physics Letters B*, 564(3):199–204, 2003.
- [9] B.L. Ioffe. QCD (quantum chromodynamics) at low energies. *Progress in Particle and Nuclear Physics*, 56(1):232–277, 2006.
- [10] S.R. Beane, W. Detmold, K. Orginos, and M.J. Savage. Nuclear physics from lattice qcd. *Progress in Particle and Nuclear Physics*, 66(1):1–40, 2011.
- [11] R. Machleidt and D. R. Entem. Chiral effective field theory and nuclear forces. *Phys. Rept.*, 503:1–75, 2011.
- [12] W. Glöckle. Effects of the two-pion exchange three-nucleon force in the triton and ^3He . *Nuclear Physics A*, 381(3):343–364, 1982.
- [13] A. Nogga, H. Kamada, W. Glöckle, and B. R. Barrett. The α particle based on modern nuclear forces. *Phys. Rev. C*, 65:054003, May 2002.
- [14] S.A. Coon, M.D. Scadron, P.C. McNamee, B.R. Barrett, D.W.E. Blatt, and B.H.J. McKellar. The two-pion-exchange three-nucleon potential and nuclear matter. *Nuclear Physics A*, 317(1):242–278, 1979.
- [15] B. S. Pudliner, V. R. Pandharipande, J. Carlson, Steven C. Pieper, and R. B. Wiringa. Quantum monte carlo calculations of nuclei with $A < \sim 197$. *Phys. Rev. C*, 56:1720–1750, Oct 1997.
- [16] V. G. J. Stoks, R. A. M. Klomp, C. P. F. Terheggen, and J. J. de Swart. Construction of high-quality nn potential models. *Phys. Rev. C*, 49:2950–2962, Jun 1994.
- [17] Robert B. Wiringa, V. G. J. Stoks, and R. Schiavilla. An Accurate nucleon-nucleon potential with charge independence breaking. *Phys. Rev.*, C51:38–51, 1995.
- [18] A. Nogga, H. Kamada, and W. Glöckle. Modern nuclear force predictions for the α particle. *Phys. Rev. Lett.*, 85:944–947, Jul 2000.
- [19] J. Carlson and R. Schiavilla. Structure and Dynamics of Few Nucleon Systems. *Rev. Mod. Phys.*, 70:743–842, 1998.
- [20] H Arenhövel and M. Sanzone. Photodisintegration of the deuteron: A Review of theory and experiment. *Few Body Syst. Suppl.*, 3:1–183, 1991.
- [21] V. G. J. Stoks, R. A. M. Klomp, M. C. M. Rentmeester, and J. J. de Swart. Partial-wave analysis of all nucleon-nucleon scattering data below 350 MeV. *Phys. Rev. C*, 48:792–815, Aug 1993.
- [22] C. Van Der Leun and C. Alderliesten. The deuteron binding energy. *Nuclear Physics A*, 380(2):261–269, 1982.
- [23] S. Weinberg. Nuclear forces from chiral lagrangians. *Physics Letters B*, 251(2):288–292, 1990.

- [24] S. Weinberg. Effective chiral lagrangians for nucleon-pion interactions and nuclear forces. *Nuclear Physics B*, 363(1):3–18, 1991.
- [25] Evgeny Epelbaum, Hans-Werner Hammer, and Ulf-G. Meißner. Modern Theory of Nuclear Forces. *Rev. Mod. Phys.*, 81:1773–1825, 2009.
- [26] E. Epelbaum, W. Glöckle, and U.-G. Meißner. Improving the convergence of the chiral expansion for nuclear forces - i: Peripheral phases. *The European Physical Journal A*, 19(1):125–137, January 2004.
- [27] E. Epelbaum. Few-nucleon forces and systems in chiral effective field theory. *Progress in Particle and Nuclear Physics*, 57(2):654–741, 2006.
- [28] D. R. Entem, R. Machleidt, and Y. Nosyk. High-quality two-nucleon potentials up to fifth order of the chiral expansion. *Phys. Rev. C*, 96:024004, Aug 2017.
- [29] E. Epelbaum, W. Glöckle, and Ulf-G. Meißner. Nuclear forces from chiral lagrangians using the method of unitary transformation (i): Formalism. *Nuclear Physics A*, 637(1):107–134, 1998.
- [30] E Epelbaum, W Glöckle, and UG Meißner. The two-nucleon system: Nuclear forces from chiral lagrangians using the method of unitary transformation ii. *Nucl. Phys. A*, 671:295–331, 2000.
- [31] E. Epelbaum, A. Nogga, W. Glöckle, H. Kamada, Ulf-G. Meißner, and H. Witała. Three-nucleon forces from chiral effective field theory. *Phys. Rev. C*, 66:064001, Dec 2002.
- [32] Evgeny Epelbaum, Walter Glöckle, and Ulf-G Meißner. The two-nucleon system at next-to-next-to-next-to-leading order. *Nuclear Physics A*, 747(2-4):362–424, 2005.
- [33] R. Skibiński, J. Gola, K. Topolnicki, H. Witała, E. Epelbaum, W. Glöckle, H. Krebs, A. Nogga, and H. Kamada. Triton with long-range chiral N³LO three-nucleon forces. *Phys. Rev. C*, 84:054005, Nov 2011.
- [34] H Witała, J Gola, R Skibiński, and K Topolnicki. Calculations of three-nucleon reactions with N³LO chiral forces: achievements and challenges. *Journal of Physics G: Nuclear and Particle Physics*, 41(9):094011, jul 2014.
- [35] E. Epelbaum, H. Krebs, and U. G. Meißner. Precision nucleon-nucleon potential at fifth order in the chiral expansion. *Phys. Rev. Lett.*, 115(12):122301, 2015.
- [36] D. R. Entem and R. Machleidt. Accurate charge-dependent nucleon-nucleon potential at fourth order of chiral perturbation theory. *Phys. Rev. C*, 68:041001, Oct 2003.
- [37] R Machleidt and D R Entem. Towards a consistent approach to nuclear structure: EFT of two- and many-body forces. *Journal of Physics G: Nuclear and Particle Physics*, 31(8):S1235–S1244, July 2005.
- [38] R. Machleidt, P. Liu, D. R. Entem, and E. Ruiz Arriola. Renormalization of the leading-order chiral nucleon-nucleon interaction and bulk properties of nuclear matter. *Phys. Rev. C*, 81:024001, Feb 2010.

- [39] M. Piarulli, L. Girlanda, L. E. Marcucci, S. Pastore, R. Schiavilla, and M. Viviani. Electromagnetic structure of $A = 2$ and 3 nuclei in chiral effective field theory. *Phys. Rev.*, C87(1):014006, 2013.
- [40] M. Piarulli, L. Girlanda, R. Schiavilla, R. Navarro Pérez, J. E. Amaro, and E. Ruiz Arriola. Minimally nonlocal nucleon-nucleon potentials with chiral two-pion exchange including Δ resonances. *Phys. Rev. C*, 91:024003, Feb 2015.
- [41] A. Ekström, G. R. Jansen, K. A. Wendt, G. Hagen, T. Papenbrock, B. D. Carlsson, C. Forssén, M. Hjorth-Jensen, P. Navrátil, and W. Nazarewicz. Accurate nuclear radii and binding energies from a chiral interaction. *Phys. Rev. C*, 91:051301, May 2015.
- [42] I. Tews, Z. Davoudi, A. Ekström, J. D. Holt, and J. E. Lynn. New ideas in constraining nuclear forces. *Journal of Physics G: Nuclear and Particle Physics*, 47(10):103001, aug 2020.
- [43] H.-W. Hammer, Sebastian König, and U. van Kolck. Nuclear effective field theory: Status and perspectives. *Rev. Mod. Phys.*, 92:025004, Jun 2020.
- [44] T. A. Lähde and Ulf-G. Meißner. *Nuclear Lattice Effective Field Theory*. Springer International Publishing, 2019.
- [45] A. J. F. Siegert. Note on the interaction between nuclei and electromagnetic radiation. *Phys. Rev.*, 52:787–789, Oct 1937.
- [46] J. Golak, H. Kamada, H. Witała, Walter Glöckle, J. Kuroś, R. Skibiński, V. V. Kotlyar, K. Sagara, and H. Akiyoshi. Faddeev calculations of proton deuteron radiative capture with exchange currents. *Phys. Rev.*, C62:054005, 2000.
- [47] C.G.J. Jacobi. Ueber Gauss neue Methode, die Werthe der Integrale näherungsweise zu finden. 1826.
- [48] W Glöckle. *The quantum mechanical few-body problem*. Texts and monographs in physics. Springer, Berlin, 1983.
- [49] W. Glöckle, H. Witała, D. Hüber, H. Kamada, and J. Golak. The three-nucleon continuum: achievements, challenges and applications. *Physics Reports*, 274(3):107–285, 1996.
- [50] R. Skibiński, J. Golak, H. Kamada, H. Witała, W. Glöckle, and A. Nogga. Search for three-nucleon force effects in two-body photodisintegration of ${}^3\text{He}({}^3\text{H})$ and in the time reversed proton-deuteron radiative capture process. *Phys. Rev. C*, 67:054001, May 2003.
- [51] R. Skibiński, J. Golak, H. Witała, W. Glöckle, and A. Nogga. Different formulations of ${}^3\text{He}$ and ${}^3\text{H}$ photodisintegration. *The European Physical Journal A*, 24(1):31–38, February 2005.
- [52] J. Arrington, C. D. Roberts, and J. M. Zanotti. Nucleon electromagnetic form factors. *Journal of Physics G: Nuclear and Particle Physics*, 34(7):S23, May 2007.

- [53] J. Jourdan. Measurements of neutron electromagnetic form factors. *Nuclear Physics A*, 654(1, Supplement 1):513c–516c, 1999.
- [54] J. Golak, R. Skibiński, H. Witała, W. Glöckle, A. Nogga, and H. Kamada. Electron and photon scattering on three-nucleon bound states. *Phys. Rept.*, 415:89–205, 2005.
- [55] M. Gari and W. Krümpelmann. The electromagnetic form factor of the neutron. *Physics Letters B*, 173(1):10–14, 1986.
- [56] V. Bernard, N. Kaiser, and Ulf-G. Meißner. Chiral dynamics in nucleons and nuclei. *International Journal of Modern Physics E*, 04(02):193–344, 1995.
- [57] V. Lensky, V. Baru, J. Haidenbauer, C. Hanhart, A. E. Kudryavtsev, and U. G. Meißner. Towards a field theoretic understanding of $NN \rightarrow NN\pi$. *The European Physical Journal A*, 27(1):37–45, Jan 2006.
- [58] J. Golak, R. Skibiński, K. Topolnicki, H. Witała, A. Grassi, H. Kamada, and L. E. Marcucci. Momentum space treatment of inclusive neutrino scattering off the deuteron and trinucleons. *Phys. Rev.*, C98(1):015501, 2018.
- [59] L. E. Marcucci, M. Piarulli, M. Viviani, L. Girlanda, A. Kievsky, S. Rosati, and R. Schiavilla. Muon capture on deuteron and ^3He . *Phys. Rev. C*, 83:014002, Jan 2011.
- [60] D. Gotta, M. Dörr, W. Fetscher, G. Schmidt, H. Ullrich, G. Backenstoss, M. Izycki, W. Kowald, I. Schwanner, P. Weber, and H. J. Weyer. Negative pion absorption at rest in ^3He . *Physical Review C*, 51(2):469–492, February 1995.
- [61] E. Epelbaum, H. Krebs, and Ulf-G. Meißner. Improved chiral nucleon-nucleon potential up to next-to-next-to-next-to-leading order. *Eur. Phys. J. A*, 51(5), May 2015.
- [62] S. Binder, A. Calci, E. Epelbaum, R. J. Furnstahl, J. Golak, K. Hebeler, H. Kamada, H. Krebs, J. Langhammer, S. Liebig, P. Maris, Ulf-G. Meißner, D. Minossi, A. Nogga, H. Potter, R. Roth, R. Skibiński, K. Topolnicki, J. P. Vary, and H. Witała and. Few-nucleon systems with state-of-the-art chiral nucleon-nucleon forces. *Phys. Rev.*, C93(4):044002, 2016.
- [63] E. Epelbaum. High-precision nuclear forces : Where do we stand? *PoS*, CD2018:006, 2020.
- [64] S. B. S. Miller, A. Ekström, and C. Forssén. Posterior predictive distributions of neutron-deuteron cross sections, 2022.
- [65] J. A. Melendez, S. Wesolowski, and R. J. Furnstahl. Bayesian truncation errors in chiral effective field theory: Nucleon-nucleon observables. *Phys. Rev. C*, 96:024003, Aug 2017.
- [66] R. Skibiński, J. Golak, K. Topolnicki, H. Witała, Yu. Volkotrub, H. Kamada, A. M. Shirokov, R. Okamoto, K. Suzuki, and J. P. Vary. Nucleon-deuteron scattering with the jisp16 potential. *Phys. Rev. C*, 97:014002, Jan 2018.

- [67] Yu. Volkotrub, J. Golak, R. Skibiński, K. Topolnicki, H. Witała, E. Epelbaum, H. Krebs, and P. Reinert. Uncertainty of three-nucleon continuum observables arising from uncertainties of two-nucleon potential parameters. *Journal of Physics G: Nuclear and Particle Physics*, 47(10):104001, aug 2020.
- [68] M. Bosman, A. Bol, J.F. Gilot, P. Leleux, P. Lipnik, and P. Macq. Measurement of the total cross section for the $^1\text{H}(n, \gamma) ^2\text{H}$ reaction between 37 and 72 MeV. *Physics Letters B*, 82(2):212–215, 1979.
- [69] J. Arends, H.J. Gassen, A. Hegerath, B. Mecking, G. Nöldeke, P. Prenzel, T. Reichelt, A. Voswinkel, and W.W. Sapp. Experimental investigation of deuteron photodisintegration in the δ -resonance region. *Nuclear Physics A*, 412(3):509–522, 1984.
- [70] R. Moreh, T. J. Kennett, and W. V. Prestwich. $^2\text{H}(\gamma, n)$ absolute cross section at 2754 kev. *Phys. Rev. C*, 39:1247–1250, Apr 1989.
- [71] Y. Birenbaum, S. Kahane, and R. Moreh. Absolute cross section for the photodisintegration of deuterium. *Phys. Rev. C*, 32:1825–1829, Dec 1985.
- [72] R. Bernabei, A. Incicchitti, M. Mattioli, P. Picozza, D. Prosperi, L. Casano, S. d’Angelo, M. P. De Pascale, C. Schaerf, G. Giordano, G. Matone, S. Frullani, and B. Girolami. Total cross section for deuteron photodisintegration between 15 and 75 mev. *Phys. Rev. Lett.*, 57:1542–1545, Sep 1986.
- [73] I. A. Rachek, L. M. Barkov, S. L. Belostotsky, V. F. Dmitriev, M. V. Dyug, R. Gilman, R. J. Holt, B. A. Lazarenko, S. I. Mishnev, V. V. Nelyubin, D. M. Nikolenko, A. V. Osipov, D. H. Potterveld, R. Sh. Sadykov, Yu. V. Shestakov, V. N. Stibunov, D. K. Toporkov, H. de Vries, and S. A. Zevakov. Measurement of tensor analyzing powers in deuteron photodisintegration. *Phys. Rev. Lett.*, 98:182303, May 2007.
- [74] S. Q. Ying, E. M. Henley, and G. A. Miller. Deuteron photodisintegration. *Phys. Rev.*, C38:1584–1600, 1988. and references therein.
- [75] E. de Sanctis et al. Deuteron Photodisintegration Cross-section Between 100-MeV and 220-MeV. *Phys. Rev. Lett.*, 54:1639, 1985.
- [76] S.I. Mishnev, D.M. Nikolenko, S.G. Popov, I.A. Rachek, A.B. Temnykh, D.K. Toporkov, E.P. Tsentalovich, B.B. Wojtsekhowski, S.L. Belostotsky, V.V. Nelyubin, V.V. Sulimov, and V.N. Stibunov. Measurement of the analyzing power components in photodisintegration of the polarized deuteron. *Physics Letters B*, 302(1):23–28, 1993.
- [77] K. M. Schmitt and H. Arenhövel. Deuteron photodisintegration with the bonn OBE potentials. *Few-body syst.*, 7(3):95–117, 1989.
- [78] A. Grassi, J. Golak, W. N. Polyzou, R. Skibiński, H. Witała, and H. Kamada. Electron and neutrino scattering off the deuteron in a relativistic framework. *Phys. Rev. C*, 107:024617, Feb 2023.
- [79] K.-H. Krause, J. Sobolewski, J. Ahrens, J.M. Henneberg, and B. Ziegler. Photodisintegration of the deuteron by linearly polarized photons. *Nuclear Physics A*, 549(3):387–406, 1992.

- [80] M. P. De Pascale, G. Giordano, G. Matone, D. Babusci, R. Bernabei, O. M. Bilaniuk, L. Casano, S. d'Angelo, M. Mattioli, P. Picozza, D. Prosperi, C. Schaerf, S. Frullani, and B. Girolami. Polarization asymmetry in the photodisintegration of the deuteron. *Phys. Rev. C*, 32:1830–1841, Dec 1985.
- [81] V.P. Barannik, V.G. Gorbenko, V.A. Gushchin, Y.V. Zhebrovskii, L.Y. Kolesnikov, Y.V. Kulish, A.L. Rubashkin, and P.V. Sorokin. Study of the cross-section asymmetry in photodisintegration of the deuteron by polarized. gamma. rays at low energies. *Sov. J. Nucl. Phys. (Engl. Transl.); (United States)*, 38:5, 11 1983.
- [82] I.E. Vnukov, I.V. Glavanakov, Y.F. Krechetov, A.P. Potylitsyn, G.A. Saruev, V.N. Stibunov, and A.N. Tabachenko. Photodisintegration of the deuteron by linearly polarized photons below the pion-production threshold. *Sov. J. Nucl. Phys. (Engl. Transl.); (United States)*, 47:4, 4 1988.
- [83] W. Del Bianco, L. Federici, G. Giordano, G. Matone, G. Pasquariello, P. Picozza, R. Caloi, L. Casano, M. P. De Pascale, L. Ingrosso, M. Mattioli, E. Poldi, C. Schaerf, P. Pelfer, D. Prosperi, S. Frullani, B. Girolami, and H. Jeremie. Neutron Asymmetry Measurements in the Deuteron Photodisintegration between 10 and 70 MeV. *Phys. Rev. Lett.*, 47:1118–1120, Oct 1981.
- [84] R. W. Jewell, W. John, J. E. Sherwood, and D. H. White. Polarization of Photoneutrons Produced from Deuterium by 2.75-MeV Gamma Rays. *Phys. Rev.*, 139:B71–B79, Jul 1965.
- [85] J.M. Cameron, C.A. Davis, H. Fielding, P. Kitching, J. Pasos, J. Soukup, J. Uegaki, J. Wesick, H.S. Wilson, R. Abegg, D.A. Hutcheon, C.A. Miller, A.W. Stetz, and I.J. van Heerden. Radiative capture of polarized neutrons by hydrogen below the pion production threshold. *Nuclear Physics A*, 458(4):637–651, 1986.
- [86] Th. Strauch, F. D. Amaro, D. F. Anagnostopoulos, P. Bühler, D. S. Covita, H. Gorke, D. Gotta, A. Gruber, A. Hirtl, P. Indelicato, E.-O. Le Bigot, M. Nikipelov, J. M. F. dos Santos, S. Schlessler, Ph. Schmid, L. M. Simons, M. Trassinelli, J. F. C. A. Veloso, and J. Zmeskal. Precision determination of the $d\pi \leftrightarrow NN$ transition strength at threshold. *Phys. Rev. Lett.*, 104:142503, Apr 2010.
- [87] Th. Strauch, F. D. Amaro, D. F. Anagnostopoulos, P. Bühler, D. S. Covita, H. Gorke, D. Gotta, A. Gruber, A. Hirtl, P. Indelicato, E. O. Le Bigot, M. Nikipelov, J. M. F. dos Santos, Ph. Schmid, S. Schlessler, L. M. Simons, M. Trassinelli, J. F. C. A. Veloso, and J. Zmeskal. Pionic deuterium. *The European Physical Journal A*, 47(7), July 2011.
- [88] J. Golak, V. Urbaneych, R. Skibiński, H. Witała, K. Topolnicki, V. Baru, A. A. Filin, E. Epelbaum, H. Kamada, and A. Nogga. Pion absorption from the lowest atomic orbital in ^2H , ^3H , and ^3He . *Phys. Rev. C*, 106:064003, Dec 2022.
- [89] I. Schwanner, G. Backenstoss, W. Kowald, L. Tauscher, H.-J. Weyer, D. Gotta, and H. Ullrich. Pionic and muonic x-ray measurements on light isotopes. *Nuclear Physics A*, 412(2):253–272, 1984.
- [90] J. McCarthy, T. Meyer, R. C. Minehart, E. A. Wadlinger, K. O. H. Ziock, and J. Vincent. Negative pion capture in ^3He . *Phys. Rev. C*, 11:266–268, Jan 1975.

BIBLIOGRAPHY

- [91] P. Truöl, H.W. Baer, J.A. Bistirlich, K.M. Crowe, N. de Botton, and J.A. Helland. Measurement of the panofsky ratio in ^3He . *Phys. Rev. Lett.*, 32:1268–1271, Jun 1974.